Journal of Materials Chemistry B

ROYAL SOCIETY OF CHEMISTRY

REVIEW

View Article Online
View Journal | View Issue

Cite this: J. Mater. Chem. B, 2025, 13, 4279

MXenes and MXene-based composites for biomedical applications

Taposhree Dutta,[a] Parvej Alam*[b] and Satyendra Kumar Mishra *[c]

MXenes, a novel class of two-dimensional materials, have recently emerged as promising candidates for biomedical applications due to their specific structural features and exceptional physicochemical and biological properties. These materials, characterized by unique structural features and superior conductivity, have applications in tissue engineering, cancer detection and therapy, sensing, imaging, drug delivery, wound treatment, antimicrobial therapy, and medical implantation. Additionally, MXene-based composites, incorporating polymers, metals, carbon nanomaterials, and metal oxides, offer enhanced electroactive and mechanical properties, making them highly suitable for engineering electroactive organs such as the heart, skeletal muscle, and nerves. However, several challenges, including biocompatibility, functional stability, and scalable synthesis methods, remain critical for advancing their clinical use. This review comprehensively overviews MXenes and MXene-based composites, their synthesis, properties, and broad biomedical applications. Furthermore, it highlights the latest progress, ongoing challenges, and future perspectives, aiming to inspire innovative approaches to harnessing these versatile materials for next-generation medical solutions.

Received 22nd December 2024,
Accepted 24th February 2025

DOI: 10.1039/d4tb02834a

rsc.li/materials-b

1. Introduction

Researchers have long been fascinated by biological structures with intriguing functions, which have motivated the development of various innovative nanomaterials. Beyond their enhanced features, recent materials science and engineering advances have created bioinspired nanostructures with multifunctional capabilities. Researchers have designed structures with distinct physicochemical properties by leveraging biomimetics and bioinspired materials derived from nature.[1]

Two-dimensional (2D) materials have become a prominent area of interest in materials science, particularly following the discovery of graphene and its remarkable characteristics.[2–5] MXenes, transition metal carbides, nitrides, and carbonitrides represent a new class of 2D materials that have recently garnered significant attention.[6,7]

Due to their intriguing properties—such as exceptional electrical conductivity, elastic mechanical strength, hydrophilicity, and chemical stability—MXenes and MXene-based composites have been extensively researched for a wide range of applications, including tissue engineering, regenerative medicine, biological imaging and sensing, gene and drug delivery, water desalination and treatment, and cancer therapeutics.[8–12]

MXenes are produced by etching the 'A' layer element from MAX phase ceramics. They combine hydrophilicity and adaptable surface chemistry with surprisingly high conductivity, surpassing other solution-processed 2D materials.[13] Despite extensive research on biomedical applications, conventional organic compounds with acceptable biocompatibility and biodegradability have seen limited development for clinical use due to their poor thermal and chemical stability and limited functionality.[14,15] However, 2D structures developed through top-down techniques (such as ion exchange, ultrasonic exfoliation, and micromechanical exfoliation) and bottom-up techniques (including ion exchange, hydro/solvothermal synthesis, microwave-assisted synthesis, chemical vapor deposition, and topochemical transformation) have demonstrated promising characteristics for biomedical applications.[16–18] For instance, in preclinical settings, selenium-coated tellurium nano heterojunctions, which offer nontoxicity benefits, have shown promising results in eliminating lung and hepatocellular carcinoma. According to this study, the photothermal treatment (PTT)-based strategy can alter the tumor microenvironment and significantly accelerate the death of malignant cells.[19] Scientists are also interested in developing novel micro- and nanostructures with distinctive properties, particularly those

[a] Department of Chemistry, Indian Institute of Engineering Science and Technology Shibpur, Howrah, W.B. – 711103, India
[b] Space and Reslinent Research Unit, Centre Tecnològic de Telecomunicacions de Catalunya Castelldefels, Spain. E-mail: smishra@cttc.es
[c] Clinical Translational Research Center of Aggregation-Induced Emission, School of Medicine, The Second Affiliated Hospital, School of Science and Engineering, Shenzhen Institute of Aggregate Science and Technology, The Chinese University of Hong Kong, Shenzhen (CUHK-Shenzhen), Guangdong 518172, P. R. China. E-mail: alamparvej@cuhk.edu.cn

influenced by nature. Various nature-inspired structures with high activity have been investigated, including bioinspired polymeric woods, lotus-leaf-like super-hydrophobic surfaces, and nacre-like structures.[20,21]

Bioinspired and biomimetic nanostructures have been designed for various applications, including medicine and gene delivery, biological systems for healing, textile industries, and waterproofing.[22–25] These structures have demonstrated significant economic and environmental benefits compared to other materials. They have proven more biocompatible and biodegradable in drug delivery and have better-targeting qualities than conventional materials.[26] Their enhanced targeting abilities in cancer therapy have resulted in fewer adverse effects. Combining biological and synthetic systems can create novel drug delivery or gene carrier systems. Johnson *et al.* highlighted the significant advantages of these delivery systems, including improved biocompatibility, minimal toxicity, and reduced immunogenicity.[27] Additionally, bioinspired sensor systems exhibit appealing characteristics such as ultra-sensitivity, low power consumption, and self-adaptability.[8,28] A novel approach for enhancing the mechanical properties, photothermal conductivity, flexibility, adsorption performance, and electrical conductivity of bioinspired MXene-based structures has emerged through creative design.[29–33] However, further concentrated research is needed to develop simple, low-cost, and scalable methods for creating bioinspired MXene-based structures with superior characteristics and high performance.[34–37] Moreover, key attributes of bioinspired MXene-based structures—such as stability, biosafety, and multifunctionality—can be effectively regulated and enhanced through appropriate functionalization processes.[19,38] Specially designed MXenes for biological applications are poised to take center stage in research platforms dedicated to biomedicine and nanomedicine. They can create the intelligent nano-systems of the future with significant applications in biological and clinical domains.[39,40] In this discussion, we explore the recent developments in MXenes and MXene-based composites, their biological applications, and an outlook on future advancements. This review aims to provide a comprehensive and methodical exploration of the latest advancements in MXenes and MXene-based composite materials for biomedical applications. We delve into the synthesis of MXene-based composites, including polymer, metal, metal oxide, and nanocarbon materials, and analyze their exceptional electric, mechanical, thermal, optical, and magnetic properties. Furthermore, we offer an in-depth overview of their biomedical applications, including tissue engineering, cancer diagnosis and therapy, advanced sensors (biosensors, pressure sensors, humidity sensors, human motion sensors, gas sensors), imaging modalities such as luminous imaging, computed tomography (CT), magnetic resonance imaging (MRI), and photoacoustic imaging (PAI), drug delivery, wound treatment, antimicrobial therapy, medical implants and sound energy harvesting and cochlear implant (Fig. 1). By addressing the current challenges and unlocking the potential of MXene-based materials, this review seeks to inspire innovative approaches and accelerate progress in transforming these materials into groundbreaking solutions for modern medicine.

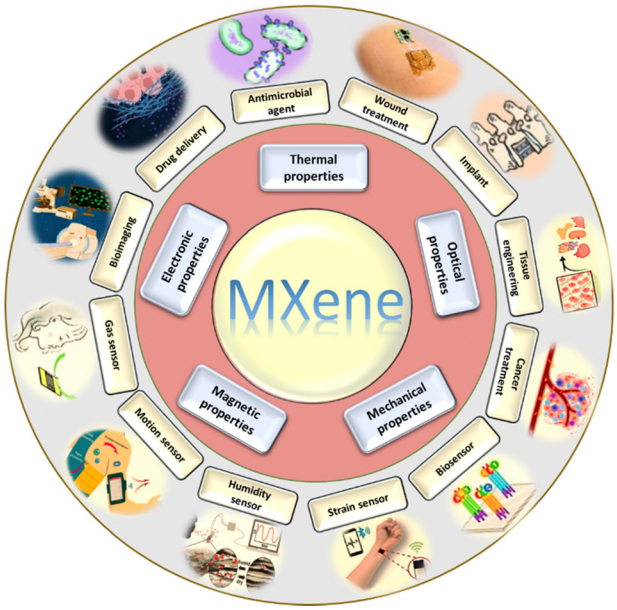

Fig. 1 MXene-based materials and their biological applications.

2. Synthesis

2.1. Synthesis of MXenes

MXenes are synthesized by chemically selectively etching specific atomic layers from the layered carbide, nitride, and carbonitride precursor. Generally, aqueous HF is used as an etchant to selectively etch A layers from the corresponding MAX phases at room temperature (Fig. 2). By removing the weakly bonded Al layers from the Ti_3AlC_2 phase, $Ti_3C_2T_x$ (where T = OH and F) was produced in a notable experiment.[41] The related reactions are as follows:

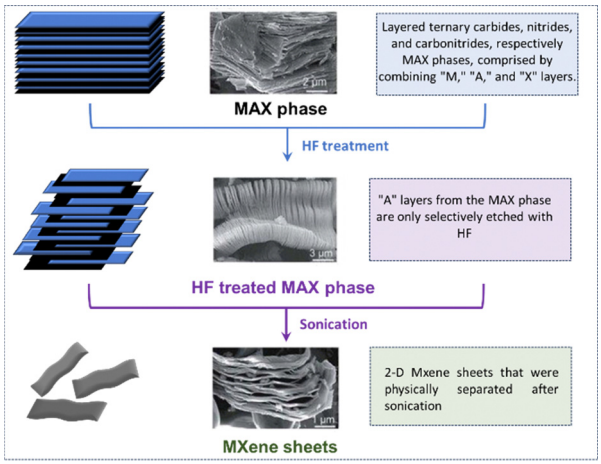

Fig. 2 Schematic diagram of the development of MXene nanosheets *via* exfoliation/degradation of the MAX phase[47] (Copyright (2024) Royal Society of Chemistry).

$$Ti_3AlC_2(s) + 3HF(aq) \rightarrow Ti_3C_2(s) + AlF_3(s) + 3/2H_2(g) \quad (1)$$

$$Ti_3C_2(s) + 2H_2O \rightarrow Ti_3C_2(OH)_2(s) + H_2(g) \quad (2)$$

$$Ti_3C_2(s) + 2HF(l) \rightarrow Ti_3C_2F_2(s) + H_2(g) \quad (3)$$

–F and –OH terminations are the products of reactions (2) and (3). After the particles were separated by centrifugation, they were washed with deionized water. MXenes typically have stacked structures without delamination. Initially, sonication was used to produce single- or few-layer MXenes, but this was eventually replaced by the more effective intercalation of dimethyl sulfoxide (DMSO).[42] With this technique, additional MXene sheets from MAX phases containing Al were synthesized. Whereas the MAxene phase has a layered hexagonal structure, consisting of alternating stacks of M-layers and A-group elements, with X-atoms occupying the octahedral voids of the M-layers. M stands for early transition metals (such as Ti, Zr, V, Nb, and Mo), A for IIIA or IV A elements (such as Al, Si, Ga, and Ge), and X for C or N. While the chemical bond between M and A possesses only metallic bonding capabilities, the bond between M and X shows significant covalent, metallic, and ionic properties.[43] Through this bond-energy phenomenon, powerful acids or molten salts can selectively remove the A layer from the MAX phase without breaking the M–X bonds.[44,45] Following the selective etching of the A layer, surface functional groups (T_x) such as OH, O, F, and Cl replace the A element to form MXene ($M_{n+1}X_nT_x$). The presence of the surface functional groups enhances the electrical conductivity and activity of the material, creating a wide scope of possibilities for additional surface modification (Fig. 2).[6,46]

Additionally, depending on the temperature and particle size, different etching conditions (such as time and HF concentration) are required to convert a specific MAX phase. For instance, the time needed for etching and HF concentration can be successfully reduced by grinding the MAX phase to a smaller particle size.[48–50] The first MXene, $Ti_3C_2T_x$, was created by Naguib *et al.* by soaking Ti_3AlC_2 particles in 50% concentrated hydrofluoric acid (HF) at room temperature (RT) for two hours.[51,52] The X-ray diffraction (XRD) pattern before and after etching Ti_3AlC_2 is shown in Fig. 3(a). It is evident that after HF treatment, $Ti_3C_2T_x$ replaces Ti_3AlC_2, as indicated by the shift of the principal peak in the XRD pattern from around 40 to 10. The similarity between the experimental XRD pattern following HF etching and the simulated XRD patterns of $Ti_3C_2F_2$ and $Ti_3C_2(OH)_2$ (Fig. 3(a)) suggests the presence of functional groups.

Subsequently, other MAX phases were effectively treated using the HF etching technique, leading to the production of numerous new MXenes, such as Ti_2CT_x, V_2CT_x, Nb_2CT_x, Ti_2NT_x, $Ti_3C_2T_x$, Ti_3CNT_x, $Nb_4C_3T_x$, $Ta_4C_3T_x$, $V_4C_3T_x$, $Mo_2TiC_2T_x$, $Mo_2Ti_2C_3T_x$, $Cr_2TiC_2T_x$, and others.[48,55–60] Developing alternative, safer etchants is necessary because HF harms the environment and human health. To produce $Ti_3C_2T_x$, the less hazardous combination of hydrochloric acid (HCl) and lithium fluoride (LiF) was used, in which Ti_3AlC_2 particles were soaked for 24 hours at 35 °C.[53] The synthetic sample exhibited fewer

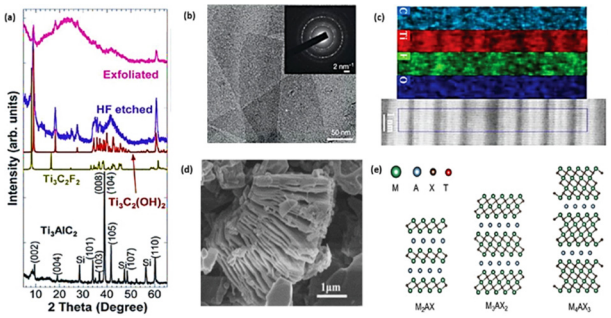

Fig. 3 (a) XRD spectra of Ti_3AlC_2 before and after HF etching[41] (Copyright (2011) John Wiley and Sons). (b) TEM image of $Ti_3C_2T_x$[53] (Copyright (2014) Nature). (c) STEM image with EDX spectra of $Ti_3C_2T_x$[10] (Copyright (2020) Royal Society of Chemistry). (d) After HF reaction, SEM image of $Zr_3Al_3C_5$[54] (Copyright (2016) John Wiley and Sons). (e) Crystal configurations of M_2AX, M_3AX_2, and M_4AX_3 phases[10] (Copyright (2020) Royal Society of Chemistry).

flaws, as shown by the transmission electron microscopy (TEM) image of $Ti_3C_2T_x$ in Fig. 3(b). However, the HCl and LiF mixture uses the exact etching mechanism as the HF solution because it contains hydrogen and fluoride ions. MXenes have also been developed using other combinations of acids (such as H_2SO_4) and salts containing fluorine ions (such as NaF, FeF_3, KF, CsF, and CaF_2).[53] Nevertheless, these combination solutions still emit some hazardous HF fumes during etching.

Additionally, ammonium hydrogen fluoride (NH_4HF_2) does not release hazardous gases, can synthesize MXenes, and is a mildly acidic, eco-friendly fluoride.[61] The reactions were as follows:

$$Ti_3AlC_2(s) + 3NH_4HF_2 \rightarrow (NH_4)_3AlF_6(s) + Ti_3C_2(s) + 3/2H_2(g) \quad (4)$$

$$Ti_3C_2(s) + aNH_4HF_2 + bH_2O \rightarrow (NH_3)_c(NH_4)_dTi_3C_2(OH)_xF_y \quad (5)$$

The atomic layers of $Ti_3C_2T_x$ are more regularly spaced and appear to be more tightly bonded due to slower and less violent reaction processes, along with the intercalation of both NH_3 and NH_4^+. The energy dispersive X-ray spectroscopy (EDX) maps and scanning transmission electron microscopy (STEM) images of synthesized $Ti_3C_2T_x$ are shown in Fig. 3(c). The EDX spectra confirm the presence of terminal hydroxyl and fluoride groups on the surface of $Ti_3C_2T_x$, displaying the distribution of C, Ti, F, and O atoms over the STEM image.

Additionally, the first nitride-based MXene, $Ti_4N_3T_x$, was successfully synthesized by heating a combination of Ti_4AlN_3 powder and molten fluoride salts at 550 °C in an argon environment.[62] The synthesis of $Ti_4N_3T_x$ serves as an excellent model for producing other 2D transition metal nitrides. Beyond MAX phases, a new family of layered ternary and quaternary compounds with the formula $MnAl_3C_2$ or $Mn[Al(Si)]_4C_3$ can also be used as precursors for synthesizing MXenes. $MnAl_3C_2$ or $Mn[Al(Si)]_4C_3$ can be structurally represented as two-dimensional $Mn^+{}_1C_n$ layers "glued" together with $(AlC)_x$ or $[Al(Si)C]_x$.[63] These novel compounds have enabled the successful production of $Zr_3C_2T_x$ and $Hf_3C_2T_x$. For instance, $Zr_3Al_3C_5$

was converted to $Zr_3C_2T_x$ by extracting the $(AlC)_x$ units with a 50% concentrated HF solution.[54] The chemical reaction is as follows:

$$Zr_3Al_3C_5(s) + HF \rightarrow AlF_3 + CH_4(g) + Zr_3C_2 \quad (6)$$

After treating $Zr_3Al_3C_5$ with HF, the XRD patterns (Fig. 3a) show that the position of the highest peak shifts from (103) to (111), and the intensities of the peaks originating from $Zr_3Al_3C_5$ significantly decrease. Additionally, the exfoliation of individual Al–C layers along the basal plane is evident in the scanning electron microscopy (SEM) image (Fig. 3(d)) of $Zr_3Al_3C_5$ following HF treatment, confirming the formation of $Zr_3C_2T_x$. In contrast, $Hf_3C_2T_x$ cannot be produced by HF etching away the $(AlC)_x$ units from $Hf_3Al_3C_5$ due to the powerful interfacial bonds between the Hf–C and Al–C units in $Hf_3Al_3C_5$.

A single-layer MXene typically requires additional processing, as synthesized MXenes are usually multi-layered.[64] There are currently two methods to reduce multi-layered MXenes to single layers: mechanical delamination and delamination by intercalation.[65] Intercalation is the primary method for producing single-layer MXene flakes, as multi-layered MXenes can accommodate different ions and molecules between their layers.[66] Sonication in deaerated water can separate the intercalated MXenes into discrete sheets because intercalation increases the interlayer spacing of multi-layered MXenes.[42] Both organic and ionic substances can serve as intercalants. Organic molecules, such as dimethyl sulfoxide (DMSO), urea, isopropyl amine, tetrabutylammonium hydroxide (TBAOH), hydrazine, and other polar organic molecules, act as intercalants in the separation of HF-synthesized MXenes, and for multi-layered MXenes generated with LiF + HCl or NH_4F etchants, Li^+ or NH_4^+ ions can intercalate between the layers.[67] These MXenes can thus be readily processed by sonication without additional intercalation, and monolayer MXenes can be obtained from HF-produced MXenes with shorter c-lattice parameters (Fig. 3e). Furthermore, monolayer MXenes produced using this technique contain fewer defects than those made with alternative methods.[68] Table 1 summarizes some of the synthesized MXenes.

Table 1 An overview of the synthesized MXenes

MXene	Initial component	Etchants	Temp. (°C)	Time (h)	Ref.
Ti_2CT_x	Ti_2AlC	HF	RT	10	55
V_2CT_x	V_2AlC	HF	RT	90	69
Ti_2NT_x	Ti_2AlN	HF	RT	24	70
$Ti_3C_2T_x$	Ti_3AlC_2	HF	RT	2	51
$Nb_4C_3T_x$	Nb_4AlC_3	HF	RT	96	71
$Mo_2TiC_2T_x$	Mo_2TiAlC_2	HF	RT	48	60
$Zr_3C_2T_x$	$Zr_3Al_3C_5$	HF	RT	60	54
Mo_2CT_x	Mo_2Ga_2C	LiF + HCl	35	384	72
$Cr_2TiC_2T_x$	Cr_2TiAlC_2	LiF + HCl	55	42	60
$Ti_3C_2T_x$	Ti_3AlC_2	NH_4HF_2	80	12	61
Ti_3CNT_X	Ti_3AlCN	LiF + HCl	35	12	73
Nb_2CT_x	Nb_2AlC	HF	RT	90	48
$(Ti_{0.5}Nb_{0.5})_2CT_x$	$(Ti_{0.5}Nb_{0.5})_2AlC$	HF	RT	28	56
$Ta_4C_3T_x$	Ta_4AlC_3	HF	RT	72	56
$V_4C_3T_x$	V_4AlC_3	HF	RT	165	59
$Mo_2Ti_2C_3T_x$	$Mo_2Ti_2AlC_3$	HF	RT	48	60
$Ti_4N_3T_x$	Ti_4AlN_3	KF + LiF + NaF	550	0.5	62
$T_3C_2T_x$	Ti_3AlC_2	NH_3F	150	24	74
V_2CT_x	V_2AlC	LiF + HCl	90	48	75
Mo_2CT_x	Mo_2Ga_2C	LiF + HCl	35	384	72
$Hf_3C_2T_x$	$Hf_3[Al(Si)]_4C_6$	HF	RT	60	76

2.2. Synthesis of MXene-based composites

In recent decades, manufacturing composites has become an increasingly common technique for developing stable and adaptable materials. Research on MXene-based composites has grown due to MXenes' exceptional suitability for creating multifunctional composites, owing to their 2D morphology, layered structures, and high flexibility. MXenes have been combined with various materials, including polymers, metal oxides, and carbon nanotubes, to produce a range of innovative new composites.

2.2.1. MXene-based polymer composites. MXenes, known for their superior mechanical properties, hydrophilic surfaces, and metallic conductivity, can significantly enhance polymers' thermal and mechanical characteristics when incorporated into composites. Single-layer MXenes are more compatible with polymers and offer higher accessible surface hydrophilicity than multi-layered MXenes. As a result, MXenes are often delaminated before being combined with polymers. This can be demonstrated by fabricating a single-layer $Ti_3C_2T_x$–polyvinyl alcohol (PVA) composite.[77] An aqueous PVA solution was combined with a colloidal suspension of $Ti_3C_2T_x$ films, resulting in a $Ti_3C_2T_x$–PVA composite (Fig. 4(a)). The high hydrophilicity of PVA allows it to form strong hydrogen bonds with $Ti_3C_2T_x$, which possesses high thermal stability. The $Ti_3C_2T_x$–PVA composite exhibited enhanced flexibility, tensile strength, and compressive strength compared to the individual $Ti_3C_2T_x$ and PVA components. Specifically, the $Ti_3C_2T_x$–PVA composite with 40 wt% $Ti_3C_2T_x$ had a tensile strength of approximately 91 ± 10 MPa, about four times higher than that of the $Ti_3C_2T_x$ film (Fig. 4(b)). This composite material also demonstrated excellent conductivity.

Additionally, a two-step process was used to develop a $Ti_3C_2T_x$–polyacrylamide (PAM) composite.[79] In the first step,

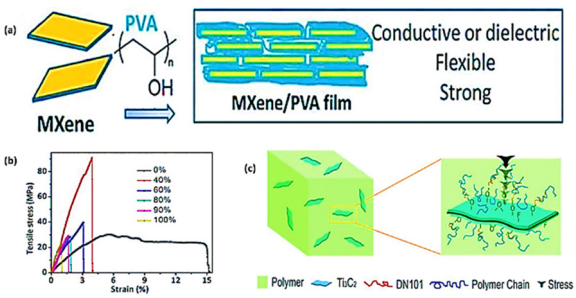

Fig. 4 (a) Schematic diagram of the synthesis of the $Ti_3C_2T_x$-PVA composite; (b) stress–strain curves for PVA films containing various weights of $Ti_3C_2T_x$[77] (Copyright (2014) PNAS); (c) diagrammatic illustration of forces functioning on the $Ti_3C_2T_x$–UHMWPE composite[78] (Copyright (2015) Elsevier).

dimethyl sulfoxide (DMSO) was introduced into the interlayers of $Ti_3C_2T_x$ to achieve complete delamination of the individual layers. This increases the layer gap of $Ti_3C_2T_x$. Afterwards, the prepared $Ti_3C_2T_x$ and PAM solutions are thoroughly combined and allowed to dry at room temperature for four to five days. By altering the mass ratio of $Ti_3C_2T_x$ to PAM, various $Ti_3C_2T_x$–PAM composites can be developed. The composite exhibits a maximum electrical conductivity of 3.3×10^{-2} S m^{-1} and high mechanical characteristics, with $Ti_3C_2T_x$ making up 6 wt% of the composite. It has also been reported that UHMWPE (ultra-high molecular weight polyethylene) can form composites with $Ti_3C_2T_x$. However, before fabricating the $Ti_3C_2T_x$–UHMWPE composite, surface-modified $Ti_3C_2T_x$ powders must be prepared; this modified surface can enhance the compatibility and dispersion properties of $Ti_3C_2T_x$ in UHMWPE.[78] The mixtures of surface-modified $Ti_3C_2T_x$ and UHMWPE are molded on an automated vulcanizer, heated at a rate of 10 °C min^{-1} to 220 °C, and held for 30 minutes under 10 MPa. Fig. 4(c) shows the technique by which $Ti_3C_2T_x$ improves the mechanical characteristics of UHMWPE. The exceptional mechanical performances of the $Ti_3C_2T_x$–UHMWPE composite can be attributed to the flexible $Ti_3C_2T_x$'s ability to withstand greater stress than UHMWPE and effectively prevent the formation and development of cracks. This is achieved by transferring stress from UHMWPE to $Ti_3C_2T_x$ along the polymer chains.

The modification of polymers is intended to assist in overcoming their inherent weaknesses, neutralize the charge on the surface of the nanoparticles, and stop the aggregation of the particles.[80] The photothermal effects and practical uses of MXenes are severely limited by their uncontrollable protein corona production and spontaneous aggregation in physiological settings. Dong *et al.* combined an acidic chitosan (CS) solution with $Ti_3C_2T_x$ suspension to create MX-CS hydrogels.[81] This allowed MRSA cell aggregation and MXene-induced hyperthermia around the hydrogel, thereby enhancing the photothermal effect and anti-MRSA activity (>99%). By cross-linking branching MXene@PDA, polyglycerol-ethyleneimine (PGE), and hyaluronic acid oxide (HCHO), biodegradable HPEM scaffolds were developed.[82] The scaffolds' electrical conductivity and thermal stability were enhanced by the addition of MXene@ PDA. By encouraging cell proliferation and angiogenesis, inducing the formation of granulation tissue, and operating as an effective anti-infection agent (99.03% efficacious MRSA inactivation), HPEM scaffolds can significantly speed up wound healing and skin reconstruction in MRSA-infected wounds. To create bio-ink and composite hydrogel scaffolds for 3D printing, $Ti_3C_2T_x$ was combined with gelatin methacrylate (GelMA), sodium alginate (Alg), and β-TCP.[83] This combination prevented the growth of bacteria and eliminated any bacteria that had already been attached to the scaffolds, which multiplied significantly when exposed to NIR irradiation. The scaffolds demonstrated long-term anti-infective effectiveness as they broke down, and MXene was gradually released. The bactericidal rate reached 98%, which can treat infected bone defects in the mandible. Due to their ability to impede the healing of wounds, bacterial infections and oxidative damage from different reactive oxygen species (ROS) represent a serious risk to human health. To create the multifunctional chiral supramolecular composite hydrogel system known as LPFEG-MXene, MXene is co-assembled with LPFEG.[84] This system demonstrated significant photothermal antimicrobial activity against *S. aureus*, *P. aeruginosa*, and *E. coli* and broad-spectrum ROS-scavenging antioxidant capacity. It also showed great potential for use in antimicrobial coatings and the healing of infected wounds. Natural cationic antimicrobial polymers and quaternary ammonium salts are examples of polymers having antibacterial qualities found in nature. Zeng *et al.* were inspired by different functional approaches for antifouling surfaces and self-assembled a polydopamine layer onto the surface of MXene.[85] They then added a quaternate polyethyleneimine derivative (PEIS) to the PDA layer by Michael's addition to obtain MXene-PEIS, an amphiphilic ionic polymer-functionalized surface. The combined action of MXene and quaternary ammonium groups on the antimicrobial led to the excellent antibacterial and anti-biofouling characteristics of the produced MXene-PEIS nanosheets (75% and 88% inhibition against *E. coli* and *S. aureus*, respectively). In general, the mechanical capabilities of MXene–polymer composites are superior to those of MXenes and polymers individually. Additionally, many exhibit strong electrical conductivity, making them suitable for wearable electronics.[86]

2.2.2. MXene-based metal and metal-oxide composites. Copper (Cu), silver (Ag), zinc (Zn), and other metal and metal oxide nanoparticles exhibit strong antibacterial properties and have been utilized in a wide range of applications. Oxidative stress, protein dysfunction, and membrane damage are the primary mechanisms by which these nanoparticles induce bacterial death.[87,88] Although silver nanoparticles (Ag NPs) have demonstrated excellent antimicrobial properties against various microorganisms, their use in biomedical applications is limited due to the instability of silver in the environment and the potential for cytotoxicity and *in vivo* retention at high doses.[89,90] Ag_2S has shown promise as a photothermal therapy (PTT) material. Still, its application in biomedical fields is constrained by its narrow bandgap of 0.9 eV, accelerating the recombination of photogenerated electrons and holes, thereby hindering the photocatalytic reaction. To overcome this challenge, by introducing $Ti_3C_2T_x$, the Ag_2S/Ti_3C_2 composite was developed.[91] In addition, Ti_3C_2 enhanced the composite's photocatalytic activity and ROS production while also improving the separation efficiency of the photogenerated charge carriers. Together, the Ag_2S/Ti_3C_2 composite reduced photodynamic therapy (PDT) and PTT by up to 99.99%, effectively accelerating the healing of infected mouse wounds. Conventional gold nanoparticles (AuNPs) are generally inert to bacteria; however, ultra-small gold nanoclusters (AuNCs) with a core size of less than 2 nm can penetrate bacterial cells and cause the accumulation of reactive oxygen species (ROS), disrupting bacterial metabolism and ultimately leading to cell death. These AuNCs have demonstrated strong antibacterial activity.[92] When AuNCs were conjugated to the surface of MXene nanosheets, synergistic antibacterial effects were

observed with an antibacterial rate greater than 98%.[93] Sharp MXene nanosheets can penetrate bacterial membranes, and the development of crumpled MXene-AuNC structures effectively hindered biofilm formation. Additionally, the hydrophobic surface of the crumpled structures prevents bacterial attachment, increasing the density of biocides and enhancing the bactericidal effect. Cu_2O is a semiconductor, and MXene is a conductor that creates stable Cu_2O-anchored MXene nanosheets, known as Cu_2O/MXene.[94] It demonstrated that adding MXene improved the electron–hole pair separation efficiency in Cu_2O and successfully enhanced the electric field. This led to greater ROS production and more effective bacterial eradication through the localized surface plasmon resonance (LSPR) phenomenon. Furthermore, Cu and Cu^{2+} ions can also cause harmful effects on bacteria, such as DNA denaturation. The combined antibacterial efficiency of Cu_2O/MXene against *S. aureus* and *P. aeruginosa* was significantly higher than that of either MXene or Cu_2O alone, reaching 95.59% and 97.04%, respectively, under the synergistic effect of Cu and MXene.

Porphyrins are commonly used as photocatalysts or photosensitizers due to their potent ability to trap visible light, low photogenerated electron–hole recombination, and rapid transfer of photogenerated carriers. ZnTCPP/$Ti_3C_2T_x$ was synthesized by using a hydrothermal method.[95] When exposed to visible light, ROS formation was observed in the ZnTCPP/$Ti_3C_2T_x$ group, while it was absent in the $Ti_3C_2T_x$ group. *In vitro*, antimicrobial tests revealed no significant change in bacterial survival in a dark environment. However, following 10 minutes of visible light exposure, ZnTCPP/$Ti_3C_2T_x$ demonstrated significantly higher inhibition rates against *S. aureus* and *E. coli*, with inhibition rates of 99.86% and 99.92%, respectively, compared to the $Ti_3C_2T_x$ group. Moreover, the results suggested that the enhanced photocatalytic activity of ZnTCPP/$Ti_3C_2T_x$ could facilitate wound healing. MXene, however, has limited capacity to scavenge ROS and cannot eliminate excess ROS surrounding the wound, leading to malignant oxidation and severe inflammatory reactions that hinder wound healing and cause discomfort for patients. Injectable multifunctional hydrogel scaffolds (FOM) were developed by doping anti-inflammatory CeO_2 nanoparticles and $Ti_3C_2T_x$ into dynamically cross-linked hydrogels to address this issue.[96] *In vitro* trials demonstrated that FOM could reduce oxidative stress, supply oxygen, and protect L929 cells in the wound microenvironment. Furthermore, FOM exhibited outstanding antibacterial capabilities, with 100% inhibition of *E. coli*, *S. aureus*, and MRSA. Hu *et al.* developed a hydrogel composed of natural polysaccharides, by incorporating Zn^{2+} and $Ti_3C_2T_x$.[97] Including Zn^{2+} enhanced the electrostatic interaction between the hydrogel and negatively charged bacteria, reducing the thermal conductivity distance of photothermal therapy (PTT) and increasing the photothermal conversion efficiency. This supported the involvement of the physical antibacterial mechanism. MXene causes physical damage to bacterial cell membranes, facilitating Zn^{2+} entry and exhibiting antibacterial properties. Combining Zn^{2+} and MXene resulted in potent antibacterial effects, promoting skin regeneration and wound healing.

2.2.3. MXene-based nano carbon composites. Many MXene/graphene hybrid composites have been developed with exceptional structural robustness, conductivity, flexibility, and distinctive electrical, electrochemical, and mechanical properties. These advantages stem from the high efficiency of MXene nanosheets as a hybridization matrix with graphene.[98–100] When these composites are used in a polyethylene glycol matrix, their through-plane thermal conductivity improves. At a thickness of 2.5 mm, the proposed composites demonstrated enhanced electromagnetic interference (EMI) shielding performance of around 36 dB.[101] Studies have shown that magnetic MXene ($Ti_3C_2T_x$)-reduced graphene oxide aerogels, tethered by magnetic nickel nano-chains, exhibit appropriate hydrophobicity, multifunctionality, and thermal insulation properties.[98] Furthermore, freeze-drying and reduction heat treatment techniques were employed to prepare MXene ($Ti_3C_2T_x$)–graphene oxide hybrid foams. These foams exhibited excellent EMI performance and enhanced electrical conductivity, making them ideal candidates for use in innovative and next-generation devices.[102] MXenes and graphene composites have also been applied to build innovative nanoscale systems with potential for drug delivery and cancer therapy/diagnosis.[103,104] Biocompatible MXene (Ti_2N) quantum dot-based devices, exhibiting excellent targeting, selectivity, and stability characteristics, have been proposed for photothermal therapy and cancer photoacoustic imaging applications.[105,106] However, graphene- and MXene-based nanostructures have also been used to develop antiviral and antimicrobial surface coatings, medical equipment (such as face masks), and innovative delivery systems for antiviral or antimicrobial drugs.[107] With excellent biocompatibility and effective multifunctionality, several MXene and graphene-based nanocomposites have been used in tissue engineering and regenerative medicine applications. For instance, Mi *et al.* introduced 3D-printed tissue-engineered bone scaffolds using MXene (Ti_3C_2)-based structures to repair bone defects.[108] MXene structures were incorporated into composite scaffolds made of sodium alginate and hydroxyapatite *via* 3D printing using an extrusion method to promote bone regeneration. These homogeneous scaffolds, with distinct macropore morphologies and structures, demonstrated notable mechanical strength, enhanced alkaline phosphatase activity, increased osteogenic gene expression, appropriate biocompatibility, and increased mineralized nodule formation and cell proliferation. They may effectively promote bone regeneration *in vivo*, offering excellent potential for bone repair.[108] MXene-based composites exhibited appropriate hydrophilicity due to functional hydrophilic groups, providing a favorable growth medium for mesenchymal stem cells derived from bone marrow.[109,110] The developed MXene–graphene hybrids have also found application as electrodes in ion batteries, flexible supercapacitors, and EMI shielding.[50,111] Nonetheless, there have been significant investigations into their use in biosensing. For example, MXene–graphene field-effect transistor sensors were developed to detect coronavirus and influenza viruses

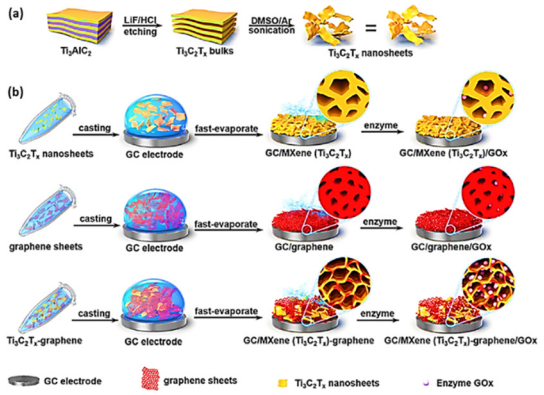

Fig. 5 (a) Synthesis of MXene nanosheets; (b) enzyme immobilization *via* MXene–graphene hybrid films for glucose biosensing application (GC = glassy carbon, DMSO = dimethyl sulfoxide, Gox = glucose oxidase, and LiF = lithium fluoride)[113] (Copyright (2019) American Chemical Society).

with high chemical sensitivity. These sensors utilize antibody–antigen binding to achieve electrochemical signal transduction after virus deposition onto the sensing material's surface. The detection limits were as low as ~125 copies mL^{-1} for the influenza virus and 1 fg mL^{-1} for the recombinant 2019-nCoV spike protein.[112] Furthermore, combining graphene and MXene structures can produce porous materials with a high capacity for enzyme binding, resulting in enhanced stability and affinity.[113] In one investigation, 3D porous $Ti_3C_2T_x$–graphene hybrid films were created using mixing-drying techniques and subsequently employed to develop biosensors for glucose detection (Fig. 5). The resulting biosensor exhibited appreciable electrochemical catalytic performance towards glucose biosensing, making it suitable for plasma glucose analysis. The internal pore size could be optimized by adjusting the ratio of MXene to graphene nanosheets, which would impact both glucose biosensing performance and the immobilization of glucose oxidase.[113]

Additionally, MXene ($Ti_3C_2T_x$)/graphene/polydimethylsiloxane layered structures developed through vacuum filtration and pre-polymerization primarily consisted of two layers: the flexible graphene/polydimethylsiloxane composite on the bottom layer and the MXenes on the top layer. These composite films can be used to create wearable strain sensors with a wide range of linear responses, high sensitivity (with a low detection limit of approximately 0.025%), excellent linearity ($R^2 > 0.98$), and remarkable cycling stability (over 5000 cycles).[114] These sensors are handy for the precise monitoring of full-range human motions. Sensors based on layer-structured homogeneous MXene ($Ti_3C_2T_x$)–graphene oxide films offer flexibility, conductivity, and cycling stability advantages.[115] In another study, graphene–MXene composites were used to develop an aerosol jet-printed flexible bimodal sensor. This temperature sensor demonstrated competitive thermoelectric power output (53.6 μV $°C^{-1}$) with high sensitivity, accuracy, stability, and flexibility (showing minimal degradation after 1000 bending cycles), creating numerous opportunities for producing multifunctional devices with biological applications.[116] By using graphene oxide to prevent MXene oxidation, these MXene–graphene composites exhibited long-term stability. The unique properties of these materials—such as high biocompatibility and linear sensitivity to humidity—warrant further investigation for their potential use in biological and healthcare devices, including smart actuators (*e.g.*, respiratory monitoring sensors).[115] Additionally, MXene-reduced graphene oxide aerogels were used to create 3D aerogel-based piezoresistive sensors with exceptional linear sensitivity (331 kPa^{-1} from 0 to 500 Pa and 126 kPa^{-1} from 500 Pa to 7.5 kPa) and good conductivity.[117] These sensors showed fast response times (load 71 ms, recovery 15 ms), low detection limits (1.25 Pa), and excellent performance and stability (even after 17 000 compression cycles). They hold potential for developing sensors capable of real-time detection of human respiration, heartbeat, and vocalization, demonstrating their future potential in flexible wearable electronics.[117]

3. Properties

In general, MXenes have the advantages of 2D materials, such as mechanical resilience, huge specific surface area, high Young's modulus, thermal/electrical conductivity, ultrathin architectures and adjustable band gap.[118–120] Notably, MXenes differ from most 2D materials due to their hydrophilic surfaces and strong metallic conductivity.[121,122] As reinforcements for multi-responsive functions, MXenes are particularly appealing due to a number of additional characteristics. Last but not least, (i) composition (such as solid solution and various transition metal "M" and "X" elements), (ii) surface functionalisation (*via* chemical and thermal treatment), and (iii) structure/morphology alteration can be used to adjust their properties and applications.[123–125] Here, we discuss the main properties of MXenes and MXene based composites (Table 2).

3.1. Electronic properties

Because of their high compositional diversity, various surface functionalization options, and controllable thickness, MXenes exhibit a wide range of electronic properties, from metallicity and semiconductivity to topological insulativity.[126–128] Most surface-functionalized MXenes and all bare MXenes are metallic. The work functions (WFs) of metallic MXenes vary significantly, ranging from 1.8 eV to 8 eV, as shown in Fig. 6.[127] It is evident that the WFs of MXenes depend on their surface chemistry: for a given MXene, the presence of OH (O) groups consistently decreases or increases the WF compared to the bare surface, while F decoration can either increase or decrease the WF, depending on the specific material. Notably, all OH-terminated MXenes exhibit ultralow WFs (<2.8 eV), which are lower than those of scandium (Sc) and among the lowest of any elemental metal. In contrast, platinum (Pt) has the highest WF among elemental metals, and some O-terminated MXenes have WFs even higher than that of Pt. MXenes with F-termination generally have WFs between OH- and O-terminated MXenes.

Table 2 An overview of the properties of MXenes

Properties	Description	Range
Electronic properties	MXenes exhibit various electronic properties, from metallicity and semiconductivity to topological insulativity. The work functions of metallic MXenes vary significantly, ranging from 1.8 eV to 8 eV	Electrical conductivity = 9880 S cm^{-1}
Mechanical properties	MXenes possess good mechanical properties and excellent mechanical flexibility due to their strong M–N and M–C bonding	Young's modulus = 400–1000 GPa Tensile strength = 8.2 MPa
Optical properties	MXenes are highly useful for photothermal treatment applications due to their potential to absorb light energy in the UV–visible range, specifically between 300 and 500 nm wavelengths	Transmittance = 91%
Thermal properties	MXenes exhibit strong thermal conductivity due to their electrical conductivity	722 W m^{-1} K^{-1}
Magnetic properties	MXenes are nonmagnetic in nature. The magnetism in some MXenes typically arises from unpaired electrons in surface transition metal atoms; thus, most of their magnetism is expected to be affected by surface passivation	The difference between the Fermi level and the maximum of the occupied spin-down band is large (2.9 eV), indicating that 100% spin-filter efficiency can be preserved in a broad bias range

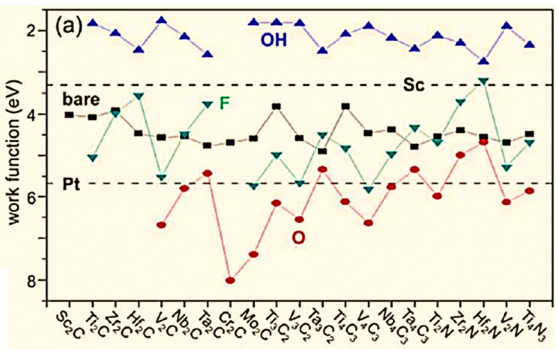

Fig. 6 Work functions of MXenes with varying terminations: dashed lines show the work functions of Sc and Pt for comparison. Bare, O-terminated, OH-terminated, and F-terminated MXenes are denoted by black squares, red circles, blue up-triangles, and cyan down-triangles, respectively[127] (Copyright (2016) American Chemical Society).

Surface functionalization alters the surface dipole moment, leading to changes in the WF.[127]

Xu *et al.* estimated the work function of $Ti_2C(OH)_xF_y$ to be 4.98 eV. Metallic MXenes with high or low WFs show significant potential as Schottky-barrier (SB)-free metal contacts to 2D semiconductors. The weak interfacial van der Waals (vdW) interaction and the high or low work function of MXenes allow for weak Fermi level fixation, facilitating SB-free hole (electron) injection into the 2D semiconductor. It has been predicted that typical 2D semiconductors, such as transition metal dichalcogenides and blue phosphorene, can form n-type Schottky barrier-free contacts with OH-terminated MXenes with ultralow WFs.[127,129,130] MoS_2, a well-known 2D semiconductor, is of great interest due to its potential to replace silicon in next-generation nanoelectronics.[131,132] However, making an SB-free p-type contact with MoS_2 remains challenging due to its high ionization energy of approximately 6.0 eV. Research indicates that six materials (V_2CO_2, Cr_2CO_2, Mo_2CO_2, $V_4C_3O_2$, Cr_2NO_2, and V_2NO_2) can be used as metal contacts to MoS_2, resulting in MoS_2–MXene interfaces with disappearing p-type Schottky barriers. This enables highly efficient hole injection into MoS_2.[133] Consequently, implementing high-performance MoS_2 field-effect transistors with both polarities will be more feasible.

3.2. Mechanical properties

The mechanical properties of MXenes are particularly intriguing due to their strong M–N and M–C bonding. Previous simulations suggest that the elastic parameters of MXenes should be approximately twice as large as those of MAX phases and that 2D materials like CdS_2 should be used. Despite having elastic parameters 2–3 times smaller than those of graphene, MXenes exhibit exceptional bending stiffness (1050 GPa), confirming their potential as reinforcing materials in composites. MXenes interact more effectively with polymeric matrices than graphene in composite applications.[134] The $Ti_3C_2T_x$ monolayer has a Young's modulus of 333 ± 20 GPa, which is higher than that of graphene oxide and MoS_2 but still considerably lower than the 386 GPa value of $Ti_3C_2O_2$.[135] Challenges such as the lack of surface control over MXenes, geometric vacancies, and weak interfaces in composite materials have impacted mechanical estimations. Therefore, new experimental work should focus on understanding how the synthesis process affects defect formation and the functional groups of pristine MXenes.[136] A thorough evaluation of mechanical properties and functional groupings based on theoretical and experimental data may still be necessary. Additionally, the mechanical properties of MXenes are influenced by the number of atomic layers, denoted by n in the chemical formula $M_{n+1}X_n$. For functionalized MXenes, the hardness and strength of $M_{n+1}X_nT_x$ increase as 'n' decreases.[137] Experiments have shown that adding carbon nanotubes or polymers to MXene composites can enhance their mechanical properties. Various polymer combinations can improve MXene's toughness, tensile and compressive strengths, and flexibility to varying extents. For example, the polyvinyl alcohol (PVA)–$Ti_3C_2T_x$ composite exhibits significant compressive and tensile strengths and outstanding flexibility. Specifically, the tensile strength of $Ti_3C_2T_x$–PVA composites is approximately four times higher than that of $Ti_3C_2T_x$ alone.[79] Additionally, $Ti_3C_2T_x$–PAM and

$Ti_3C_2T_x$–UHMWPE composites have shown good toughness and yield strength.[78,138]

3.3. Optical properties

Optical properties are crucial for applications in photovoltaic, photocatalytic, transparent, and optically conductive electrode devices, as they depend on visible and ultraviolet light absorption. $Ti_3C_2T_x$ films can potentially absorb light energy in the UV–visible range, specifically between 300 and 500 nm wavelengths.[139] Even at a film thickness of 10 nm, these films exhibit 91% transmittance. Moreover, depending on the film thickness, $Ti_3C_2T_x$ films can absorb a broad and strong band of light between 700 and 800 nm, resulting in pale green coatings that are highly useful for photothermal treatment applications.[140] Interestingly, both film thickness and ion intercalation can slightly optimize transmittance. For instance, Verger *et al.* found that the transmittance of $Ti_3C_2T_x$ films was reduced by urea, hydrazine, and DMSO but increased from 75% to 92% when treated with tetramethyl ammonium hydroxide.[141]

3.4. Thermal properties

Thermal stability, thermal conductivity, and thermal expansion characteristics are the essential aspects of a material's thermal properties. MXenes exhibit strong thermal conductivity due to their electrical conductivity, which is comparable to that of graphene. When combined with a polymer, MXenes can enhance the polymer's heat conductivity. Cao *et al.* developed MXene/PVDF nanocomposites using solution mixing. The composite with just 5 wt% MXene showed a thermal diffusivity of 0.167 $mm^2\ s^{-1}$ and a thermal conductivity of 0.363 $W\ m^{-1}\ K^{-1}$, roughly twice as high as that of pure PVDF.[142] MXenes are used to enhance the thermal conductivity of polymer materials.[143–145] It was noted that the nanosheet structure of MXenes allows them to form hydrogen and chemical bonds with polymers, acting as a bridge in the composites and creating a network for heat conduction that facilitates heat transfer between polymer chains. Additionally, MXenes reduce the volatility of the polymer chain arrangement, which decreases thermal vibrations and phonon scattering, further improving thermal conductivity.[145] Moreover, MXenes, being inorganic nanoparticles, significantly enhance the heat resistance of polymer materials. Ti_3C_2 was incorporated into linear low-density polyethylene (LLDPE) to create MXene/LLDPE nanocomposites. In thermal glass transition (T_g) experiments, the average values of T20%, T40%, and T_{max} increased, indicating that the nanocomposite improved thermal stability.[146] The thermal stability of synthesized $Ti_3C_2T_x$/PVA composites was significantly enhanced compared to pure $Ti_3C_2T_x$ and pure PVA, as evidenced by higher degradation and oxidation temperatures.[143] By adding functionalized MXenes to a chitosan (CS) matrix, hybrid membranes were developed, which significantly increased thermal stability.[147] MXene composites also enhance heat radiation, contributing to increased thermal conductivity and improved thermal stability. The barrier effect of MXenes helps boost heat resistance by preventing volatile compounds from escaping the bulk polymer during degradation, thus improving heat resistance.[142,146]

3.5. Magnetic properties

Most of the 2D materials discovered so far are nonmagnetic, which limits their application in spintronics. Consequently, pursuing controlled magnetism in two-dimensional materials has been a longstanding goal. Interestingly, some pristine MXenes, such as Ti_2C, Ti_2N, Cr_2C, Cr_2N, and Mn_2C, are predicted to be intrinsic magnetic materials. Specifically, Mn_2C and Cr_2N are antiferromagnetic, while Ti_2C, Ti_2N, and Cr_2C exhibit ferromagnetic properties.[148–151] Recently, magnetic MXenes with half-metallicity have garnered significant attention. Half-metals have fully spin-polarized electrons at the Fermi level, with one spin channel being metallic and the other semiconducting. Cr_2C is the first half-metal anticipated within the MXene family.[149] Fig. 7(a) shows its band structure, with visible metallic spin-up and insulating spin-down channels. The half-metallic gap between the maximum of the occupied spin-down band and the Fermi level is approximately 2.9 eV, indicating that a wide bias range can maintain 100% spin-filter efficiency. Consequently, predictions of half-metallicity have also been made for Ti_2C and Ti_2N.[152] Surface functionalization can significantly alter the magnetic and electronic properties of bare MXenes. The magnetism in bare MXenes typically arises from unpaired electrons in surface transition metal atoms; thus, most of their magnetism is expected to be affected by surface passivation. Some MXenes, particularly those containing Cr and Mn, retain their magnetic properties after surface functionalization.

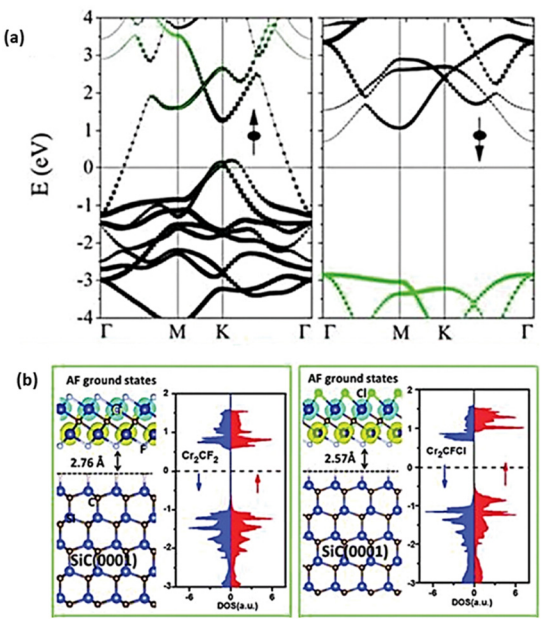

Fig. 7 (a) The Cr2C band structure[149] (Copyright (2015) American Chemical Society); (b) density of states of Cr_2CFCl (right panel) and Cr_2CF_2 (left panel) on a SiC (0001) substrate[153] (Copyright (2016) Royal Society of Chemistry).

Functional groups can impact their electronic structures and magnetic couplings. For example, Cr_2C changes from a ferromagnetic half-metal to an antiferromagnetic semiconductor with a large band gap when functionalized with –F, –H, –OH, or –Cl groups.[154] Conversely, surface passivation with O transforms Cr_2N from an antiferromagnetic metal to a ferromagnetic half-metal, unlike Cr_2C.[155,156] The ferromagnetic–antiferromagnetic transition in Cr_2C appears to be induced by symmetrical and asymmetrical functionalization. As opposed to symmetrical functionalization, asymmetrical functionalization introduces additional modifications to the electronic structure of Cr_2C. The density of states (DOS) for Cr_2CF_2 (left panel) and Cr_2CFCl (right panel) are shown in Fig. 7(b).[153] Compared to the symmetrical distribution of Cr_2CF_2, Cr_2CFCl exhibits characteristics of bipolar magnetic semiconductors, where the conduction band minimum (CBM) and the valence band maximum (VBM) have opposite spin polarizations. Other MXene composites, such as Cr_2CFCl, Cr_2CClBr, Cr_2CHCl, Cr_2CHF, and Cr_2CFOH, exhibit similar bipolar magnetic characteristics, making them promising candidates for spintronic applications.[153]

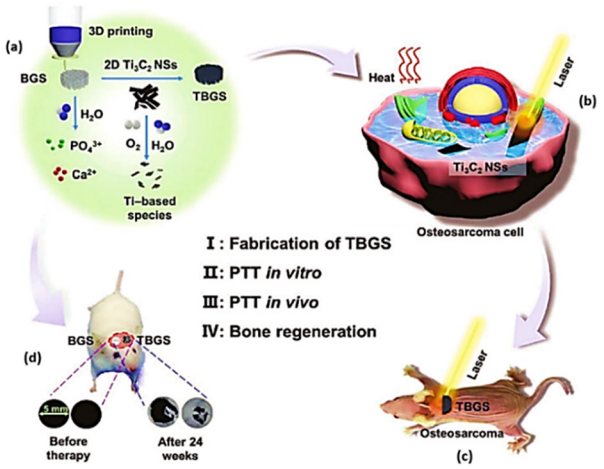

Fig. 8 Schematic diagram of the development of TBGS: (a) Ti_3C_2 MXene integration, degradation of the Ti_3C_2 MXene on BGS and 3D printing of pure BGS constitute all steps in the fabrication process of TBGS; *in vitro* (b) and *in vivo* (c) photothermal ablation of osteosarcoma cells carried out with TBGS; (d) bone-tissue repair and therapeutic outcomes for BGS and TBGS implantation[159] (Copyright (2019) John Wiley and Sons).

4. Biomedical applications of MXenes and MXene-based composites

4.1. Tissue engineering

MXenes have shown remarkable potential in materials sciences and stem cell-based tissue therapies.[109] Titanium carbide (Ti_3C_2) MXene nanofibers have been used to develop innovative biomaterials for cell culture and tissue engineering. Due to the presence of various functional hydrophilic groups, these hydrophilic composite nanofibers can be synthesized through electrospinning and doping.[109] The functional groups on the surfaces of MXene nanofiber composites may provide suitable environments for cell proliferation. The biochemical properties were assessed using bone marrow-derived mesenchymal stem cells (BMSCs). The resulting MXene composite nanofibers exhibited excellent biocompatibility, significantly enhanced cellular activity, and promoted the differentiation of BMSCs into osteoblasts.[157] Such innovative biomaterials with distinct multi-biological properties are ideal for tissue engineering and repair.[158] For instance, zero-dimensional (0D) Ti_3C_2 MXene-based quantum dots (QDs) have been utilized for immunomodulation to enhance tissue repair following injury. These 2D structures, which are compatible with BMSCs, were able to selectively reduce human $CD4^+$ IFN-γ^+ T-lymphocyte activation while promoting the expansion of immunosuppressive $CD4^+CD25^+$ $FoxP3^+$ regulatory T-cells in a stimulated lymphocyte population. Ti_3C_2 MXene QDs were incorporated into a chitosan hydrogel to create a 3D platform with improved physicochemical properties for tissue repair and stem cell delivery. The hydrogel composite maintained injectability and thermal sensitivity while demonstrating good conductivity.[158] Surgical failure and bone tumor recurrence remain significant concerns due to residual malignant tumor cells and inadequate bone-tissue integration.[159] As a result, developing multifunctional therapeutic platforms for effective tumor treatment and bone regeneration has become essential. One potential application is the integration of the 2D Ti_3C_2 MXene with 3D-printed bioactive glass scaffolds to combine photonic hyperthermia for simultaneous tumor ablation and bioactive scaffolds for bone tissue reconstruction (Fig. 8).[159] The composite scaffolds were designed with optimal characteristics to achieve bone-tumor ablation using near-infrared (NIR)-triggered photothermal hyperthermia and remove the entire tumor from *in vivo* bone-tumor xenografts. Integrating the Ti_3C_2 MXene into composite scaffolds can potentially enhance the *in vivo* growth of new bone tissue within bioactive glass scaffolds. These scaffolds, which offer the dual benefits of tumor ablation and bone tissue regeneration, represent a promising alternative to other tissue engineering devices for treating bone tumors.[159]

In the NIR-II biological window, a soluble 2D MXene (Nb_2C nanosheets) system was developed using polyvinylpyrrolidone microneedles for medical implantation and photothermal tumor elimination.[160] The high-functioning photothermal nano agents, Nb_2C nanosheets, were incorporated into a biocompatible polyvinylpyrrolidone matrix. This resulted in a microneedle system with sufficient skin penetration and distinctive solubility. Upon insertion into the tumor site, the microneedles rapidly break down and release the nanosheets. Due to their excellent biocompatibility and minimal toxicity or adverse effects, these microneedle devices hold promise for safe, effective, and minimally invasive localized therapy.[160] On the other hand, designing and manufacturing conductive cardiac patches to improve electrical coupling with the host tissue represents a promising approach to enhancing heart tissue regeneration. The alignment of myofibrils into bundles and their organization within the ventricular myocytes significantly impacts heart tissue functionality.[161] Although aerosol jet

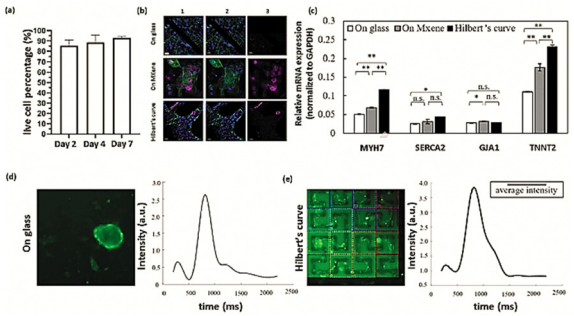

Fig. 9 (a) Viability percentage of iCMs on the $Ti_3C_2T_x$ MXene-PEG hydrogel; (b) immunostaining characterization included three methods: (1) connexin-43 staining, (2) sarcomeric alpha-actinin staining and (3) combination of connexin-43 and sarcomeric alpha-actinin staining. The straight-line patterned MXene printed on glass, the unpatterned $Ti_3C_2T_x$ MXene, and Hilbert's curve-patterned $Ti_3C_2T_x$ MXene printed on PEG were utilized for immunostaining characterization; (c) Qrt-PCR analysis of the relative mRNA expression of the cardiac markers MYH7, SERCA2, GJA1, and TNNT2; (d) an individual image obtained during the calcium flux timelapse recording of an on-glass sample (left) and the calcium flux timelapse image's intensity (right); (e) the average intensity of calcium flux and time (right) and a single snapshot from the calcium flux timelapse recording of the $Ti_3C_2T_x$ MXene-PEG hydrogel (left) (the pattern was categorized into 16 groups, each of which is depicted with a distinct colour)[162] (Copyright (2022) Elsevier).

printing (AJP) offers high resolution and can print on soft and hard tissues, it is especially suitable for producing cell-scale printed patterns. This technology enables the creation of hybrid tissue frameworks and allows printing on hydrogels of various shapes.[162] Using AJP, MXene-integrated composites were prepared for human cardiac patches. The conductive $Ti_3C_2T_x$ MXene was printed in specific patterns onto a polyethylene glycol (PEG) hydrogel, and the electroconductive cardiac patches were aligned with human-induced pluripotent stem cell-derived cardiomyocytes (iCMs).[162] To study cell attachment and alignment, $Ti_3C_2T_x$ was printed on various substrates, including glass, GelMA, and PEG hydrogels. Among the scaffolds created, $Ti_3C_2T_x$ MXene-PEG hydrogels exhibited excellent alignment of iCMs with high vitality (Fig. 9(a and b)). qRT-PCR analysis of Hilbert's curve-patterned glass samples showed a significant increase in the relative mRNA expression of cardiac markers compared to straight line-patterned glass samples, indicating better iCM maturity (Fig. 9(c)). Contraction dynamics of the cardiac patches were evaluated by investigating Ca^{2+} handling and conduction velocity (Fig. 9(d and e)). The results demonstrated that the addition of $Ti_3C_2T_x$ MXene to non-conductive hydrogels increased the synchronous beating rate of iCMs. Additionally, injectable shape-memory composite tissue scaffolds were developed for *in vitro* applications by incorporating Ti_3C_2 MXene quantum dots into chitosan-based hydrogels.[158] In another related study, chitosan-based hydrogels with honey, Ti_3C_2 MXene, and 0D fluorescent carbon dots were created and applied to tissue engineering. These hydrogels exhibited favorable compatibility with various stem cell types and demonstrated antibacterial and anti-inflammatory properties.[163] Another investigation incorporated $Ti_3C_2T_x$ nanosheets into a reduced graphene oxide hydrogel to explore diverse applications, including tissue engineering possibilities.[164] It indicated that MXene-based bio-composites exhibited immunomodulatory and anti-inflammatory qualities, which make them ideal for tissue engineering applications.[96,165] Here, we also discuss various uses of MXene-based nanocomposites in tissue engineering and regenerative medicine (Table 3).

4.2. Detection and treatment of cancer

Recently, there has been increasing attention on nanocomposites made from two or more constituent materials.[174] The significance of 2D MXenes in creating multifunctional nanocomposites is recognized due to their distinct structural features, metallic conductivity, rich surface chemistry, large surface area, biocompatibility, hydrophilicity, and adjustable particle size.[175–177] MXenes possess a variety of functional groups on their surfaces, allowing them to readily hybridize with other materials such as polymers, MnO_x, zinc oxide, mesoporous silica nanoparticles, Au nanoclusters, surface-superparamagnetic iron oxide, g-C_3N_4, MnO_x, and zinc oxide.[93,178–186] This versatility enables the development of advanced functional nanocomposites with enhanced therapeutic functionalities, including combinations of photodynamic and chemodynamic therapies and multimodal imaging capabilities, which cannot be achieved by single MXene nanosheets alone.[187] Specific examples of MXene-integrated nanocomposites for cancer treatment are summarized in Table 4.

Nanocomposites of Ti_3C_2/g-C_3N_4 have been developed to combine photothermal therapy (PTT) with *in situ* oxygen generation to enhance photodynamic therapy (PDT).[185] The integration of Ti_3C_2 with g-C_3N_4 can significantly boost the absorption of g-C_3N_4 in the near-infrared spectrum, which in turn enhances the photocatalytic activity of the resulting

Table 3 MXene-based nanocomposites in tissue engineering and regenerative medicine

MXene nanocomposites	Targeted tissue	Therapy	Ref.
$Ti_3C_2T_x$ MXene nanosheets	Skin	PTT	82
MXene/hydroxyapatite nanoparticle composite nanofibers	Bone	PTT	166
Nb_2C@TP (Nb_2C MXene titanium plate)	Skin	—	167
Nb_2C MXene-integrated 3D-printed bone-mimetic scaffold	Bone	PTT	168
Muscle-inspired MXene/PVA hydrogel	Skin	PTT	169
MXene–amoxicillin–PVA nanofibrous membrane	Skin	—	170
Silica@Nb_2C MXene-integrated 3D-printing bioactive glass scaffolds	Bone	—	171
Chitosan–hyaluronate hydrogel@$Ti_3C_2T_x$ MXene nanocomposites	Skin	—	172
Ultralong hydroxyapatite nanowires/titanium carbide nanocomposite	Bone	PTT	173

Table 4 MXene nanocomposite incorporation for cancer treatment

MXene nanocomposite	Cancer	Treatment	Ref.
Carbon dot@$Ti_3C_2T_x$	Breast	Sonodynamic therapy (SDT)/photothermal therapy (PTT)	188
Ti_3C_2@chitosan–$MnFe_2O_4$	Pancreatic	Chemodynamic therapy (CDT)/photothermal therapy (PTT)/magnetic resonance imaging	189
MXene@agarose/TNF-α	Colorectal carcinoma	Chemotherapy/photothermal therapy (PTT)	190
Nb_2C plasmon (MXene)/Pt nanozymes/doxorubicin (DOX)	Cervical carcinoma	Chemotherapy/photothermal therapy (PTT)	191
MXene@hydrogel	Melanoma	Chemotherapy/photothermal therapy (PTT)	192

nanocomposites and increases the generation of reactive oxygen species (ROS). The ROS generation and mitochondria-targeted nanomedicine were further developed by modifying Ti_3C_2/g-C_3N_4 with triphenylphosphonium bromide (Ti_3C_2/g-C_3N_4-TPP).[185] Under near-infrared (NIR) irradiation, synergistic type I and type II PDT can occur (Fig. 10(a)). Ti_3C_2/g-C_3N_4 nanosheets (NSs) can generate abundant O_2 in type II PDT through the breakdown of endogenous water when exposed to light. This energy transfer to O_2 initiates the creation of cytotoxic singlet oxygen ($^1O_2$).

In type I PDT, electrons from the valence band (VB) of g-C_3N_4 are energized to the conduction band (CB), producing photoactivated electrons and holes.[185] The excited holes react with water molecules to generate hydroxyl radicals ($^\bullet$OH). Additionally, excited electrons from g-C_3N_4 may migrate to Ti_3C_2, reducing O_2 to generate superoxide anions (O_2^-), a potent ROS. Electron spin resonance spectra of g-C_3N_4 and Ti_3C_2/g-C_3N_4 (670 nm laser, 0.48 W cm^{-2}) verified the generation of ROS, including $^\bullet$OH, O_2^-, and $^1O_2$. Under 808 nm laser irradiation, Ti_3C_2/g-C_3N_4 nanocomposites exhibited excellent photothermal effects at various concentrations (Fig. 10(b)).[185] *In vitro* experiments showed that the zeta potential of Ti_3C_2/g-C_3N_4 nanocomposites increased from −4.5 to −22.4 mV compared to pure Ti_3C_2 nanosheets. The zeta potential was further enhanced to 7.6 and −3.0 mV, respectively, by modifying the surface with TPP and $PEGNH_2$. This improvement provided exceptional physiological stability in Dulbecco's modified Eagle's medium (DMEM), fetal bovine serum (FBS), and phosphate-buffered saline (PBS, pH = 7.4, 10 mM), which is essential for *in vivo* applications.

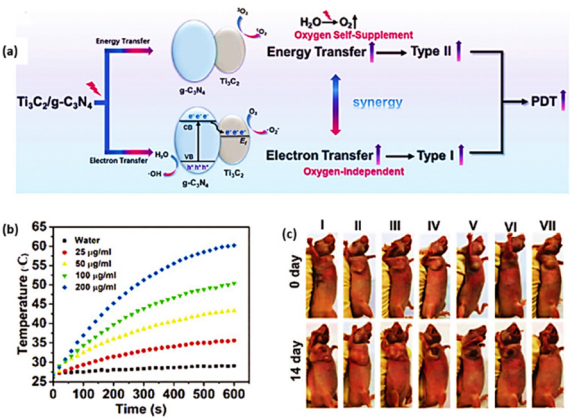

Fig. 10 (a) Ti_3C_2/g-C_3N_4 nanocomposite illustrated as a photosensitizer for enhanced PDT by the cooperative action of type I and type II routes when exposed to near-infrared radiation; (b) Ti_3C_2/g-C_3N_4 nanocomposites at different concentrations exposed to an 808 nm laser (0.8 W cm^{-2}) *via* photothermal heating curves; (c) after two weeks of various treatments, images of MCF-7 tumour-bearing mice: (I) PBS (pH = 7.4, 10 mm); (II) PBS (pH = 7.4, 10 mm) reflected by a 670 nm laser (0.48 W cm^{-2}) and 808 nm laser (0.8 W cm^{-2}); (III) Ti_3C_2/g-C_3N_4-TPP; (IV) Ti_3C_2/g-C_3N_4 reflected by a 670 nm laser (0.48 W cm^{-2}); (V) Ti_3C_2/g-C_3N_4 reflected by an 808 nm laser (0.8 W cm^{-2}); (VI) Ti_3C_2/g-C_3N_4 reflected by a 670 nm laser (0.48 W cm^{-2}) and 808 nm laser (0.8 W cm^{-2}); and (VII) Ti_3C_2/g-C_3N_4-TPP reflected by a 670 nm laser (0.48 W cm^{-2}) and 808 nm laser (0.8 W cm^{-2}). The experimental irradiation time was five minutes[185] (Copyright (2020) Elsevier).

A strong anticancer efficacy of Ti_3C_2/g-C_3N_4-TPP nanocomposites was demonstrated through *in vivo* multimodal PTT and PDT in tumor-bearing mice (Fig. 10(c)).[185] PTT can be combined with various therapeutic approaches, such as photodynamic therapy,[193] radiation,[194] and immunotherapy,[195] for effective cancer treatment. Zhang *et al.* developed a composite with cellulose-based hydrogels and Ti_3C_2 MXene loaded with the chemotherapeutic drug doxorubicin (DOX). They demonstrated the composite's good photothermal properties, high DOX loading capacity, and optimal biocompatibility for this dual-modality photothermal/chemotherapy system.[196] The drug effectively destroyed tumor cells and prevented recurrence when released in response to photothermal action. Deng *et al.* recently described a novel multifunctional hydrogel known as SP@MX-TOB/GelMA, synthesized with Ti_3C_2 nanosheets, gelatin methacrylate (GelMA), sulfonated polyetheretherketone (SP), and tobramycin (TOB).[197] The hydrogel demonstrated effective photothermal properties, successfully killing osteosarcoma cells and *E. coli* and *S. aureus* bacteria. It also showed favorable osseointegration, biocompatibility, and osteogenic activity for pre-osteoblasts. In another development, composite nanosheets containing Ta_4C_3 (tantalum carbide) MXenes were created for multiple imaging-guided photothermal tumor removal (Fig. 11).[180] These nanosheets initiated a redox reaction on their surfaces, facilitating the *in situ* formation of manganese oxide nanoparticles. The integrated MnO_x section of the produced composites was modified to function as the tumour microenvironment-receptive contrast entity for T1-weighted MRI, and the tantalum portions might serve as superior contrast means for contrast-boosted computed tomography (CT). With appropriate contrast-enhanced photoacoustic imaging applications, the photothermal-translation activity of the

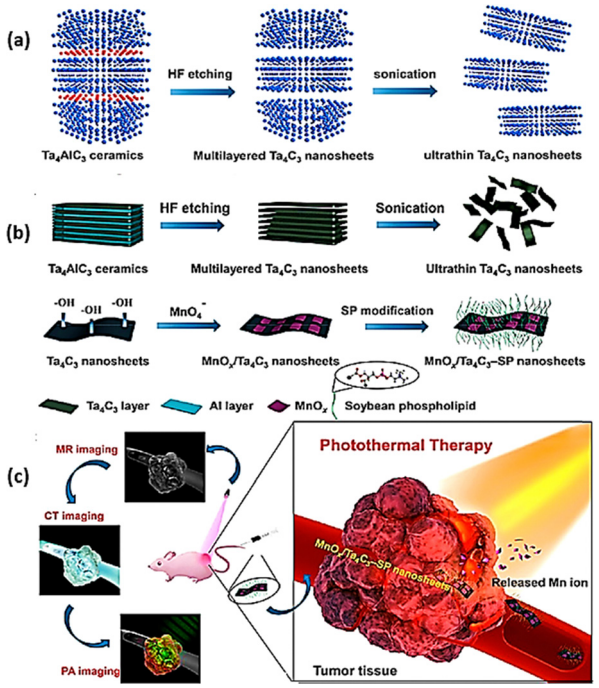

Fig. 11 Schematic diagram of the synthesis process and photothermal tumour therapy with MnO_x/Ta_4C_3–SP composite nanosheets influenced by MR/CT/PA imaging. (a) The ball-and-stick model-based exfoliation approach for 2D Ta_4C_3 nanosheets consists of HF etching and sonication exfoliation; (b) the technique to develop MnO_x/Ta_4C_3-SP nanocomposite sheets involves several steps, like HF etching, sonication exfoliation, an *in situ* redox reaction between Ta_4C_3 nanosheets and post-introduced $KMnO_4$, and surface SP modification; (c) schematic diagram of theranostic properties of MnO_x/Ta_4C_3–SP nanocomposite sheets, *i.e.*, effective PTT ablation of cancer influenced by MR/CT/PA imaging[180] (Copyright (2017) American Chemical Society).

developed MXene-based nanosheets could significantly limit tumour growth by photothermal hyperthermia.[180]

By combining an engineered exosome vector with vanadium carbide (V_2C) quantum dots that have appropriate photothermal activity in the NIR-II range, Cao *et al.* proposed a novel approach to increase the therapeutic efficiency of PTT (Fig. 12). These quantum dots targeted the tumour cells. They entered their nuclei, destroying them both *in vivo* and *in vitro*. The developed nanosystem exhibited a prolonged circulation time, high biocompatibility with the capacity to escape endosomes, and potential for clinical applications.[198] Ultrathin 2D molybdenum carbide (Mo_2C) MXenes were developed for photonic tumour hyperthermia.[199] The substantial NIR absorption, encompassing NIR-I and -II, the first and second biological transparency windows, was demonstrated using computational simulation, a unique approach for photonic-performance prediction. Following external engineering modification, Mo_2C-PVA nanoflakes were produced with poly(vinyl alcohol) (PVA). These nanoflakes demonstrated excellent biocompatibility and quick biodegradability. In addition to exhibiting an intriguing broad absorption band spanning NIR in the I and II regions, subsequent nanoparticles had an optimal photothermal-translation efficiency (43.3% for NIR-II and 24.5% for NIR-I).[199]

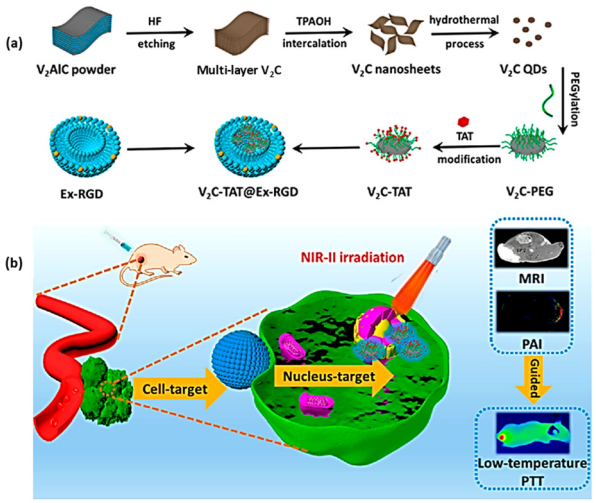

Fig. 12 Schematic diagram of the (a) synthesis process of V2C-TAT; (b) dual-target V2C-TAT@Ex-RDG nano agent for the cancer cell membrane and nucleus for multimodal imaging-guided PTT in the NIR-II bio-window at low temperature (Ex = exosomes and RDG = Arg-Gly-Asp)[198] (Copyright (2019) American Chemical Society).

4.3. Sensors

4.3.1. Biosensors in conjunction with wearable electronics. MXene-based components have been actively and passively utilized as electrocatalysts and redox transducers to detect biomarkers, environmental pollutants, pharmaceuticals, and nanoparticles.[200] The expansion of MXenes' application in the sensor domain is primarily attributed to their chemical characteristics and easily adjustable surface functionalization.[201]

Given these advantages, MXenes have gained popularity across various sensors, including optical/electrochemical, gas/humidity, and stress/strain sensors. However, MXenes have van der Waals interactions between neighboring sheets, which lead to a small interlayer gap and substantial aggregation. This aggregation limits their potential applications.[202,203] To enhance the properties of MXenes, expanding the interlayer gap to increase surface area, create additional active sites, and widen ionic transportation channels could be beneficial.[204] For instance, developing composites based on MXenes can improve their efficiency through synergistic and additive effects. The growing demand for novel diagnostic techniques has led to the development of decentralized, user-friendly biosensors. MXenes, with their unique structure, distinct surface chemistry, excellent conductivity, and biocompatibility, are well-suited for developing cutting-edge electrochemical and biosensing devices.[205,206] Table 5 provides examples of MXene-based biosensors. Although MXene-based composites are promising biosensors in biomedicine, they generally have low brightness in the optical domain. MXenes have been coupled with fluorescent dyes or quantum dots to enhance their photoluminescence properties.[207] For example, rhodamine B was used to modify the surface of Ti_3C_2 MXene, which initially subdued the dye's fluorescence. However, in the presence of phospholipase D, the fluorescence was restored as the dye detached from the

Table 5 An overview of MXene-based biosensors

MXene nanocomposite	Probe	Sensing range	Limit of detection	Ref.
MXene–Au	Gram-negative/Gram-positive bacteria	3×10^5–3×10^8 CFU mL^{-1}	3×10^5 CFU mL^{-1}	212
MXene N-Ti_3C_2 quantum dot/Fe^{3+}	Glutathione	0.5–100 μm	0.17 μm	213
MXene–MoS_2	MicroRNA-21	100 fm–100 nm	26 fm	214
MXene-derived quantum dot@Au	Triple-negative breast cancer	5 fm–10 nm	1.7 fm	215
Prussian blue/Ti_3C_2 MXene	Exosomes	5×10^2–5×10^5 particles μL^{-1}	229 particles μL^{-1}	216
Ti_3C_2–MoS_2 MXene	Toxic gases	10–100 ppm	—	217
Ti_3C_2@ReS_2	Cancer-related miRNA-141	0.1 fm–1 nm	2.4 am	218
$Ti_3C_2T_x$ MXene–Au NPs@polyimide thin film	Carcinoembryonic antigen	0.1–100 ng mL^{-1}	0.001 ng mL^{-1}	200
MXene@Au NPs@methylene blue	Prostate-specific antigen	5 pg mL^{-1}–10 ng mL^{-1}	0.83 pg mL^{-1}	219

MXene nanosheets. Electronic stretchable and flexible sensors have introduced new possibilities for innovative applications.[208,209] These wearable sensors, which generate electrical signals in response to mechanical stimuli, have potential uses in humanoid robotics and intelligent medical diagnostics.[210] Due to their exceptional characteristics, MXenes are commonly used as nanofillers in polymer matrices to create flexible, elastic, and malleable electronics. For instance, $Ti_3C_2T_x$ nanosheets were incorporated into a glycerine/poly(dimethylsiloxane) film to develop a self-powered e-skin sensor. This e-skin sensor demonstrated adequate sensitivity, allowing it to track temperature changes between 15 and 25 °C.[211] MXenes can also be combined with DNA through robust chelation interactions to develop diagnostic composites. For example, an electrochemical biosensor for gliotoxin detection was created using Ti_3C_2 nanosheets modified with DNA nanostructures. The phosphoryl groups on the DNA nanostructures facilitated interactions with MXene nanosheets, speeding up electron flow between the electrochemical species and the electrode surface. The altered conformation of the DNA after attachment to target molecules resulted in a detectable electrochemical signal.

This biosensor showed a detection range of 5 pM to 10 nM and a limit of detection of 5 pM for gliotoxins. These biosensors could be further developed to detect additional mycotoxins (Fig. 13(a and b)).[220] Wearable electrochemical biosensors for sweat-based analysis face challenges such as inadequate durability, limited sensitivity, and instability of enzymes and biomaterials with repeated use. MXene-based composites have partially addressed these issues. For example, an MXene and Prussian blue composite was used to detect perspiration biomarkers, such as lactate and glucose. This electrochemical biosensor demonstrated a high sensitivity of 35.3 μA mm^{-1} cm^{-2} for lactate and 11.4 μA mm^{-1} cm^{-2} for glucose, with excellent repeatability (Fig. 13(c–e)).[221]

Another intriguing application of MXene-based biosensors is in oral disease diagnosis. A bio-aerogel with a 3D porous cellulose/$Ti_3C_2T_x$ MXene array was designed for diagnosing periodontal problems. The embedded MXene nanosheets provided flexibility and exceptional mechanical properties. The system could sense ammonia gas and pressure, making it suitable for oral health monitoring.

The sensor demonstrated biodegradability, biocompatibility, and low H_2O_2 concentrations during decomposition.[222] Aerogels from bacterial cellulose and $Ti_3C_2T_x$ MXene (BC/MXene) were flexible and rapidly degraded. This sensor platform was designed to detect local ammonia diffusion and occlusal force to prevent dental disorders. It showed high sensitivity to occlusal force and could differentiate between different contact points, demonstrating excellent sensitivity and selectivity to ammonia produced by dental decay. These MXene-based biosensors hold the potential for early detection of oral diseases (Fig. 14(a and b)).[222] The composite aerogel was produced by freeze-drying, which facilitated the arrangement of cellulose along the ice grain boundaries, creating a porous 3D structure. This preparation technique enhanced the mechanical strength of the sensing platform (Fig. 14(c)). The biosensor's pressure-sensitive responses were examined using triggers such as finger bending, sound, and pulse (Fig. 14(d–f)). These developments in MXene-based biosensors open new opportunities for designing and fabricating advanced functional materials for various diagnostic and therapeutic applications.

4.3.2. Stress and pressure sensors. Piezoresistive, piezoelectric, and capacitive are the three main types of pressure/strain sensors. The Greek word for pressure is the source of the prefix piezo. Applying pressure alters a material's electrical capacitance (capacitive pressure material), alters a piezoresistive material's resistivity, and generates charges in a piezoelectric material. The following formula for the capacitance of parallel-plate capacitors can be used to describe the operation of capacitive pressure sensors:

$$C = \frac{\varepsilon A}{d} \tag{7}$$

where ε = dielectric constant; A = surface area of electrodes; and d = distance between two electrodes. An applied force changes ε or d, changing C for a constant A. When a slight force is applied, ε or d should fluctuate perceptibly to get high sensitivity. The dielectric material must have a low compressive modulus to meet this criterion. Aerogels and elastomeric materials are two excellent examples of materials having a low compressive modulus. When a dielectric layer of these materials is subjected to a small force, it deforms significantly. In these scenarios, an MXene can effectively increase the dielectric constant and decrease the compression modulus of a polymeric dielectric material, such as poly(vinylidene fluoride-trifluoroethylene) (PVDF-TrFE), to improve its sensitivity. A potential method to create wearable, mechanically robust

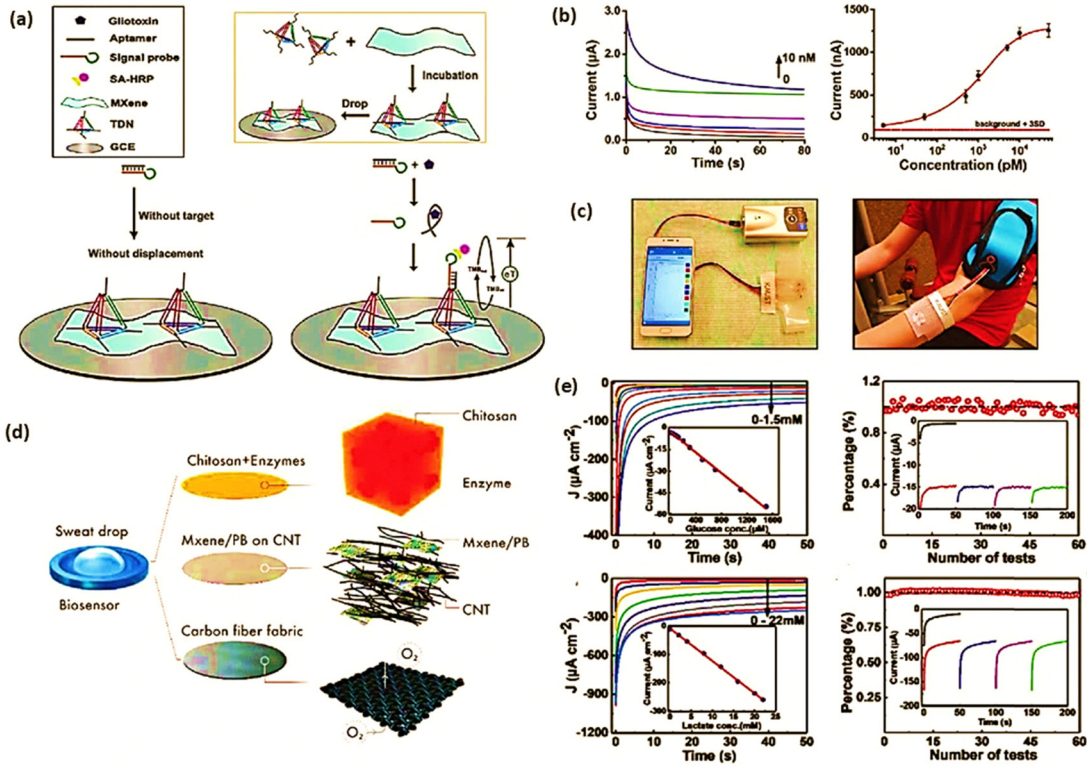

Fig. 13 (a) Schematic diagram of a typical label-free electrochemical gliotoxin biosensor based on the MXene-based nanocomposite including the tetrahedral DNA nanostructure (TDN) and horseradish peroxidase (HRP); (b) amperometric response curves (concentration range: 0–10 000 pm) and the examined logarithmic plot (amperometric current *vs.* gliotoxin concentration)[220] are two examples of the electrochemical properties utilised for the diagnosis of gliotoxins (Copyright (2019) Elsevier); (c) the portable electrochemical analyzer on the body attached to the wearable real-time sweat monitoring patch, which provides electricity for monitoring glucose, lactate, and pH levels. It also connects wirelessly *via* Bluetooth to commercial mobile phones; (d) schematic diagram of oxygen-rich sensing electrodes in wearable electrochemical biosensors, featuring conducting super hydrophobic carbon fiber, carbon nanotubes, $Ti_3C_2T_x$, and Prussian blue. The optical picture of the sensing patch system linked to a portable device; (e) chronoamperometric response of the glucose/lactate sensor at different glucose concentrations (0–1.5 × 10^{-3} M, pH = 6 for glucose and 0–22 × 10^{-3} M, pH = 6 for lactate). The sensor calibration curve and typical responses over time are displayed in the inset. The chronoamperometric response was observed at the 10th, 20th, 30th, and 40th tests for glucose/lactate[221] (Copyright (2019) John Wiley and Sons).

pressure sensors is MXene/PVDF-TrFE sandwiched between two flexible polymeric electrodes. This can be used to create capacitive MXene/polymer pressure sensors.[225] Fig. 15 shows the fabrication of such MXene/polymer sensors. A change in resistivity happens in MXene-based piezoresistive strain sensors in response to pressure or force. In most cases, the resistivity change is stated as $\Delta R/R_0$, where R_0 = resistivity of the sensor material with no stretch and ΔR = difference in resistivity before and after the strain. A strain sensor's gauge factor (GF) indicates the sensitivity.

$$\mathrm{GF} = \frac{\Delta R/R_0}{\Delta L/L_0} \tag{8}$$

where ΔL = absolute change in length and L_0 = original length of the sensor before strain. The resistivity changes more when a strain occurs when the GF is higher.

Lately, strain sensors with MXene and poly(dimethylsiloxane) with a GF of 3.6 have been effectively constructed.[226] In the strain range of 0–10%, MXene/elastomer sensors with a GF 43–107 were also identified.[227] The significance of a pressure sensor's sensitivity is provided by

$$s = \frac{\Delta I/I_0}{\Delta p} \tag{9}$$

where ΔI = changes in the electrical current; ΔP = pressure reading before and after applying pressure; and I_0 = electrical current when no pressure is exerted.[228] Most MXene/polymer sensors generate a conductive network of MXene flakes when the MXene concentration reaches a point known as the percolation concentration. The MXene flakes of the network move closer to one another when under pressure and detach from one another when under strain. The gaps between MXene flakes increase with the complexity of electrical charges moving through the MXene network. Indeed, isolated or weakly linked flakes produce extra resistance for charge transfer. The basis for the operation of strain and pressure sensors containing electroconductive nanoparticles, such as MXene, is the relationship between the magnitude of electrical charge transport and the applied force.[229]

4.3.3. Humidity and moisture sensors. Because they are hydrophilic, MXene nanosheets are useful for humidity sensing. That implies humidity monitoring and detection can be

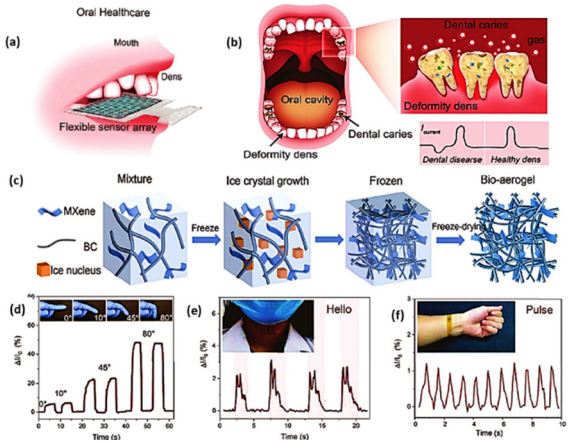

Fig. 14 Flexible sensing platform based on the BC/MXene bio-aerogel. (a) and (b) Illustration and principle of the flexible sensor based on bio-aerogel and BC/MXene; (c) schematic diagram of BC/MXene bio-aerogel synthesis[223] (Copyright (2023) Frontiers); (d) bending and straightening the index finger induces the BC/MXene bio-aerogel flexible sensor to adapt to a pressure-sensitive approach. The reaction exhibits varying intensities and frequent shifts in response to varying degrees of bending; (e) and (f) when attached to the throat, sound detection is achieved by tracking the vibration of the vocal cords during speaking; when the flexible sensor is connected to the wrist, human health is monitored through the pulse signal of the BC/MXene-based BC sensor. In summary, it has been determined that the average human pulse frequency is 70 times per minute[224] (Copyright (2022) John Wiley and Sons).

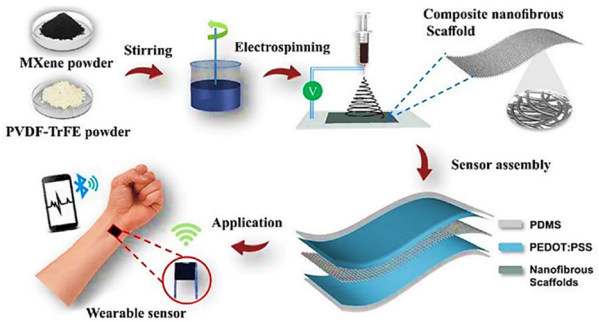

Fig. 15 Developing a sensitive pressure sensor through poly(3,4-ethylenedioxythiophene) polystyrenesulfonate/polydimethylsiloxane electrodes and PVDF-TrFE dielectric material[225] (Copyright (2019) American Chemical Society).

done with MXene-based sensors. It is understood that water seeping into the MXene network causes an increase in the electrical conductivity of an MXene-based sensor. On the other hand, An *et al.* observed that greater interlayer spacing and tunnelling resistance between the sheets result from the intercalation of water molecules between MXene flakes.[230] They also explained that this process is reversible, and the resistivity decreases due to the water molecules' deintercalation, which shortens the interlayer distance. The humidity sensor was sufficiently sensitive to identify and measure a person's intake and exhale rate when walking and jogging (Fig. 16).[230]

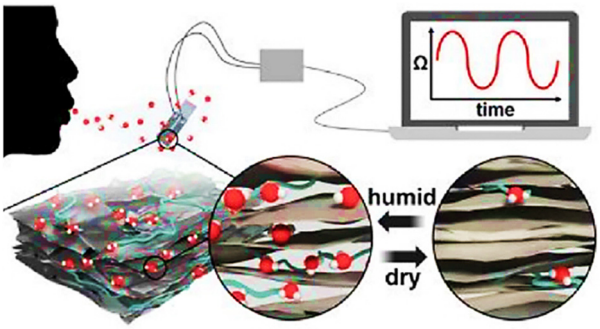

Fig. 16 The MXene-based humidity sensor reacts by permitting water to intercalate and decallate between its layers[230] (Copyright (2019) American Chemical Society).

The rate of inhalation/exhalation is higher during running than during walking, and this difference can be detected by the humidity-detecting sensor due to the higher rate of water intercalation between MXene layers during running. Regardless of the mechanism, it is crucial to understand that the conductivity of MXenes changes when water molecules penetrate between their flakes, and due to this property, MXenes are desirable for use in moisture and humidity detecting sensors.

4.3.4. Comprehension of human motion. Wearable sensors are elastic nanocomposite sensors composed of elastomeric polymers. It has been mentioned that MXene/polymer sensors can detect even minute movements in the human body with sufficient accuracy.[227] The facial muscles of an individual stretch and contract when they change their expression or enunciate words differently.[227] For instance, a person's throat muscles contract or relax differently as they speak. The motions of the throat muscles during the utterance of a particular phrase create a distinct pattern that these sensors can detect when affixed to the front of the neck or the skin of the face (Fig. 17(a)). Consequently, voice detection can be done with

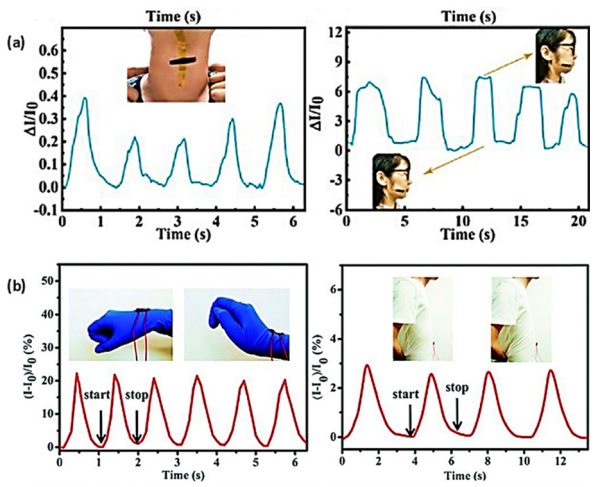

Fig. 17 (a) MXene-based skin-mountable sensors for speech recognition[228] (Copyright (2020) Wiley) and (b) to detect minute motions in the body by attaching MXene-based sensors to different body parts[232] (Copyright (2020) Royal Society of Chemistry).

MXene-based sensors.[225] Voice signals that have been analyzed can subsequently be translated into commands for driving a car. This indicates potential in robotics, artificial intelligence, and autonomous vehicles.[227] Several reusable MXene/polymer nanocomposite sensors are available to detect movements of the hand, stomach, eyebrow, finger, and other body parts (Fig. 17(b)).[229,231] Motion sensors based on MXenes can detect and measure motion by comparing it to $\Delta R/R_0$. Authenticating signatures is an intriguing use case for MXene-based motion sensors. When signing a document, each person applies pressure and takes a different time. It is possible to create a motion sensor that resembles a thin sheet and insert it beneath the document that needs to be signed.

Subsequently, the sensor produces an exclusive electrical signal, which is analyzed by artificial intelligence equipped with a signature database to verify the legitimacy of the signature. Therefore, there are numerous security applications for MXene-based motion sensors.[229] A wearable motion sensor can also be used as a pulse meter to detect heartbeat rate. The heart's performance can then be assessed by analyzing the recorded signal.[233]

4.3.5. Gas sensors. Distinct gases have varying affinities to the MXene surface. Consequently, their possibilities of adsorption on the MXene surface are different. Electrons from gas molecules migrate to the MXene surface when molecules of a gas with excellent affinity for the surface are adsorbed. Since the electrical conductivity of MXenes depends on their electronic configuration and surface functional groups, this changes the conductivity of the MXene. Significant changes in MXene conductivity are not brought about by gases that contact poorly with its surface or that do not exhibit affinities towards it.[234] An MXene-based gas sensor's reaction is explained as follows:

$$R = 100\frac{|R_g - R_a|}{R_a} \quad (10)$$

where R_g = sensor resistance in gas and R_a = sensor resistance in air. Furthermore, $\Delta I/I_0$ can indicate the gas sensitivity, where ΔI is the electrical current change upon gas contact and I_0 is the electrical current before gas adsorption. A more accessible MXene surface makes gas detection easier because gas detection depends on the interaction of a gas molecule with the surface of an MXene. Therefore, a single-layer MXene with a larger surface area is preferable to a multilayer or stacked MXene in sensor manufacturing. By employing *in situ* polymerization, Zhao *et al.* developed polyaniline (PANI) particles on the surface of Ti_3C_2 to stop MXene flakes from stacking and preserve the surface for the adsorption of gaseous molecules.[235] This allowed for greater gas diffusion paths, an open structure between the MXene layers, and reasonable access to the MXene sensing layer.[235] Due to this change, the MXene/PANI sensor demonstrated a 2.3-fold increase in ethanol sensitivity compared to the original MXene. It also provided a significant degree of flexibility to the MXene-based sensor (Fig. 18).[235] Wu *et al.* used a pristine MXene gas sensor and showed that the sensor can distinguish between NH_3 and ethanol at concentrations as low as 10 ppm.[234] The sensor responded to a 25 ppm

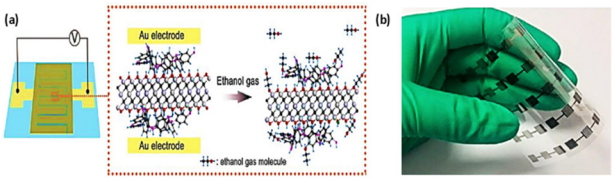

Fig. 18 (a) MXene-based gas sensors for ethanol detection; (b) flexibility of the sensing layer of the PANI-modified MXene-based gas sensor[235] (Copyright (2019) Wiley).

NH_3 mixture with a response time of 45 s and recovered in 94 s. The pristine MXene sensor's NH_3 selectivity was four times higher than its ethanol selectivity, indicating that it is appropriate for ammonia detection. However, the MXene/PANI gas sensor effectively detected ethanol more than ammonia.[235] The strength of a gas molecule's contact with a sensor surface is the source of these variations.[235] Including PANI in the MXene/PANI sensor enhanced the possibility that the functional groups would interact with ethanol molecules and facilitate electron transport from ethanol to the MXene surface compared to a pure MXene sensor.[234] Consequently, the selectivity of MXene-based sensors for particular gas detection is improved by tailoring the surface chemistry of MXenes through polymer grafting. Various MXenes beyond Ti_3C_2 can also be utilized to develop and produce sensors. For instance, Ti_2C MXene for gas sensor applications was studied practically and conceptually.[236] Simulation investigations confirm that when the surface of single-layer Ti_2C is enriched with oxygen functional groups, it exhibits greater sensitivity for NH_3 than for CO_2, O_2, H_2, and CH_4. Additionally, outstanding NH_3 detection was demonstrated *via* artificially flexible Ti_2C/polyimide sensors. A sensor for detecting nonpolar gases was created by combining V_2C, an MXene, with polyimide. It was possible to develop temperature- and CO_2-sensitive sensors by grafting poly(2-(dimethylamino)ethyl methacrylate) onto the V_2C surface.[236]

Here, in Table 6, we have presented a quick overview of various MXene-based sensors and their application.

4.4. Imaging

Imaging technology is critical for accurate tumour staging and localization, as well as for directing cancer treatment and identifying post-treatment recurrences. It is an essential tool for early cancer diagnosis. MXene nanosheets have excellent physicochemical properties, making them highly promising for diagnostic imaging. They can be used with various imaging techniques, including magnetic resonance imaging (MRI), photoacoustic imaging, CT, and fluorescence imaging.

Novel MXene-based reagent-based imaging approaches can help overcome some of the frequent issues and limitations with existing reagents. For instance, 2D MXene-based reagents have quantum size effects for photoluminescence (PL) cell imaging, which can improve elemental contrast for X-ray CT imaging and intrinsic photothermal properties for PA imaging. This is in contrast to traditional imaging reagents.

Table 6 An overview of MXene-based sensors

MXene based composites	Application	Ref.
Ti_3C_2–rGO	Pressure sensor	237
Ti_3C_2–chitosan	Biosensor	238
Ti_3C_2–polyurethane	Strain sensing fabric	239
Ti_3C_2-epoxidized natural rubber	Self-healable intelligent sensor	227
Ti_3C_2-ink	Strain sensor	240
Ti_3C_2-poly(vinyl alcohol)	Wearable electronic sensors	229
Ti_3C_2-poly(dimethylsiloxane)	Skin conformal sensors	233
Ti_3C_2-Ag nanoparticles	Biosensor for glucose detection	241
Ti_3C_2-TiO_2	H_2O_2 sensor	242
Ti_3C_2-modified sodium alginate-polyacrylamide	Human motion sensor and biomonitoring sensor	232
Ti_3C_2-poly(diallyldimethyl ammonium chloride)	Humidity sensor	230

4.4.1. Luminous imaging method. In aqueous solutions, conventional MXene-based materials show extremely low luminescence properties; thus, no photoluminescence response is visible. Researchers have employed several techniques to improve MXene's fluorescence qualities and increase the range of potential biomedical uses. The fluorescence characteristics of MXene materials can be enhanced by two primary methods. One technique is to give MXenes luminous characteristics by affixing a fluorescent species on their surfaces. Electrostatic adsorption is used to load the cationic fluorescent medicine DOX onto an MXene containing the p-terminus aluminum oxide anion (Fig. 19(a)) to achieve coupling.[243] This technology can be used for biological imaging and anticancer therapy because of the auto-fluorescence effect of anticancer medication DOX. The second approach is developing MXene quantum dots (MQDs) with luminescence characteristics. Like graphene quantum dots (QDs), molybdenum disulfide QDs, and boron nitride QDs, MQDs have luminescence characteristics dependent on excitation, making them suitable for practical fluorescence imaging.[244–249] Hydrothermal techniques are one of the many ways MXene flakes can be broken down into quantum dots with minimal diameters and outstanding photoluminescence (PL) capabilities.[250–252] The advantages of using quantum dots of inorganic two-dimensional nanomaterials, such as MQDs, over conventional organic fluorescein are as follows: low cytotoxicity, high dispersibility for bioimaging, high chemical stability and photostability, high quantum yield of photoluminescence, and tunable wavelength that can be adjusted by varying the size, shape, or functionality of the prepared quantum dots. The size effect and surface defects are the two mechanisms of luminescence in 2D materials that are still under debate, even though substantial photoluminescence effects may be seen in materials like graphene and MXene quantum dots.[253,254] With the simple hydrothermal technique, Xue *et al.* produced monolayered $Ti_3C_2T_x$ QDs at temperatures of 100 °C (MQD-100), 120 °C (MQD-120), and 150 °C (MQD-150). They then showed that these MQDs have excitation-dependent luminous features.[255] They ultimately concluded that the MQDs showed excitation-related PL behaviour based on the UV–vis spectra and PL excitation (PLE) spectra that were recorded with the greatest luminescence (Fig. 19(b)). It was discovered that MQDs are sufficiently stable to be employed in circumstances with a range of pH values by examining the variation of PL intensities of MQDs at different pH values. MQDs have a great deal of potential as biocompatible multicolour cell imaging reagents. Initial MQD-100 and MQD-120 cell imaging experiments were conducted by labelling RAW264.7 cells (Fig. 19(c)).[255] Nb2CT$_x$ QDs were synthesized in tetrapropylammonium hydroxide (TPAOH) solution through ultrasonic-assisted physicochemical exfoliation.[256] In contrast to conventional nanofluorescence, the synthesized Nb_2CT_x QDs demonstrated remarkable chemical stability and biocompatibility, particularly noteworthy enzyme-responsive biodegradability and exceptional anti-photobleaching capability (Fig. 20(a)).

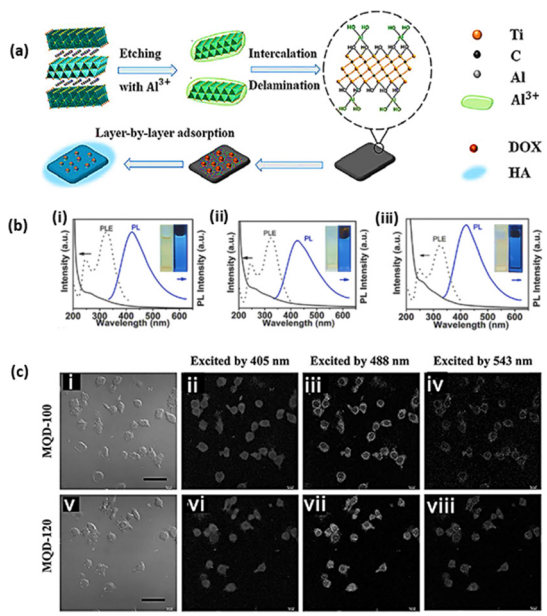

Fig. 19 (a) Schematic illustration of the development of Ti_3C_2-DOX[243] (Copyright (2017) American Chemical Society); (b) UV-vis (solid line), PLE (dashed line), and PL (solid line, Ex = 320 nm) spectra of (i) MQD-100, (ii) MQD-120 and (iii) MQD-150 solutions under a 365 nm UV lamp and visible light[255] (Copyright (2017) John Wiley and Sons); (c) (i and v) bright-field confocal images (at 405, 488, and 543 nm) of RAW264.7 cells (ii–iv) with MQD-100 and (vi–viii) with MQD-120[255] (Copyright (2017) John Wiley and Sons).

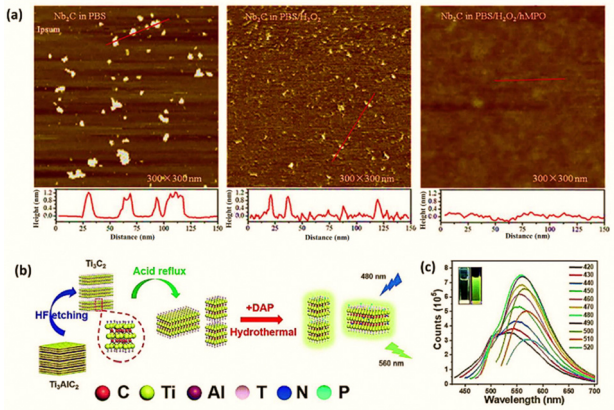

Fig. 20 (a) The related height distributions and AFM pictures of Nb_2CT_x quantum dots with various biodegradation treatments over 24 hours duration time[256] (Copyright (2020) Elsevier); (b) diagrammatic representation of synthesis of N,P-MQDs[257] (Copyright (2019) Royal Society of Chemistry); (c) emission spectra of fluorescence of N-P-MQDs, which developed at 120 °C with various excitation wavelengths. In the inset, the image was taken under UV light (365 nm)[257] (Copyright (2019) Royal Society of Chemistry).

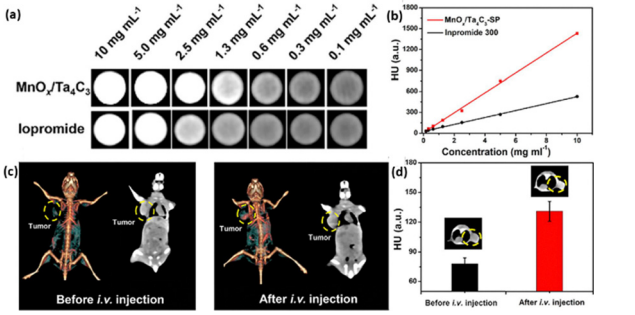

Fig. 21 CT scans *in vitro* (a) with HU principles; (b) both the iopromide solution and the $MnO_x/Ta_4C_3T_x$-SP composite nanosheet solution at different concentrations (concentration of Ta, I); (c) mice were injected intravenously with $MnO_x/Ta_4C_3T_x$-SP composite nanosheets (20 mg kg^{-1}, 100 μL) for two hours, as demonstrated in the *in vivo* 3D reconstructed CT (left) and contrast (right) images; (d) CT comparison of *in vivo* tumour tissues before and after $MnO_x/Ta_4C_3T_x$-SP composite nanosheets were administered intravenously[180] (Copyright (2017) American Chemical Society).

modifications can be made to improve their properties further. To get greater quantum yields (QY), better stability, and more surface active centres, doping with elements like N, Cu, and P, among others, is an essential way, which can drastically alter the electrical characteristics and structure of quantum dots.[258–260] The photoluminescence quantum yield (PLQY) was significantly raised to 20.1%, as Guan *et al.* synthesized nitrogen–phosphorus functionalized $Ti_3C_2T_x$ MXene-based quantum dots (N,P-MQDs) with a hydrothermal approach (Fig. 20(b)).[257] At 480 nm excitation, the newly created photoluminescent quantum dots showed intense green fluorescence for the first time (Fig. 20(c)). As an additional illustration, DMF was used as the solvent medium and nitrogen-doping agent to synthesize a class of N-$Ti_3C_2T_x$ quantum dots utilizing two-dimensional $Ti_3C_2T_x$ as the raw material.[261] After being further added with DAP, the resulting N-$Ti_3C_2T_x$ quantum dots demonstrated good dispersion stability and formed a composite nanoprobe (N-$Ti_3C_2T_x$ quantum dots@DAP nanoprobe). Wang *et al*. used a solvothermal method to simultaneously cut and stack cleaved layers in an aqueous TMAOH solution to develop extremely tiny MXenes with monolayer thickness, lateral dimensions of 2–8 nm, and excellent and controllable fluorescence.[262] Furthermore, Zhou *et al*. developed a method for the synthesis of graphene quantum dots (GQDs) from layered $Ti_3C_2T_x$ by solvent heat treatment of $Ti_3C_2T_x$ in dimethylformamide (DMF) for bioimaging.[263] The development of MQD modification methodologies has led to ongoing improvements in MQD performance for cellular imaging.

4.4.2. Computed tomography (CT) imaging method. Due to deep tissue penetration, non-invasiveness, and excellent spatial resolution, CT imaging is one of the most popular and valuable diagnostic imaging techniques. The primary basis for CT imaging is the variation in tissue absorption of radiation; successive sections of a body component are scanned to create 3D images.[264,265] Because of their propensity to attenuate X-rays, nanomaterials containing high atomic number elements, including bismuth, cesium, tantalum, and tungsten, are frequently regarded as possible CT imaging materials.[265] As iodine-containing compounds have a limited blood circulation duration and are very toxic, they are not recommended for patients who need repetitive CT scans or who are at high risk.[266,267] These agents are also the most widely used clinically approved CT contrast agents. Accordingly, a common path in the evolution of CT is seeking CT imaging agents with high atomic number elements and improved biocompatibility. Many biomedical researchers are interested in two-dimensional materials like MXenes because of their distinct structural and physicochemical features. The element tantalum (Ta) has a high atomic number (Z = 73) and a high X-ray attenuation coefficient. Tantalum's X-ray attenuation coefficient at 100 eV is 4.3 cm^2 kg^{-1}, while for gold it is 5.16 cm^2 kg^{-1}.[268] So, $Ta_4C_3T_x$, a Ta-based MXene, is considered to be the best agent for CT imaging.[180,269,270] The CT scans of $MnO_x/Ta_4C_3T_x$-SP composite nanosheets exhibited an excellent linear positive connection between the brightness and accompanying improved Hounsfield unit (HU) values and the concentration of Ta. This correlation was enhanced with increasing Ta concentration (Fig. 21(a and b)). *In vitro* CT images of $MnO_x/Ta_4C_3T_x$-SP composite nanosheets demonstrated a stronger signal and higher contrast at the same elemental concentration compared with the CT imaging impact of iodine-based iopromide, which is currently employed in clinical practice (Fig. 21(c and d)).[180]

4.4.3. Magnetic resonance imaging (MRI) method. Compared to the CT method, which utilizes hazardous radiation, in terms of imaging capabilities, MRI is another non-invasive clinical imaging technology.[271] However, MRI technology can immediately provide native 3D cross-sectional images without reconstruction, better depict the structure of human soft tissues, and does not harm the body with ionizing radiation.[272] Gadolinium(III) complexes are commonly utilized as MRI

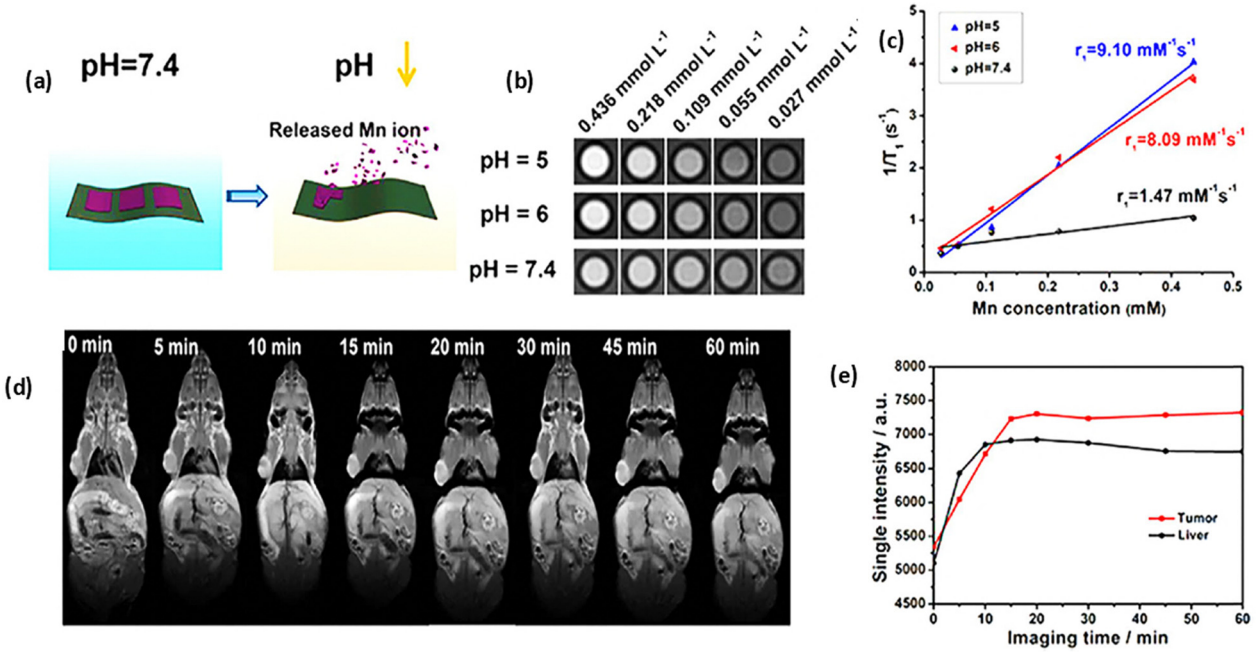

Fig. 22 Comparison of CT scans of *in vivo* tumour tissues before and after intravenous injection of $MnO_x/Ta_4C_3T_x$-SP composite nanosheets: (a) schematic diagram of dissolution of MnO_x in mildly acidic conditions; (b) $MnO_x/Ti_3C_2T_x$-SP nanosheets utilizing *in vitro* T1-weighted magnetic resonance imaging after 3-hour immersion in a series of solutions with varying pH levels; (c) $MnO_x/Ti_3C_2T_x$-SP nanosheets immersed for 3 hours in buffer solutions with varying pH values; 1/T1 *vs.* Mn concentration. Imaging with T1 weighted input; (d) identifying the same MRI signal strength; (e) mice at various intervals after the intravenous injection of $MnO_x/Ti_3C_2T_x$-SP composite nanosheets[275] (Copyright (2017) American Chemical Society).

contrast agents. However, in recent years, there has been increasing concern about their toxicity to the kidneys. Persons with renal insufficiency who use gadolinium(III)-based MRI contrast agents face the risk of developing deadly nephrogenic systemic fibrosis (Nsf). At the same time, persons with normal renal function have also been shown to have metallic gadolinium deposits in their brains.[273,274] Thus, the scientific world has focused much work on developing an MRI contrast agent with high biosafety and low toxicity to enhance the quality and specificity of MRI. Manganese (Mn)-based paramagnetic agents are a unique class of biocompatible materials with tremendous potential for therapeutic uses in magnetic resonance imaging.[275,276] For example, the ''redox reaction-induced growth'' (RR-IG) method effectively immobilized paramagnetic MnO_x on the surfaces of $Ti_3C_2T_x$ nanosheets. Moreover, additional surface modification with soy phospholipids (SP) significantly increased the stability of the $MnO_x/Ti_3C_2T_x$ composite nanosheets ($MnO_x/Ti_3C_2T_x$-SP).[275] The developed $MnO_x/Ti_3C_2T_x$-SP composite nanosheets can be used for tumour MRI since the surface-anchored paramagnetic MnO_x component exhibits a unique pH-responsive T1-weighted MRI capacity. In the slightly acidic microenvironment of the tumour, the Mn–O bond is readily broken to release Mn^{2+} ions (Fig. 22(a)), which maximizes the possibility of interaction between paramagnetic Mn centres and water molecules, thereby enhancing the T1-weighted MRI performance.[277] This conclusion was reinforced by *in vivo* studies in mice, where the MRI signal was significantly enhanced in tumours (Fig. 22(d and e)),[275] as well as by *in vitro* experiments showing the enhancement of the MRI signal (Fig. 22(b and c)) and the dissociative release of Mn^{2+} under acidic conditions (Fig. 22(a)). To assess the potential of $MnO_x/Ti_3C_2T_x$-SP composite nanosheets, T1-weighted imaging was conducted at different intervals after the intravenous injection of a sufficient dose of $MnO_x/Ti_3C_2T_x$-SP nanosheets (dose: 2 mg mL^{-1}, 100 μL) into mice. A notable brightening effect of MRI signals in tumours was seen in the T1-weighted imaging data, and the signals progressively improved with longer imaging duration (Fig. 22(d and e)).[275] Liu *et al.* also tried to prepare agents for multimodal imaging. They were able to immobilize superparamagnetic iron oxide nanoparticles (IONPs) on the surface of a 2D MXene, $Ta_4C_3T_x$, by producing $Ta_4C_3T_x$-IONP through *in situ* growth, which gave the TaCT/superparamagnetic iron oxide (IONP) nanocomposite the ability to perform contrast-enhanced T2-weighted MR imaging (Fig. 23(a)).[270] Zong *et al.* developed an alternative method to generate $GdW_{10}@Ti_3C_2$ composites. They accomplished it by depositing GdW_{10} on the surfaces of Ti_3C_2 nanoflakes, which can be utilized as contrast agents for improved CT and MR imaging (Fig. 23(b)).[278]

4.4.4. Photoacoustic imaging (PAI) method. PAI, a non-invasive and non-ionizing biomedical imaging technology, has recently gained interest. When a non-ionizing pulsed laser is directed at biological tissues, the light-absorbing domains in the tissues transform the energy into ultrasonic waves, also known as photoacoustic signals. The photoacoustic signal is converted into an image of the tissue distribution of light absorption by the ultrasonic transducer being considered. This signal contains information on the properties of tissue light

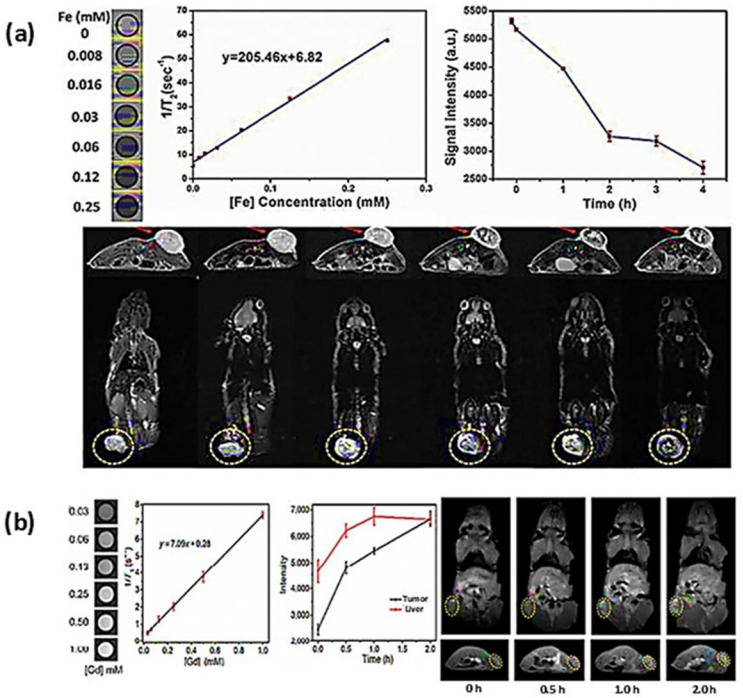

Fig. 23 (a) T2-weighted MRI transverse and coronal sections taken before and after intravenous injection of $Ta_4C_3T_x$-IONP-SPS in a 4T1 tumour-bearing animal at various periods. The longer the observation period, the more visible the regions of hypointense signal T2 pictures were at the tumour site[270] (Copyright (2021) Ivyspring International Publisher); (b) MRI signal intensity of a tumour *in vivo* and the liver of 4T1 tumour-bearing mice after intravenous injection[278] (Copyright (2018) Springer Nature).

absorption. PAI contrast agents make deeper tissue imaging possible, primarily avoiding light scattering effects and providing a higher spatial distribution rate for living objects than pure optical tissue imaging.[279,280] Therefore, an effective PAI contrast agent should have excellent photothermal conversion ability to create a signal that significantly contrasts with the PA signal formed by the surrounding tissue. The LSPR-effecting MXene nanosheets are thought to be very appealing PAI contrast agents. Various MXenes with excellent photothermal conversion properties, including $Ti_3C_2T_x$, Nb_2CT_x, and $Ta_4C_3T_x$, have been stated.[180,269,275,281] Because of its excellent photothermal conversion efficiency and biocompatibility, $Ta_4C_3T_x$-SP shows potential application in PA contrast agents. A photothermal converter's photothermal performance is primarily determined by two parameters: the extinction coefficient (ε) and the photothermal conversion efficiency (η). The photothermal conversion efficiency indicates the photothermal converter's effectiveness, whereas the extinction coefficient indicates the amount of light that may be absorbed. Excellent near-infrared photothermal properties were exhibited by 2D ultrathin $Ta_4C_3T_x$ nanosheets prepared by the liquid-phase exfoliation method, which combines HF etching and probe ultrasonication. These nanosheets had an extinction coefficient of 4.06 lg^{-1} cm^{-1} at 808 nm, a photothermal conversion efficiency of 44.7%, and excellent photothermal stability.[269] MQDs, which exhibit a high and broad near-infrared absorption band, have potential uses in fluorescence imaging and as excellent imaging agents for tumour photo-immunization. A fluorine-free approach was used to create a MQD. The quantum dots showed stronger and broader absorption capabilities in the near-infrared region with an extinction coefficient as high as 52.8 lg^{-1} cm^{-1} at 808 nm and a photothermal conversion efficiency as high as 52.2% because of the modification of a large number of aluminum oxygen anions on their surface. Zhang *et al.* created MXene quantum dots, which allowed for simultaneous PTT effects and photoacoustic (PA) imaging of tumours.[118] Overall, MXene-based PAI is a potential imaging tool that may overcome the penetration constraints of conventional optical imaging techniques to obtain deeper tissue imaging because of its low tissue attenuation coefficient.

4.5. Drug delivery

MXenes have a unique structure that makes them helpful in building gene and drug delivery systems that will increase targeted drug delivery, decrease drug toxicity, and enhance the pharmaco-kinetics of therapeutic molecules. Nanoscale-sized MXene materials make it easier to administer intravenous therapy to the sick region and efficiently accumulate there during treatment. Additionally, the substantial specific surface area of MXenes results from their two-dimensional planar topology, which offers many anchoring sites for medicinal molecules on the surface of the laminar structure. At the moment, cancer is a serious illness that poses a risk to human health and claims many lives annually on a global scale. By improving the cellular absorption of the payload and regulating medication release, materials based on MXenes have the

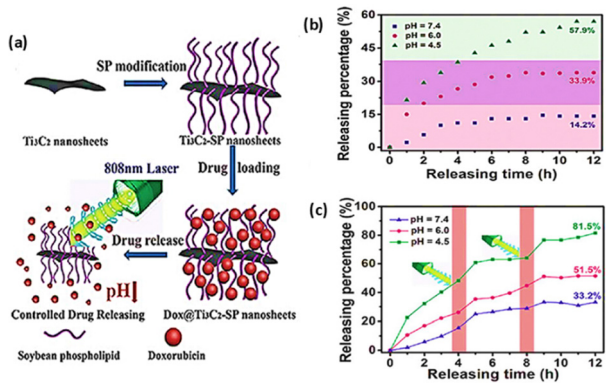

Fig. 24 (a) Diagrammatic illustration of pH-responsive and laser-induced drug release of $Ti_3C_2T_x$-SP nanosheets loaded with DOX; (b) the Dox release patterns of Dox@$Ti_3C_2T_x$-SP nanosheets in buffer solutions of various pH; (c) the Dox release profiles at various pH levels attributed to 808 nm laser irradiation[285] (Copyright (2018) John Wiley and Sons).

potential to target cancer cells efficiently.[192,282–284] Previously, research indicates that MXenes are helpful anticancer agents. Through layer-by-layer surface modification of doxorubicin (DOX) and hyaluronic acid (HA), Chen *et al.* developed a multifunctional Ti_3C_2-based nanoplatform ($Ti_3C_2T_x$-DOX). This was feasible due to the positive charge of DOX on the surface of $Ti_3C_2T_x$ and the negative charge of tumour-targeted HA.[243] The photothermal performance and light-harvesting capabilities of $Ti_3C_2T_x$, produced using tetrapropylammonium hydroxide (TPAOH) intercalation, were further improved upon by adding hydroxyl groups. By overexpressing $CD44^+$ on cancer cell membranes, HA coating of the outer layer of the nanosheets enhanced the system's biocompatibility and allowed for active targeting of tumour cells. This Ti3C2T_x-DOX demonstrated a drug loading capacity of up to 84.2%. Additionally, studies conducted *in vitro* and *in vivo* demonstrated that the system could display high biocompatibility, adequate pH sensitivity, and drug-releasing behaviour caused by NIR lasers.[243]

Additionally, for highly effective tumour eradication, cancer-fighting medicines (doxorubicin, DOX) can be loaded onto the surfaces of Ti_3C_2 nanosheets modified by SP that have a large specific surface area ($Ti_3C_2T_x$-SP) (Fig. 24(a)). In addition to having a high drug-loading capacity (up to 211.8%), pH responsiveness (Fig. 24(b)), and NIR laser-triggered drug release (Fig. 24(c)), $Ti_3C_2T_x$-SP is a unique nano drug-delivery system.[285] A possible drawback of the use of MXenes as drug-delivery carriers is that they cannot provide a contained space for significant drug loading. Based on simple sol–gel chemistry, surface nanopore engineering of $Ti_3C_2T_x$ has been carried out in a recent study to improve drug loading/release capabilities and expand the biomedical uses of MXenes.[182] With cetyltrimethylammonium chloride (CTAC) as a mesoporous guide and tetraethylorthosilicate (TEOS) as a precursor ($Ti_3C_2T_x$@ mMSNs), a thin layer of mesoporous silica shell was successfully applied to the surface of $Ti_3C_2T_x$ under alkaline synthesis conditions. This improved the interfacial properties of $Ti_3C_2T_x$ and combined the benefits of both materials as drug carriers, including a space-confined mesoporous structure, enhanced hydrophilicity, suitable surface chemistry, and dispersibility. Arginine-glycine-aspartic acid (RGD) was covalently linked to $Ti_3C_2T_x$@mMSNs modified with polyethylene glycol (PEG) to provide an active targeting response to the tumour location. With a consistent pore size of 3.1 nm, a high pore volume of 0.96 $cm^3\ g^{-1}$, and a specific surface area of 772 $m^2\ g^{-1}$, the synthesized $Ti_3C_2T_x$@mMSNs exhibit a good mesoporous structure. Evaluations conducted both *in vivo* and *in vitro* have demonstrated the high biocompatibility and active-targeting capability of the novel MXene-based composite nano-systems created by this method.

Combined with conventional chemotherapy and photothermal hyperthermia, these systems can completely eradicate tumours without a significant recurrence.[182] Additionally, MBEne, a promising post-MXene material, has just been created as a versatile platform for nano-delivery. With the help of a microwave-associated chemical etching technique, He *et al.* successfully synthesized a 2D zirconium boride nanosheet (ZBN) with good dispersion through hyaluronic acid (HA) surface modification by borate esterification. ZBN has excellent NIR-photothermal properties, with a high photothermal conversion efficiency of 76.8% in the NIR-II aperture (1060 nm). By loading doxorubicin (DOX) and NO prodrug (Gal-NO) on the surface of ZBN-HA *via* borate esterification, high drug loading (ZBN-HA/DOX and ZBN-HA/NO) was accomplished. Photo-controlled intratumoral retention and drug release were achieved using ZBN-HA/DOX and ZBN-HA/NO photo-pyrolysis, facilitating HA deconjugation and ZBN aggregation.[286] Ultimately, because of their 2-dimensional planar architecture and nanoscale, MXenes are excellent drug carriers.

4.6. Wound treatment

The skin, which covers most of our body's exterior, shields our interior organs from harm, infection, heat, and light. Consequently, any flaws in the skin have the potential to cause a variety of illnesses, including wound infections, which can have an impact on the health of individuals.[287,288] Skin wound recovery requires multistep processes involving coordinating multiple cell types found in the epidermis, dermis, and hypodermis layers. The human body's normal reaction to an injury is skin wound healing, consisting of four highly integrated and overlapping phases: hemostasis, inflammation, proliferation, and tissue remodelling. For wound healing to succeed, these steps must be followed precisely.[289] An ideal dressing for wound healing should be antibacterial, maintain a steady temperature, and inhibit the migration and multiplication of cells.[290–292] Hydrogel-based dressings have garnered much interest in wound healing. Among their many benefits are their remarkable adhesiveness to native tissues, ability to imitate the biological microenvironment, ability to maintain a moist-like environment surrounding the wound site, and high oxygen permeability, which promotes optimal tissue regeneration. Notwithstanding these advantages, hydrogels behave erratically when healing wounds. To solve this issue, they are paired with additional treatment approaches for desired behaviour.[293]

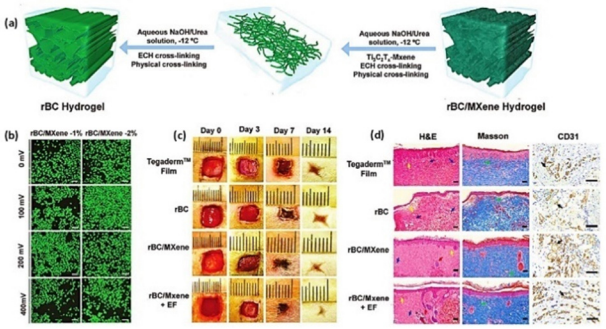

Fig. 25 (a) Hydrogels based on cellulose (rBC) and their synthesis strategy; (b) confocal microscopy of staining for life and death. Scale bar: 100 μm; (c) The healing process of the wounds in the various treatment groups on days 0, 3, 7, and 14. Scale bar: 500 μm; (d) on day 14, $CD31^+$ microvessel immunohistochemistry staining, Masson's trichrome staining, and histological examination of the repaired tissues with H&E were performed. Collagen deposition (green arrow), hair follicle (red arrow), fibroblast (yellow arrow), neutrophil (purple arrow), blood vessel (blue arrow), and $CD31^+$ structures (brown)[224] (Copyright (2022) John Wiley and Sons).

Based on similar reasoning, Yang *et al.* created a hydrogel bandage consisting of MXene and bacterial cellulose that might hasten the healing of wounds when exposed to external electrical stimulation.[294] The production of the cellulose/MXene composite hydrogels involved both physical (hydrogen bonding) and chemical (covalent cross-linking) interactions, as shown in Fig. 25(a). Under various electrical stimulation potentials, the fluorescence pictures demonstrated that the NIH3T3 cells on the cellulose/MXene hydrogels with varying MXene content were highly active and displayed a higher cell density than those on the hydrogels without MXene nanosheets (Fig. 25(b)). The results showed a considerable change in cell activity after cellulose/MXene hydrogels were combined with external electrical stimulation. Additionally, outcomes from an *in vivo* rat experiment demonstrated that this method might hasten wound healing and encourage tissue regeneration. Copper electrodes were used on the hydrogel dressing in an *in vivo* experiment to apply an external electric field ranging from 0 to 400 mV. According to Fig. 25(c), the macroscopic images showed that the wounds treated with cellulose/MXene + electric field (100 mV mm^{-1}) had smaller surfaces than the other groups during therapy. When compared to a commercial film and cellulose hydrogel, the MXene-integrated hydrogels with or without an electric field caused the formation of new blood vessels, normal epithelium, less inflammation, higher density of fibroblasts, and a better wound healing effect, according to histological analysis of healed tissues using H&E and Masson's trichrome staining as well as immunofluorescent staining for CD31 (Fig. 25(d)). However, when an external electric field was used, wounds healed faster and underwent a more thorough re-epithelization and remodelling process.

4.7. Antimicrobial additives

As bacteria have grown more resistant to traditional antibiotics over the past few decades, along with the growing challenge of finding new, effective antibiotics, antibiotic-resistant bacterial illnesses have steadily become a serious hazard to public health. Determining new antimicrobial medicines to combat drug-resistant bacterial diseases is, therefore, one of the main goals of this field. Graphene and MoS_2, two critical examples of 2D nanomaterials, provided a wealth of outstanding chances for investigating extremely potent antibacterial drugs because of their distinct 2-dimensional structures. Compared to antibiotics, novel 2D nanoparticles have greater membrane penetration. The primary antibacterial mechanisms of 2D nanoparticles have been reported to be the generation of reactive oxygen species (ROS) and free radicals, enhanced oxidative stress, damage to genomic DNA, damage to cellular structural integrity, and physical damage to cell membranes due to the sharp edges of 2D materials.[295–299] MXene-based materials are regarded as high-potential antimicrobial agents because of their ability to load several antimicrobial functional groups, their large specific surface area, and their feasibility for functionalization and chemical modification.

The first observation that $Ti_3C_2T_x$ shows better antibacterial efficiency compared with graphene oxide was made by Rasool and Mahmoud *et al.*, who observed that $Ti_3C_2T_x$ exhibited antibacterial behaviour in colloidal suspensions.[300] The colony counting method was used to examine the inhibitory effects of three materials: delaminated $Ti_3C_2T_x$ nanosheets, ML-MXene, and $Ti_3AlC_2T_x$(MAX). The results showed that all three materials had an inhibitory effect on *B. subtilis* and *E. coli*. More precisely, a $Ti_3C_2T_x$ colloidal solution led to viability losses of *B. subtilis* and *E. coli* of 97.04 ± 2.91% and 97.70 ± 2.87%, respectively. After that, researchers measured the growth curves and cell viability of bacteria in $Ti_3C_2T_x$ colloidal solutions at different concentrations and discovered that the antibacterial action of the solution was dose-dependent. At a concentration of 200 μg mL^{-1} of $Ti_3C_2T_x$, the rate of bacterial inhibition exceeded 99%. Furthermore, $Ti_3C_2T_x$ exhibited more significant cell inactivation than GO when comparing the antibacterial properties of the two substances. Through the investigation of glutathione oxidation, SEM and TEM pictures, and LDH release, the antibacterial mechanism of $Ti_3C_2T_x$ nanosheets was hypothesized as follows: $Ti_3C_2T_x$ adsorbs on the surface of the cell, rupturing the cell membrane and ultimately causing damage and cell death. Using flow cytometry and fluorescence imaging techniques, the antibacterial performances of MXene nanosheets of different lateral sizes (0.09, 0.35, 0.57, and 4.40 μm) against *Bacillus subtilis* and *Escherichia coli* bacteria were investigated by Shamsabadi *et al.*

They confirmed that MXene's antibacterial performances were both size-dependent and exposure-time-dependent, which was the first study of MXene's primary antimicrobial mode of action.[301] Scientists employed a broth microdilution assay for the first time to ascertain the relationship between the antibacterial activity of MXene nanosheets and their contact with bacterial cells. They found that the sharp edges of MXene nanosheets severely destroyed the bacterial cell walls, causing the release of bacterial DNA and the eventual diffusion of the bacteria (Fig. 26(a)). Electrospun CS nanofiber mats were

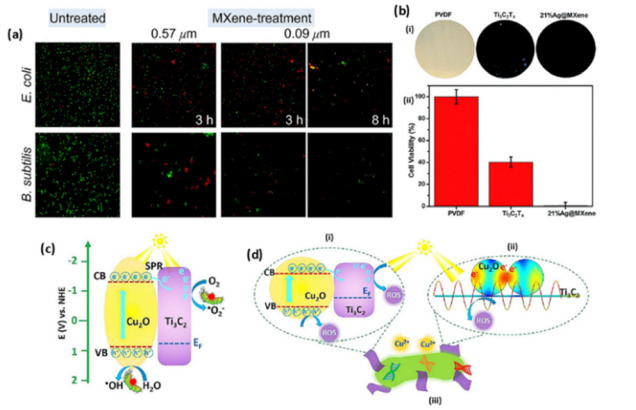

Fig. 26 (a) The antibacterial activity of MXenes is dependent on both size and exposure period. Fluorescence imaging analysis was carried out following the treatment of *Bacillus subtilis* and *Escherichia coli* with 100-μg mL^{-1} MXene nanosheets with sizes of 0.09 and 0.57 μm[301] (Copyright (2018) American Chemical Society); (b) Membranes constructed from 21% Ag@MXene, MXene ($Ti_3C_2T_x$), and PVDF (control) also exhibited antibacterial activity[306] (Copyright (2018) Royal Society of Chemistry); (c) diagrammatic illustration of improving Cu_2O/MXene antibacterial activity;[94] (d) diagrammatic illustration of the antibacterial mechanism of Cu_2O/MXene[94] (Copyright (2020) Elsevier).

functionalized with $Ti_3C_2T_x$ sheets for the first time to develop a flexible bandage material with exceptional antibacterial properties, which led to a cell reduction rate of 95% against Gram-negative bacteria (*Escherichia coli*) and 62% against Gram-positive bacteria (*Staphylococcus aureus*).[302] MXenes are used to make multifunctional composite films that exhibit great antibacterial properties and excellent biocompatibility and promote wound healing. Materials such as chitosan, electrospun poly(polycaprolactone), and chitin are used in this process.[303–305] MXenes have recently demonstrated that they can be modified by employing metal nanoparticles and metal oxides with antimicrobial activity (like copper, zinc, silver, *etc.*) to further improve antibacterial qualities.[88] Through self-reduction of $AgNO_3$ to produce AgNPs on the surfaces of MXene nanosheets, Ag@MXene composite nanopore membranes were developed.[306] *E. coli* was cultivated for 24 hours at 35 °C on PVDF (control), MXene, and 21% Ag@MXene composite membranes. The findings showed that the MXene membrane had an inhibition rate of roughly 60% against *E. coli*, whereas the 21% Ag@MXene composite membrane prevented the development of *E. coli* up to 99% (Fig. 26(b)). Practical antibacterial efficacy against *Pseudomonas aeruginosa* and *Staphylococcus aureus* bacteria was demonstrated by a cuprous oxide-anchored MXene nanosheet, with inhibition rates of 95.59% and 97.04%, respectively.[94] The antibacterial activity of the Cu_2O-anchored MXene nanosheets was significantly higher than that of the original MXene nanosheets due to the combined effects of MXene (acceleration of photoelectron transfer), Cu_2O (antibacterial activity and photocatalysis), the production of reactive oxygen species (ROS), and ionophore resonance (Fig. 26(c and d)). MXenes are a new multipurpose wound dressing because of their potent antibacterial qualities. In addition, the mild photothermal activity promotes angiogenesis and cell proliferation, which speed up the remodelling and repair of injured tissues.[307] The creation of wound dressings based on MXenes has garnered increasing interest. Gold nanoparticles (AuNPs) have several unique characteristics, such as low toxicity, photothermal and polyvalent effects, and the ability to speed up skin regeneration by increasing the migration of keratinocytes and fibroblasts. By adding gold nanoparticles (AuNPs) to MXene-based nanomaterials within the network of chitin sponge, Xu *et al.* created a chitin/MXene composite sponge. The created composite sponge encouraged regular skin cell migration to repair the infected wound and showed potent antibacterial activity through the synergy of the capture and photothermal effects.[305] An antibacterial nanofibrous membrane like MXene-AMX-PVA nanofibrous membrane is used to treat bacterially infected skin wounds by combining amoxicillin (AMX), MXene, and polyvinyl alcohol (PVA). The hyperthermia caused by MXene under reduced power density NIR irradiation slowed down bacterial growth and accelerated AMX release, which improved the rate at which bacterially infected wounds healed.[170]

4.8. Medical implants

Despite the widespread use of medical implants in clinical therapy today, several issues still need to be resolved, including immunological response, infection following surgery, inadequate healing, and tumour recurrence. Because of their exceptional biocompatibility, biodegradability, and antimicrobial activity, MXenes can be applied as a surface coating on implants to improve and toughen implants and even significantly reduce the probability of tumour recurrence and bacterial infection.[167,168,308,309] A novel multifunctional implant (Sp@MXGelMA) that combines MXene nanosheets, gelatin methacrylate (GelMA), and bioinert sulfonated polyetheretherketone (SP) was developed to fight the difficulties of tumour recurrence and bacterial infection complications associated with conventional treatments for osteosarcoma.[310] The Sp@MXTOB/GelMA implant has been shown through *in vitro* and *in vivo* experiments to exhibit excellent osseointegration, osteogenic commitment of preosteoblasts, and cytocompatibility. These properties render the implant a highly promising treatment for bone loss with osteosarcoma resection. Yin *et al.* integrated photonic-responsive 2D niobium carbide Nb_2CT_x nanosheets into 3D-printed bone-mimetic scaffolds to treat osteosarcoma.[168] The unique photonic response of the integrated 2D Nb_2CT_x nanosheets in the second near-infrared (NIR-II) biological aperture with a high tissue penetration depth allows them to block tumor regrowth and effectively kill bone cancer cells. Furthermore, the neovascularisation and migration of the damaged area can be significantly aided by the biodegradation of 2D Nb_2CT_x-integrated 3D-printed scaffolds, which would significantly speed up osseous regeneration to mend more significant bone defects. In recent years, human bone marrow mesenchymal stem cells have been demonstrated to undergo osteogenic differentiation more quickly in response to several two-dimensional materials,

including graphene.[311,312] The ability of MXenes, graphene analogs, to promote osteogenic differentiation and cell proliferation has also been demonstrated.[313] Zhang *et al.* first investigated the application of $Ti_3C_2T_x$ MXene films in bone tissue engineering and GBR treatment.[314] Cellular assessments showed that $Ti_3C_2T_x$ has good cytocompatibility and can promote cell proliferation. Further evidence of $Ti_3C_2T_x$ film's safety *in vivo* was demonstrated through the host tissue response to MXene films, which exhibited no appreciable inflammation or harmful side effects. Furthermore, MXenes stimulated early osteogenic differentiation of osteogenic cells, as demonstrated by the results of alkaline phosphatase (ALP) assay and qRT-PCR of MXenes. These observations were further supported by research using rat calvarial deficiency models. After developing the ultra-thin 2D MXenes, Shi *et al.* recently used Micro-CT, histological evaluations, and UHMWPE particle-induced osteolysis models to demonstrate the function of few-layered Nb_2C (FNC) in reducing the production of inflammatory cytokines and preventing osteoclastogenesis *via* ROS scavenging.[315] Furthermore, recent research demonstrates that two-dimensional $Ti_3C_2T_x$ MXene promotes the differentiation of neural stem cells (NSCs) and the electrophysiological maturation of neural circuits, providing a crucial and encouraging avenue for the development of a body of evidence promoting the use of $Ti_3C_2T_x$ MXene in the neural interface or scaffold in stem cell therapy and nerve tissue engineering from morphology, physiology, and functionality. Cultured NSCs on $Ti_3C_2T_x$ MXene films exhibited the capacity to stimulate NSC maturation by differentiating into neurons with greater efficiency and longer neurites. Moreover, $Ti_3C_2T_x$ MXene demonstrated no discernible impact on voltage-gated Na^+ or K^+ currents. However, it amplifies explicitly the amplitude of voltage-gated Ca^{2+} currents, potentially leading to longer neurons and longer neurites. Additionally, it boosted spiking, which in turn improved synaptic transmission. By specifically raising the frequency rather than the amplitude or quantity of synapses, $Ti_3C_2T_x$ MXene improves synaptic transmission.[316] Thus, MXene research offers a new kind of nanomaterial and opens up a new avenue for MXene use in biomedical applications because of its tumor-killing action and capacity for bone regeneration.

4.9. Sound energy harvesting and cochlear implant

The flawless operation of implanted medical equipment, such as pacemakers and neurostimulators, should be promised for a long time, which calls for energy sources with limitless capacity. Ultrasound waves are one of the most accessible and least attenuated energy sources that can safely charge implanted devices because of their low attenuation through human tissues. Nonetheless, most implantable energy harvesting devices on the market lack adequate biocompatibility and require particular materials and intricate manufacturing procedures. Here, we explored how MXene-based composites can capture ultrasonic energy. In this regard, the same MXene-homopolymeric hydrogel was employed for sensing.[229,317] It shows a fundamental device construction with two ecoflex coverings encasing a layer of the $Ti_3C_2T_x$–PVA hydrogel. The MXene-based device's output voltage increased to 2.8 V when the ultrasonic tip was placed directly in contact with it. With the entering ultrasonic wave, the voltage changed at a specific frequency (20 kHz). Furthermore, the device demonstrated its potential for *in vivo* charging by functioning in biological tissue-like media (water, hydrogel, and ecoflex) at varying distances between the tip and the device. Microdevices and wireless sensors can be sustained autonomously by materials and gadgets that capture acoustic energy. However, brittle piezoceramics, which are the basis of conventional acoustic energy harvesters, have limited their application in wearable electronics. The piezoelectric polymer PVDF-TrFE electrospun onto fabric-based electrodes enables acoustic harvesters to overcome these drawbacks. For the best electromechanical performance, polarisation locking of the electrospun PVDF-TrFE was induced using two-dimensional (2D) $Ti_3C_2T_x$ MXene flakes. It was determined that the mechanically strong, lightweight, and flexible device could detect and collect energy in the 50–1000 Hz sound frequency band at sound intensities between 60 and 95 dB, with a high sensitivity of 37 VPa^{-1}. At 200 Hz and 95 dB, the maximum output power is 19 mW cm^{-3}.[318] Furthermore, hair cell function could be replaced by piezoelectric materials because these materials can produce electric charge in response to sound wave vibration. In order to replace cochlear hair cells with self-powered acoustic sensors, a novel method utilising piezoelectric nanocomposite filaments, specifically poly(vinylidene fluoride) (PVDF), poly(vinylidene fluoride)/barium titanate (PVDF/BT), and poly(vinylidene fluoride)/reduced graphene oxide (PVDF/rGO), has been developed. With an overall acoustoelectric energy conversion efficiency of 3.25%, these flexible filaments have a unique capacity to produce electricity in response to frequency noises from 50 to 1000 Hz at moderate sound pressure levels (60 to 95 dB), reaching the audible range. With a high sensitivity of 117.5 mV $(Pa\ cm^2)^{-1}$, these flexible filaments function as self-powered acoustic sensors and show promise for possible use in cochlear implants.[319] Recently, energy harvesting techniques have shown great promise in demonstrating cochlear implants with consistent and reliable power, extending their operational life and improving user experience.[320] However, **MXenes** promise a new avenue for recharging small electronic devices in the future, including wearable innovative technology, implanted biomedical devices, and remote Internet-of-things equipment.

5. Challenges and future prospects

The exceptional physicochemical characteristics of MXenes, including their strength and stiffness, excellent chemical stability, high surface area, good hydrophilicity, and metallic conductivity, have inspired scientists to extensively explore their biomedical applications. Despite their potential, the commercialization and the development of low-cost, eco-friendly manufacturing processes face several significant challenges. To address these hurdles, focusing on green chemical processes is crucial. Environmentally friendly and nature-

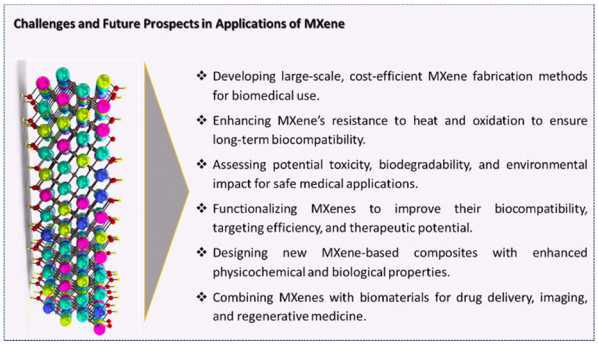

Fig. 27 Significant challenges related to manufacturing and application of MXenes.

inspired synthesis methods can reduce MXene toxicity and improve biocompatibility.[121,281,321,322] Surface functionalization and modification can help resolve some challenges, such as MXenes' stability and biocompatibility. For instance, functionalization strategies such as silylation effectively mitigate spontaneous oxidation, stabilize MXenes, and enhance surface properties like hydrophilicity.[323–326] Functionalization with phenylsulfonic groups has also improved specific surface area and dispersibility.[326] Furthermore, adjusting lamellar spacing, number of layers, and particle size enables tuning of optical and electrical properties, offering opportunities for targeted applications.[66,327,328] Hybridization with low-dimensional materials, including metals, metal oxides, and polymer nanomaterials, provides novel functionalities. For example, noble metal nanoparticles grown on flexible biomimetic MXene papers exhibit exceptional electrocatalytic performance, stability, and sensitivity for superoxide ($O2^{*-}$) detection, making them promising for high-performance flexible bioelectronics.[329–331] Similarly, integrating MXenes with natural polymers like cellulose and chitosan enhances their medicinal applications while improving biocompatibility. However, understanding these materials' cellular and molecular interactions with human tissues remains essential to minimize toxicity and ensure safe clinical use.[269,285,332] The commercialization of MXenes demands a comprehensive approach to optimize their production and application. This includes systematic biocompatibility examinations (*in vitro* and *in vivo*), environmental stability assessments, surface chemical characterization, and nanotoxicological evaluations. Additionally, preclinical studies should investigate biological responses to MXene-coated implants, ensuring effective integration with the host tissue.[333–336] Balancing stability and degradation rates is critical to enhancing therapeutic efficacy while minimizing potential side effects (Fig. 27).[249,337–339] Analytical optimization of targeted and controlled release behaviors is necessary for drug delivery. Recent advancements such as hetero-structured nanocarriers using Ti_3C_2 MXenes and cobalt nanowires demonstrate dual stimuli-responsive drug release and magnetic regulation, enabling synergistic chemo-photothermal cancer treatment.[340–342] Similarly, the MXene-based composite nanoplatform for hepatocellular cancer showcases improved hydrophilicity, drug delivery efficiency, and surface engineering for precise targeting.[332,337,343–345] Integrating MXenes with noble metals or natural polymers continues to enhance their multifunctionality, offering transformative potential in bioelectronics and therapeutic systems and systematically addressing current challenges, such as biosafety, scalable manufacturing, and regulatory systems. By systematically addressing current challenges, such as biosafety, scalable manufacturing, and regulatory compliance, MXenes are poised to revolutionize biomedicine, delivering innovative solutions for diagnostics, therapeutics, and clinical applications.

6. Conclusion

Due to their unique morphologies and ultrathin structural characteristics, MXenes and their composites have demonstrated remarkable potential in biomedical applications, particularly tissue engineering. Their exceptional physicochemical, optical, electrical, and biological capabilities offer exciting opportunities for developing versatile scaffolds with properties such as highly efficient photothermal conversion, controlled drug release, and stimulatory tissue regeneration. These advancements present significant potential for treating various diseases and malignancies, including tumors and cancers. MXenes can be functionalized for multiple biomedical applications and produced using simple, cost-effective processes. Modifying synthetic features and implementing optimal conditions can tailor their surface properties for specific uses such as tissue engineering, imaging, and sensing. MXenes and their composites exhibit high biocompatibility and can be engineered with antibacterial, anticancer, and immunomodulatory effects. Their remarkable electrical and optical properties make them excellent candidates for sensing applications.

Future research should focus on developing responsive scaffolds for mechanical and electrical fields, which could be used in regenerative medicine, intracellular fluorescent probes, partition membranes for artificial organs, and bio-electronic interfaces for neurotransmitters and bio-electronic signal recognition. Investigating novel, sustainable, and environmentally friendly synthetic methodologies for MXenes and their composites is crucial. These innovations could enable rapid sensing of cancerous cells and low-cost treatments, as well as advance tissue engineering. It is essential to systematically and analytically assess the effects of MXene size and composition on their properties, including their interactions with drugs and their toxicity, biodegradability, biocompatibility, histopathological effects, and biosafety concerns. Appropriate biofunctionalization and chemical surface modifications can enhance functionality, stability, bioavailability, biodegradability, and biocompatibility. These techniques also help reduce adverse effects and immune system reactions while improving targeting capabilities.

Author contributions

TD, PA, and SKM discussed the idea. TD wrote the original manuscript, while PA and SKM reviewed and finalized it.

Data availability

No primary research results, software or code have been included and no new data were generated or analysed as part of this review.

Conflicts of interest

The authors declare no conflicts of interest.

Acknowledgements

Shenzhen Longgang District Science and Technology Innovation Special Fund Medical and Health Technology Research and Development Project (LGKCYLWS2023). This work is part of the project SOFIA PID2023-147305OB-C32 funded by MICIU/AEI/10.13039/501100011033 and by FEDER/UE.

References

1 M. S. Ganewatta, Z. Wang and C. Tang, *Nat. Rev. Chem.*, 2021, **5**, 753–772.
2 A. K. Geim and K. S. Novoselov, *Nat. Mater.*, 2007, **6**, 183–191.
3 Y. Jing, Z. Zhou, C. R. Cabrera and Z. Chen, *J. Mater. Chem. A*, 2014, **2**, 12104–12122.
4 T. Dutta and S. Sarkar, *Appl. Nanosci.*, 2016, **6**, 1191–1197.
5 T. Dutta, R. Sarkar, B. Pakhira, S. Ghosh, R. Sarkar, A. Barui and S. Sarkar, *RSC Adv.*, 2015, **5**, 80192–80195.
6 A. VahidMohammadi, J. Rosen and Y. Gogotsi, *Science*, 2021, **372**, eabf1581.
7 S. Alwarappan, N. Nesakumar, D. Sun, T. Y. Hu and C.-Z. Li, *Biosens. Bioelectron.*, 2022, **205**, 113943.
8 S. Iravani and R. S. Varma, *Mater. Adv.*, 2022, **3**, 4783–4796.
9 S. Iravani and R. S. Varma, *Nano-Micro Lett.*, 2022, **14**, 213.
10 X. Zhan, C. Si, J. Zhou and Z. Sun, *Nanoscale Horiz.*, 2020, **5**, 235–258.
11 C. Wang, Y. Wang, X. Jiang, J. Xu, W. Huang, F. Zhang, J. Liu, F. Yang, Y. Song and Y. Ge, *Adv. Opt. Mater.*, 2019, **7**, 1900060.
12 S. Iravani, A. Zarepour, E. Nazarzadeh Zare, P. Makvandi, A. Khosravi, R. S. Varma and A. Zarrabi, *Mater. Adv.*, 2024, **5**, 8404–8418.
13 B.-M. Jun, S. Kim, J. Heo, C. M. Park, N. Her, M. Jang, Y. Huang, J. Han and Y. Yoon, *Nano Res.*, 2019, **12**, 471–487.
14 R. Song, M. Murphy, C. Li, K. Ting, C. Soo and Z. Zheng, *Drug Des., Dev. Ther.*, 2018, 3117–3145.
15 W. Park, H. Shin, B. Choi, W.-K. Rhim, K. Na and D. K. Han, *Prog. Mater. Sci.*, 2020, **114**, 100686.
16 A. Zavabeti, A. Jannat, L. Zhong, A. A. Haidry, Z. Yao and J. Z. Ou, *Nano-Micro Lett.*, 2020, **12**, 1–34.
17 M. Hassan, S. Liu, Z. Liang, S. Hussain, J. Liu, G. Liu and G. Qiao, *J. Adv. Ceram.*, 2023, **12**, 2149–2246.
18 Z. A. Sheikh, P. K. Katkar, H. Kim, S. Rehman, K. Khan, V. D. Chavan, R. Jose, M. F. Khan and D.-K. Kim, *J. Energy Storage*, 2023, **71**, 107997.
19 L. Chen, M. Wakeel, T. U. Haq, N. S. Alharbi, C. Chen and X. Ren, *Environ. Sci.: Nano*, 2022, **9**, 3168–3205.
20 Y. Tan, B. Hu, J. Song, Z. Chu and W. Wu, *Nano-Micro Lett.*, 2020, **12**, 1–42.
21 S. Rawal and M. Patel, *Nano-Micro Lett.*, 2021, **13**, 142.
22 S. Shi, Y. Si, Y. Han, T. Wu, M. I. Iqbal, B. Fei, R. K. Li, J. Hu and J. Qu, *Adv. Mater.*, 2022, **34**, 2107938.
23 G. Zan and Q. Wu, *Adv. Mater.*, 2016, **28**, 2099–2147.
24 S. Iravani and R. S. Varma, *Nano-Micro Lett.*, 2022, **14**, 213.
25 M. Qin, C. Merzougui, Y.-M. Su, Y.-F. Li, W.-Y. Chen and D. Huang, *New Carbon Mater.*, 2023, **38**, 496–506.
26 Z. Chen, Z. Wang and Z. Gu, *Acc. Chem. Res.*, 2019, **52**, 1255–1264.
27 A. P. Johnson, C. Sabu, K. Nivitha, R. Sankar, V. A. Shirin, T. Henna, V. Raphey, H. Gangadharappa, S. Kotta and K. Pramod, *J. Controlled Release*, 2022, **343**, 724–754.
28 J. Xue, Y. Zou, Y. Deng and Z. Li, *EcoMat*, 2022, **4**, e12209.
29 N. Shafiei, M. Nasrollahzadeh and S. Iravani, *Comments Inorg. Chem.*, 2021, **41**, 317–372.
30 C. Cai, W. Zhou and Y. Fu, *Chem. Eng. J.*, 2021, **418**, 129275.
31 S. Ma, P. Xue, Y. Tang, R. Bi, X. Xu, L. Wang and Q. Li, *Responsive Mater.*, 2024, **2**, e20230026.
32 T. Chen, J. Cai, X. Cheng, S. Cui, D. Zhang and D. Gong, *Chem. Eng. J.*, 2023, **477**, 147116.
33 Y. Zhou, Y. Zhang, K. Ruan, H. Guo, M. He, H. Qiu and J. Gu, *Sci. Bull.*, 2024, **69**, 2776–2792.
34 G. Jamalipour Soufi, P. Iravani, A. Hekmatnia, E. Mostafavi, M. Khatami and S. Iravani, *Comments Inorg. Chem.*, 2022, **42**, 174–207.
35 D. A. Darko, S. Sahu, J. Rathore, L. Kaur, B. Jain, S. Kanungo and R. Rawat, *Front. Energy Res.*, 2024, **12**, 1251188.
36 W. Zhang, X.-X. Ji and M.-G. Ma, *Chem. Eng. J.*, 2023, **458**, 141402.
37 A. M. Amani, L. Tayebi, M. Abbasi, A. Vaez, H. Kamyab, S. Chelliapan and E. Vafa, *ACS Omega*, 2024, **9**, 3123–3142.
38 M. Huang, Z. Gu, J. Zhang, D. Zhang, H. Zhang, Z. Yang and J. Qu, *J. Mater. Chem. B*, 2021, **9**, 5195–5220.
39 F. Yang, Y. Ge, T. Yin, J. Guo, F. Zhang, X. Tang, M. Qiu, W. Liang, N. Xu and C. Wang, *ACS Appl. Nano Mater.*, 2020, **3**, 11850–11860.
40 S. Iravani and R. S. Varma, *ACS Biomater. Sci. Eng.*, 2021, **7**, 1900–1913.
41 M. Naguib, M. Kurtoglu, V. Presser, J. Lu, J. Niu, M. Heon, L. Hultman, Y. Gogotsi and M. W. Barsoum, *Adv. Mater.*, 2011, **23**, 4248–4253.
42 O. Mashtalir, M. Naguib, V. N. Mochalin, Y. Dall'Agnese, M. Heon, M. W. Barsoum and Y. Gogotsi, *Nat. Commun.*, 2013, **4**, 1716.
43 P. Li, X. Zhao, Y. Ding, L. Chen, X. Wang and H. Xie, *Front. Ther. Eng.*, 2024, **4**, 1440165.
44 H. Yu, L. Xue, Y. Xue, H. Lu, Y. Liu, L. Wang, C.-F. Du and W. Liu, *Carbon Energy*, 2024, **6**, e597.

45 M. Naguib, V. N. Mochalin, M. W. Barsoum and Y. Gogotsi, *Adv. Mater.*, 2014, **26**, 992–1005.
46 U. Noor, M. F. Mughal, T. Ahmed, M. F. Farid, M. Ammar, U. Kulsum, A. Saleem, M. Naeem, A. Khan and A. Sharif, *Nanotechnology*, 2023, **34**, 262001.
47 H. Liu, T. Fu, Z. Cao and Y. Mao, *Environ. Sci.: Nano*, 2024, **11**, 2744–2770.
48 M. Naguib, J. Halim, J. Lu, K. M. Cook, L. Hultman, Y. Gogotsi and M. W. Barsoum, *J. Am. Chem. Soc.*, 2013, **135**, 15966–15969.
49 M. Downes, C. E. Shuck, B. McBride, J. Busa and Y. Gogotsi, *Nat. Protoc.*, 2024, 1–28.
50 Y. Wei, P. Zhang, R. A. Soomro, Q. Zhu and B. Xu, *Adv. Mater.*, 2021, **33**, 2103148.
51 M. Naguib, M. Kurtoglu, V. Presser, J. Lu, J. Niu, M. Heon, L. Hultman, Y. Gogotsi and M. W. Barsoum, *MXenes*, Jenny Stanford Publishing, 2011, pp. 15–29.
52 X. Wang and Y. Zhou, *J. Mater. Sci. Technol.*, 2010, **26**, 385–416.
53 M. Ghidiu, M. R. Lukatskaya, M.-Q. Zhao, Y. Gogotsi and M. W. Barsoum, *Nature*, 2014, **516**, 78–81.
54 J. Zhou, X. Zha, F. Y. Chen, Q. Ye, P. Eklund, S. Du and Q. Huang, *Angew. Chem., Int. Ed.*, 2016, **55**, 5008–5013.
55 Y. Guan, R. Zhao, Y. Cong, K. Chen, J. Wu, H. Zhu, Z. Dong, Q. Zhang, G. Yuan and Y. Li, *Chem. Eng. J.*, 2022, **433**, 133582.
56 M. Naguib, O. Mashtalir, J. Carle, V. Presser, J. Lu, L. Hultman, Y. Gogotsi and M. W. Barsoum, *ACS Nano*, 2012, **6**, 1322–1331.
57 X. Wang, X. Shen, Y. Gao, Z. Wang, R. Yu and L. Chen, *J. Am. Chem. Soc.*, 2015, **137**, 2715–2721.
58 H.-W. Wang, M. Naguib, K. Page, D. J. Wesolowski and Y. Gogotsi, *Chem. Mater.*, 2016, **28**, 349–359.
59 M. H. Tran, T. Schäfer, A. Shahraei, M. Dürrschnabel, L. Molina-Luna, U. I. Kramm and C. S. Birkel, *ACS Appl. Energy Mater.*, 2018, **1**, 3908–3914.
60 B. Anasori, Y. Xie, M. Beidaghi, J. Lu, B. C. Hosler, L. Hultman, P. R. Kent, Y. Gogotsi and M. W. Barsoum, *ACS Nano*, 2015, **9**, 9507–9516.
61 J. Halim, M. R. Lukatskaya, K. M. Cook, J. Lu, C. R. Smith, L.-Å. Näslund, S. J. May, L. Hultman, Y. Gogotsi and P. Eklund, *Chem. Mater.*, 2014, **26**, 2374–2381.
62 P. Urbankowski, B. Anasori, T. Makaryan, D. Er, S. Kota, P. L. Walsh, M. Zhao, V. B. Shenoy, M. W. Barsoum and Y. Gogotsi, *Nanoscale*, 2016, **8**, 11385–11391.
63 Y.-C. Zhou, L.-F. He, Z.-J. Lin and J.-Y. Wang, *J. Eur. Ceram. Soc.*, 2013, **33**, 2831–2865.
64 K. R. G. Lim, M. Shekhirev, B. C. Wyatt, B. Anasori, Y. Gogotsi and Z. W. Seh, *Nat. Synth.*, 2022, **1**, 601–614.
65 J. Xu, T. Peng, X. Qin, Q. Zhang, T. Liu, W. Dai, B. Chen, H. Yu and S. Shi, *J. Mater. Chem. A*, 2021, **9**, 14147–14171.
66 N. Hemanth and B. Kandasubramanian, *Chem. Eng. J.*, 2020, **392**, 123678.
67 A. Lipatov, S. Bagheri and A. Sinitskii, *ACS Mater. Lett.*, 2023, **6**, 298–307.
68 T. Zhang, L. Pan, H. Tang, F. Du, Y. Guo, T. Qiu and J. Yang, *J. Alloys Compd.*, 2017, **695**, 818–826.
69 A. VahidMohammadi, A. Hadjikhani, S. Shahbazmohamadi and M. Beidaghi, *ACS Nano*, 2017, **11**, 11135–11144.
70 B. Soundiraraju and B. K. George, *ACS Nano*, 2017, **11**, 8892–8900.
71 S. Zhao, X. Meng, K. Zhu, F. Du, G. Chen, Y. Wei, Y. Gogotsi and Y. Gao, *Energy Storage Mater.*, 2017, **8**, 42–48.
72 J. Halim, S. Kota, M. R. Lukatskaya, M. Naguib, M. Q. Zhao, E. J. Moon, J. Pitock, J. Nanda, S. J. May and Y. Gogotsi, *Adv. Funct. Mater.*, 2016, **26**, 3118–3127.
73 F. Du, H. Tang, L. Pan, T. Zhang, H. Lu, J. Xiong, J. Yang and C. J. Zhang, *Electrochim. Acta*, 2017, **235**, 690–699.
74 L. Wang, H. Zhang, B. Wang, C. Shen, C. Zhang, Q. Hu, A. Zhou and B. Liu, *Electron. Mater. Lett.*, 2016, **12**, 702–710.
75 F. Liu, J. Zhou, S. Wang, B. Wang, C. Shen, L. Wang, Q. Hu, Q. Huang and A. Zhou, *J. Electrochem. Soc.*, 2017, **164**, A709.
76 J. Zhou, X. Zha, X. Zhou, F. Chen, G. Gao, S. Wang, C. Shen, T. Chen, C. Zhi and P. Eklund, *ACS Nano*, 2017, **11**, 3841–3850.
77 Z. Ling, C. E. Ren, M.-Q. Zhao, J. Yang, J. M. Giammarco, J. Qiu, M. W. Barsoum and Y. Gogotsi, *Proc. Natl. Acad. Sci. U. S. A.*, 2014, **111**, 16676–16681.
78 H. Zhang, L. Wang, Q. Chen, P. Li, A. Zhou, X. Cao and Q. Hu, *Mater. Des.*, 2016, **92**, 682–689.
79 M. Naguib, T. Saito, S. Lai, M. S. Rager, T. Aytug, M. P. Paranthaman, M.-Q. Zhao and Y. Gogotsi, *RSC Adv.*, 2016, **6**, 72069–72073.
80 S. Ye, H. Zhang, H. Lai, J. Xu, L. Yu, Z. Ye and L. Yang, *Front. Bioeng. Biotechnol.*, 2024, **12**, 1338539.
81 Y. Dong, J. Liu, Y. Chen, T. Zhu, Y. Li, C. Zhang, X. Zeng, Q. Chen and Q. Peng, *Int. J. Biol. Macromol.*, 2023, **240**, 124482.
82 L. Zhou, H. Zheng, Z. Liu, S. Wang, Z. Liu, F. Chen, H. Zhang, J. Kong, F. Zhou and Q. Zhang, *ACS Nano*, 2021, **15**, 2468–2480.
83 R. Nie, Y. Sun, H. Lv, M. Lu, H. Huangfu, Y. Li, Y. Zhang, D. Wang, L. Wang and Y. Zhou, *Nanoscale*, 2022, **14**, 8112–8129.
84 Z. Riaz, S. Baddi, F. Gao and C. L. Feng, *Macromol. Biosci.*, 2023, **23**, 2300082.
85 Y. Zeng, P. Wang, B. He, S. Liu, Q. Ye and F. Zhou, *Prog. Org. Coat.*, 2023, **183**, 107727.
86 S. Iravani, N. Rabiee and P. Makvandi, *J. Mater. Chem. B*, 2024, **12**, 895–915.
87 J. A. Lemire, J. J. Harrison and R. J. Turner, *Nat. Rev. Microbiol.*, 2013, **11**, 371–384.
88 Z. B. Shifrina, V. G. Matveeva and L. M. Bronstein, *Chem. Rev.*, 2019, **120**, 1350–1396.
89 Y. a Qing, L. Cheng, R. Li, G. Liu, Y. Zhang, X. Tang, J. Wang, H. Liu and Y. Qin, *Int. J. Nanomed.*, 2018, 3311–3327.
90 C. J. Dedman, G. C. Newson, G.-L. Davies and J. A. Christie-Oleza, *Sci. Total Environ.*, 2020, **747**, 141229.
91 Q. Wu, L. Tan, X. Liu, Z. Li, Y. Zhang, Y. Zheng, Y. Liang, Z. Cui, S. Zhu and S. Wu, *Appl. Catal., B*, 2021, **297**, 120500.

92 K. Zheng, M. I. Setyawati, D. T. Leong and J. Xie, *ACS Nano*, 2017, **11**, 6904–6910.
93 K. Zheng, S. Li, L. Jing, P. Y. Chen and J. Xie, *Adv. Healthcare Mater.*, 2020, **9**, 2001007.
94 W. Wang, H. Feng, J. Liu, M. Zhang, S. Liu, C. Feng and S. Chen, *Chem. Eng. J.*, 2020, **386**, 124116.
95 H. Cheng, J. Wang, Y. Yang, H. Shi, J. Shi, X. Jiao, P. Han, X. Yao, W. Chen, X. Wei, P. Chu and X. Zhang, *Small*, 2022, **18**, 2200857.
96 H. Zheng, S. Wang, F. Cheng, X. He, Z. Liu, W. Wang, L. Zhou and Q. Zhang, *Chem. Eng. J.*, 2021, **424**, 130148.
97 Y. Hu, Q. Zeng, Y. Hu, J. He, H. Wang, C. Deng and D. Li, *Talanta*, 2024, **266**, 125101.
98 L. Liang, Q. Li, X. Yan, Y. Feng, Y. Wang, H.-B. Zhang, X. Zhou, C. Liu, C. Shen and X. Xie, *ACS Nano*, 2021, **15**, 6622–6632.
99 Y. Li, F. Meng, Y. Mei, H. Wang, Y. Guo, Y. Wang, F. Peng, F. Huang and Z. Zhou, *Chem. Eng. J.*, 2020, **391**, 123512.
100 Q. Yang, Z. Xu, B. Fang, T. Huang, S. Cai, H. Chen, Y. Liu, K. Gopalsamy, W. Gao and C. Gao, *J. Mater. Chem. A*, 2017, **5**, 22113–22119.
101 L. Jin, P. Wang, W. Cao, N. Song and P. Ding, *ACS Appl. Mater. Interfaces*, 2021, **14**, 1747–1756.
102 Z. Fan, D. Wang, Y. Yuan, Y. Wang, Z. Cheng, Y. Liu and Z. Xie, *Chem. Eng. J.*, 2020, **381**, 122696.
103 Y. Niu, J. Li, J. Gao, X. Ouyang, L. Cai and Q. Xu, *Nano Res.*, 2021, **14**, 3820–3839.
104 K. K. Reza, D. Tripathi, H. Mazumdar, K. Ahuja and A. Kaushik Fics Mrcs Ecs Acs, *Mater. Adv.*, 2024, 5.
105 J. Shao, J. Zhang, C. Jiang, J. Lin and P. Huang, *Chem. Eng. J.*, 2020, **400**, 126009.
106 S. M. Mousavi, M. Y. Kalashgrani, M. Binazadeh, Y. Mazaheri, N. Omidifar, V. Rahmanian, M. Riazi, C. W. Lai, R. H. Althomali and M. M. Rahman, *Mater. Today Chem.*, 2024, **38**, 102097.
107 C. Gokce, C. Gurcan, O. Besbinar, M. A. Unal and A. Yilmazer, *Nanoscale*, 2022, **14**, 239–249.
108 X. Mi, Z. Su, Y. Fu, S. Li and A. Mo, *Biomed. Mater.*, 2022, **17**, 035002.
109 R. Huang, X. Chen, Y. Dong, X. Zhang, Y. Wei, Z. Yang, W. Li, Y. Guo, J. Liu and Z. Yang, *ACS Appl. Bio Mater.*, 2020, **3**, 2125–2131.
110 S. Iravani, E. Nazarzadeh Zare and P. Makvandi, *ACS Biomater. Sci. Eng.*, 2024, **10**, 1892–1909.
111 N. Chen, W. Yang and C. Zhang, *Sci. Technol. Adv. Mater.*, 2021, **22**, 917–930.
112 Y. Li, Z. Peng, N. J. Holl, M. R. Hassan, J. M. Pappas, C. Wei, O. H. Izadi, Y. Wang, X. Dong, C. Wang, Y.-W. Huang, D. Kim and C. Wu, *ACS Omega*, 2021, **6**, 6643–6653.
113 H. Gu, Y. Xing, P. Xiong, H. Tang, C. Li, S. Chen, R. Zeng, K. Han and G. Shi, *ACS Appl. Nano Mater.*, 2019, **2**, 6537–6545.
114 Y. Yang, Z. Cao, P. He, L. Shi, G. Ding, R. Wang and J. Sun, *Nano Energy*, 2019, **66**, 104134.
115 G. Jia, A. Zheng, X. Wang, L. Zhang, L. Li, C. Li, Y. Zhang and L. Cao, *Sens. Actuators, B*, 2021, **346**, 130507.
116 M. Saeidi-Javash, Y. Du, M. Zeng, B. C. Wyatt, B. Zhang, N. Kempf, B. Anasori and Y. Zhang, *ACS Appl. Electron. Mater.*, 2021, **3**, 2341–2348.
117 F. Niu, Z. Qin, L. Min, B. Zhao, Y. Lv, X. Fang and K. Pan, *Adv. Mater. Technol.*, 2021, **6**, 2100394.
118 Y. Z. Zhang, Y. Wang, Q. Jiang, J. K. El-Demellawi, H. Kim and H. N. Alshareef, *Adv. Mater.*, 2020, **32**, 1908486.
119 Z. Fu, N. Wang, D. Legut, C. Si, Q. Zhang, S. Du, T. C. Germann, J. S. Francisco and R. Zhang, *Chem. Rev.*, 2019, **119**, 11980–12031.
120 J. Pang, R. G. Mendes, A. Bachmatiuk, L. Zhao, H. Q. Ta, T. Gemming, H. Liu, Z. Liu and M. H. Rummeli, *Chem. Soc. Rev.*, 2019, **48**, 72–133.
121 K. Huang, Z. Li, J. Lin, G. Han and P. Huang, *Chem. Soc. Rev.*, 2018, **47**, 5109–5124.
122 M. Alhabeb, K. Maleski, B. Anasori, P. Lelyukh, L. Clark, S. Sin and Y. Gogotsi, *Chem. Mater.*, 2017, **29**, 7633–7644.
123 J. Halim, J. Palisaitis, J. Lu, J. Thörnberg, E. Moon, M. Precner, P. Eklund, P. Å. Persson, M. Barsoum and J. Rosen, *ACS Appl. Nano Mater.*, 2018, **1**, 2455–2460.
124 E. Kayali, A. VahidMohammadi, J. Orangi and M. Beidaghi, *ACS Appl. Mater. Interfaces*, 2018, **10**, 25949–25954.
125 F. Kong, X. He, Q. Liu, X. Qi, Y. Zheng, R. Wang and Y. Bai, *Electrochim. Acta*, 2018, **265**, 140–150.
126 R. Ibragimova, P. Erhart, P. Rinke and H.-P. Komsa, *J. Phys. Chem. Lett.*, 2021, **12**, 2377–2384.
127 Y. Liu, H. Xiao and W. A. Goddard III, *J. Am. Chem. Soc.*, 2016, **138**, 15853–15856.
128 T. Dutta, N. Yadav, Y. Wu, G. J. Cheng, X. Liang, S. Ramakrishna, A. Sbai, R. Gupta, A. Mondal, Z. Hongyu and A. Yadav, *Nano Mater. Sci.*, 2024, **6**, 1–23.
129 Q. Peng, C. Si, J. Zhou and Z. Sun, *Appl. Surf. Sci.*, 2019, **480**, 199–204.
130 H. Wang, C. Si, J. Zhou and Z. Sun, *J. Phys. Chem. C*, 2017, **121**, 25164–25171.
131 M. Saliba, J. P. Atanas, T. M. Howayek and R. Habchi, *Nanoscale Adv.*, 2023, **5**, 6787–6803.
132 Q. H. Wang, K. Kalantar-Zadeh, A. Kis, J. N. Coleman and M. S. Strano, *Nat. Nanotechnol.*, 2012, **7**, 699–712.
133 J. You, C. Si, J. Zhou and Z. Sun, *J. Phys. Chem. C*, 2019, **123**, 3719–3726.
134 M. Khazaei, A. Ranjbar, M. Arai and S. Yunoki, *Phys. Rev. B*, 2016, **94**, 125152.
135 P. Zhang, L. Wang, Z. Huang, J. Yu, Z. Li, H. Deng, T. Yin, L. Yuan, J. K. Gibson, L. Mei, L. Zheng, H. Wang, Z. Chai and W. Shi, *ACS Appl. Mater. Interfaces*, 2020, **12**, 15579–15587.
136 L. Xiu, Z. Wang, M. Yu, X. Wu and J. Qiu, *ACS Nano*, 2018, **12**, 8017–8028.
137 V. N. Borysiuk, V. N. Mochalin and Y. Gogotsi, *Nanotechnology*, 2015, **26**, 265705.
138 E. A. Mayerberger, O. Urbanek, R. M. McDaniel, R. M. Street, M. W. Barsoum and C. L. Schauer, *J. Appl. Polym. Sci.*, 2017, **134**, 45295.
139 X. Gao, Z. Jia, B. Wang, X. Wu, T. Sun, X. Liu, Q. Chi and G. Wu, *Chem. Eng. J.*, 2021, **419**, 130019.

140 K. Rasool, R. P. Pandey, P. A. Rasheed, S. Buczek, Y. Gogotsi and K. A. Mahmoud, *Mater. Today*, 2019, **30**, 80–102.
141 L. Verger, V. Natu, M. Carey and M. W. Barsoum, *Trends Chem.*, 2019, **1**, 656–669.
142 Y. Cao, Q. Deng, Z. Liu, D. Shen, T. Wang, Q. Huang, S. Du, N. Jiang, C.-T. Lin and J. Yu, *RSC Adv.*, 2017, **7**, 20494–20501.
143 R. Liu and W. Li, *ACS Omega*, 2018, **3**, 2609–2617.
144 C. Yan, C. Ji, X. Zeng, R. Sun and C.-P. Wong, Interconnecting the Promising MXenes via Ag Nanowire in Epoxy Nanocomposites for High-Performance Thermal Management Applications, *2018 19th International Conference on Electronic Packaging Technology (ICEPT)*, Shanghai, China, 2018, pp. 510–512, DOI: 10.1109/ICEPT.2018.8480698.
145 R. Kang, Z. Zhang, L. Guo, J. Cui, Y. Chen, X. Hou, B. Wang, C.-T. Lin, N. Jiang and J. Yu, *Sci. Rep.*, 2019, **9**, 9135.
146 X. Cao, M. Wu, A. Zhou, Y. Wang, X. He and L. Wang, *e-Polymers*, 2017, **17**, 373–381.
147 L. Wang and B. Shi, *Materials*, 2018, **11**, 2335.
148 G. Gao, G. Ding, J. Li, K. Yao, M. Wu and M. Qian, *Nanoscale*, 2016, **8**, 8986–8994.
149 C. Si, J. Zhou and Z. Sun, *ACS Appl. Mater. Interfaces*, 2015, **7**, 17510–17515.
150 G. Wang, *J. Phys. Chem. C*, 2016, **120**, 18850–18857.
151 L. Hu, X. Wu and J. Yang, *Nanoscale*, 2016, **8**, 12939–12945.
152 M. Sternik and U. D. J. P. C. C. P. Wdowik, *Phys. Chem. Chem. Phys.*, 2018, **20**, 7754–7763.
153 J. He, P. Lyu, L. Sun, A. M. Garcia and P. Nachtigall, *J. Mater. Chem. C*, 2016, **4**, 6500–6509.
154 D. Xiong, X. Li, Z. Bai and S. Lu, *Small*, 2018, **14**, 1703419.
155 Z. Tan, Z. Fang, B. Li and Y. Yang, *ACS Omega*, 2020, **5**, 25848–25853.
156 B. U. Haq, S.-H. Kim, S. Tahir, R. Ahmed, S. AlFaify, K. Alam and A. R. Chaudhry, *Mater. Sci. Semicond. Process.*, 2023, **168**, 107837.
157 L. Ma, L. R. L. Ting, V. Molinari, C. Giordano and B. S. Yeo, *J. Mater. Chem. A*, 2015, **3**, 8361–8368.
158 A. Rafieerad, W. Yan, G. L. Sequiera, N. Sareen, E. Abu-El-Rub, M. Moudgil and S. Dhingra, *Adv. Healthcare Mater.*, 2019, **8**, 1900569.
159 S. Pan, J. Yin, L. Yu, C. Zhang, Y. Zhu, Y. Gao and Y. Chen, *Adv. Sci.*, 2020, **7**, 1901511.
160 S. Lin, H. Lin, M. Yang, M. Ge, Y. Chen and Y. Zhu, *Nanoscale*, 2020, **12**, 10265–10276.
161 S. Rohr, D. Schölly and A. G. Kleber, *Circ. Res.*, 1991, **68**, 114–130.
162 G. Basara, M. Saeidi-Javash, X. Ren, G. Bahcecioglu, B. C. Wyatt, B. Anasori, Y. Zhang and P. Zorlutuna, *Acta Biomater.*, 2022, **139**, 179–189.
163 A. Rafieerad, G. L. Sequiera, W. Yan, P. Kaur, A. Amiri and S. Dhingra, *J. Mech. Behav. Biomed. Mater.*, 2020, **101**, 103440.
164 J. K. Wychowaniec, J. Litowczenko, K. Tadyszak, V. Natu, C. Aparicio, B. Peplińska, M. W. Barsoum, M. Otyepka and B. Scheibe, *Acta Biomater.*, 2020, **115**, 104–115.
165 C. He, L. Yu, H. Yao, Y. Chen and Y. Hao, *Adv. Funct. Mater.*, 2021, **31**, 2006214.
166 C. Li, D. Chu, L. Jin, G. Tan and Z. Li, *J. Biomed. Nanotechnol.*, 2021, **17**, 2014–2020.
167 C. Yang, Y. Luo, H. Lin, M. Ge, J. Shi and X. Zhang, *ACS Nano*, 2020, **15**, 1086–1099.
168 J. Yin, S. Pan, X. Guo, Y. Gao, D. Zhu, Q. Yang, J. Gao, C. Zhang and Y. Chen, *Nano-Micro Lett.*, 2021, **13**, 1–18.
169 Y. Li, M. Han, Y. Cai, B. Jiang, Y. Zhang, B. Yuan, F. Zhou and C. Cao, *Biomater. Sci.*, 2022, **10**, 1068–1082.
170 X. Xu, S. Wang, H. Wu, Y. Liu, F. Xu and J. Zhao, *Colloids Surf., B*, 2021, **207**, 111979.
171 Q. Yang, H. Yin, T. Xu, D. Zhu, J. Yin, Y. Chen, X. Yu, J. Gao, C. Zhang and Y. Chen, *Small*, 2020, **16**, 1906814.
172 A. Rozmysłowska-Wojciechowska, E. Karwowska, M. Gloc, J. Woźniak, M. Petrus, B. Przybyszewski, T. Wojciechowski and A. M. Jastrzębska, *Materials*, 2020, **13**, 4587.
173 Y. Fu, J. Zhang, H. Lin and A. Mo, *Mater. Sci. Eng.: C*, 2021, **118**, 111367.
174 X. Sun, C. Huang, L. Wang, L. Liang, Y. Cheng, W. Fei and Y. Li, *Adv. Mater.*, 2021, **33**, 2001105.
175 M. Malaki, A. Maleki and R. S. Varma, *J. Mater. Chem. A*, 2019, **7**, 10843–10857.
176 M. Soleymaniha, M.-A. Shahbazi, A. R. Rafieerad, A. Maleki and A. Amiri, *Adv. Healthcare Mater.*, 2019, **8**, 1801137.
177 G. Yang, F. Liu, J. Zhao, L. Fu, Y. Gu, L. Qu, C. Zhu, J.-J. Zhu and Y. Lin, *Coord. Chem. Rev.*, 2023, **479**, 215002.
178 L. Bai, W. Yi, T. Sun, Y. Tian, P. Zhang, J. Si, X. Hou and J. Hou, *J. Mater. Chem. B*, 2020, **8**, 6402–6417.
179 H. Lin, X. Wang, L. Yu, Y. Chen and J. Shi, *Nano Lett.*, 2017, **17**, 384–391.
180 C. Dai, Y. Chen, X. Jing, L. Xiang, D. Yang, H. Lin, Z. Liu, X. Han and R. Wu, *ACS Nano*, 2017, **11**, 12696–12712.
181 J. Guo, B. Legum, B. Anasori, K. Wang, P. Lelyukh, Y. Gogotsi and C. A. Randall, *Adv. Mater.*, 2018, **30**, 1801846.
182 Z. Li, H. Zhang, J. Han, Y. Chen, H. Lin and T. Yang, *Adv. Mater.*, 2018, **30**, 1706981.
183 W. Tang, Z. Dong, R. Zhang, X. Yi, K. Yang, M. Jin, C. Yuan, Z. Xiao, Z. Liu and L. Cheng, *ACS Nano*, 2018, **13**, 284–294.
184 R. Liang, Y. Li, M. Huo, H. Lin and Y. Chen, *ACS Appl. Mater. Interfaces*, 2019, **11**, 42917–42931.
185 Y. Zhang, Y. Cheng, F. Yang, Z. Yuan, W. Wei, H. Lu, H. Dong and X. Zhang, *Nano Today*, 2020, **34**, 100919.
186 Y. Sun, Y. Zhang, H. Zhang, M. Liu and Y. Liu, *Anal. Chem.*, 2020, **92**, 10668–10676.
187 H. Hu, W. Feng, X. Qian, L. Yu, Y. Chen and Y. Li, *Adv. Mater.*, 2021, **33**, 2005062.
188 B. Geng, S. Xu, L. Shen, F. Fang, W. Shi and D. Pan, *Carbon*, 2021, **179**, 493–504.
189 Y. Wu, W. Xiong, Z. Wang, Y. Wang, K.-Y. Sun, X. Song, Z. Lv, W. Xu, W. Zhong and X. Zou, *Chem. Eng. J.*, 2022, **427**, 131925.
190 S. Wang, Z. Zhang, S. Wei, F. He, Z. Li, H.-H. Wang, Y. Huang and Z. Nie, *Acta Biomater.*, 2021, **130**, 138–148.

191 Z. Hao, Y. Li, X. Liu, T. Jiang, Y. He, X. Zhang, C. Cong, D. Wang, Z. Liu and D. Gao, *Chem. Eng. J.*, 2021, **425**, 130639.
192 Y. Dong, S. Li, X. Li and X. Wang, *Int. J. Biol. Macromol.*, 2021, **190**, 693–699.
193 W. Guo, F. Wang, D. Ding, C. Song, C. Guo and S. Liu, *Chem. Mater.*, 2017, **29**, 9262–9274.
194 F. Daneshvar, F. Salehi, M. Karimi, R. D. Vais, M. Mosleh-Shirazi and N. Sattarahmady, *J. Photochem. Photobiol., B*, 2020, **203**, 111737.
195 J. Ming, J. Zhang, Y. Shi, W. Yang, J. Li, D. Sun, S. Xiang, X. Chen, L. Chen and N. Zheng, *Nanoscale*, 2020, **12**, 3916–3930.
196 C. Xing, S. Chen, X. Liang, Q. Liu, M. Qu, Q. Zou, J. Li, H. Tan, L. Liu and D. Fan, *ACS Appl. Mater. Interfaces*, 2018, **10**, 27631–27643.
197 J. Yin, Q. Han, J. Zhang, Y. Liu, X. Gan, K. Xie, L. Xie and Y. Deng, *ACS Appl. Mater. Interfaces*, 2020, **12**, 45891–45903.
198 Y. Cao, T. Wu, K. Zhang, X. Meng, W. Dai, D. Wang, H. Dong and X. Zhang, *ACS Nano*, 2019, **13**, 1499–1510.
199 W. Feng, R. Wang, Y. Zhou, L. Ding, X. Gao, B. Zhou, P. Hu and Y. Chen, *Adv. Funct. Mater.*, 2019, **29**, 1901942.
200 Y. Pei, X. Zhang, Z. Hui, J. Zhou, X. Huang, G. Sun and W. Huang, *ACS Nano*, 2021, **15**, 3996–4017.
201 R. A. Soomro, S. Jawaid, Q. Zhu, Z. Abbas and B. Xu, *Chin. Chem. Lett.*, 2020, **31**, 922–930.
202 M. Khazaei, A. Ranjbar, M. Arai, T. Sasaki and S. Yunoki, *J. Mater. Chem. C*, 2017, **5**, 2488–2503.
203 J. Yan, C. E. Ren, K. Maleski, C. B. Hatter, B. Anasori, P. Urbankowski, A. Sarycheva and Y. Gogotsi, *Adv. Funct. Mater.*, 2017, **27**, 1701264.
204 Y. Xue, Q. Zhang, W. Wang, H. Cao, Q. Yang and L. Fu, *Adv. Energy Mater.*, 2017, **7**, 1602684.
205 L. Lorencova, T. Bertok, J. Filip, M. Jerigova, D. Velic, P. Kasak, K. A. Mahmoud and J. Tkac, *Sens. Actuators, B*, 2018, **263**, 360–368.
206 M. Song, S. Y. Pang, F. Guo, M. C. Wong and J. Hao, *Adv. Sci.*, 2020, **7**, 2001546.
207 A. Sinha, H. Zhao, Y. Huang, X. Lu, J. Chen and R. Jain, *TrAC, Trends Anal. Chem.*, 2018, **105**, 424–435.
208 H. Sun, Y. Zhao, C. Wang, K. Zhou, C. Yan, G. Zheng, J. Huang, K. Dai, C. Liu and C. Shen, *Nano Energy*, 2020, **76**, 105035.
209 X. Cui, T. Zhao, S. Yang, G. Xie, Z. Zhang, Y. Zhang, S. Sang, Z.-H. Lin, W. Zhang and H. Zhang, *Nano Energy*, 2020, **78**, 105381.
210 M. Li, W.-Y. Cheng, Y.-C. Li, H.-M. Wu, Y.-C. Wu, H.-W. Lu, S.-L. Cheng, L. Li, K.-C. Chang and H.-J. Liu, *Nano Energy*, 2021, **79**, 105405.
211 F. X. Wang, M. J. Wang, H. C. Liu, Y. L. Zhang, Q. H. Lin, T. Chen and L. N. Sun, *Adv. Mater. Interfaces*, 2020, **7**, 2000536.
212 Z. Yu, L. Jiang, R. Liu, W. Zhao, Z. Yang, J. Zhang and S. Jin, *Chem. Eng. J.*, 2021, **426**, 131914.
213 W. Luo, H. Liu, X. Liu, L. Liu and W. Zhao, *Colloids Surf., B*, 2021, **201**, 111631.
214 J. Zhao, C. He, W. Wu, H. Yang, J. Dong, L. Wen, Z. Hu, M. Yang, C. Hou and D. Huo, *Talanta*, 2022, **237**, 122927.
215 Y. Nie, Z. Liang, P. Wang, Q. Ma and X. Su, *Anal. Chem.*, 2021, **93**, 17086–17093.
216 H. Zhang, Z. Wang, F. Wang, Y. Zhang, H. Wang and Y. Liu, *Talanta*, 2021, **224**, 121879.
217 S. Radhakrishnan and C. S. Rout, *Nanoscale Adv.*, 2023, **5**, 4649–4669.
218 L. Liu, Y. Yao, K. Ma, C. Shangguan, S. Jiao, S. Zhu and X. Xu, *Sens. Actuators, B*, 2021, **331**, 129470.
219 Y. Xu, X. Wang, C. Ding and X. Luo, *ACS Appl. Mater. Interfaces*, 2021, **13**, 20388–20396.
220 H. Wang, H. Li, Y. Huang, M. Xiong, F. Wang and C. Li, *Biosens. Bioelectron.*, 2019, **142**, 111531.
221 Y. Lei, W. Zhao, Y. Zhang, Q. Jiang, J. H. He, A. J. Baeumner, O. S. Wolfbeis, Z. L. Wang, K. N. Salama and H. N. Alshareef, *Small*, 2019, **15**, 1901190.
222 X. Jin, L. Li, S. Zhao, X. Li, K. Jiang, L. Wang and G. Shen, *ACS Nano*, 2021, **15**, 18385–18393.
223 S. Liang, *Front. Bioeng. Biotechnol.*, 2023, 11.
224 A. Maleki, M. Ghomi, N. Nikfarjam, M. Akbari, E. Sharifi, M.-A. Shahbazi, M. Kermanian, M. Seyedhamzeh, E. Nazarzadeh Zare, M. Mehrali, O. Moradi, F. Sefat, V. Mattoli, P. Makvandi and Y. Chen, *Adv. Funct. Mater.*, 2022, **32**, 2203430.
225 S. Sharma, A. Chhetry, M. Sharifuzzaman, H. Yoon and J. Y. Park, *ACS Appl. Mater. Interfaces*, 2020, **12**, 22212–22224.
226 K. Zhang, J. Sun, J. Song, C. Gao, Z. Wang, C. Song, Y. Wu and Y. Liu, *ACS Appl. Mater. Interfaces*, 2020, **12**, 45306–45314.
227 Q. Guo, X. Zhang, F. Zhao, Q. Song, G. Su, Y. Tan, Q. Tao, T. Zhou, Y. Yu and Z. Zhou, *ACS Nano*, 2020, **14**, 2788–2797.
228 M. Zhu, Y. Yue, Y. Cheng, Y. Zhang, J. Su, F. Long, X. Jiang, Y. Ma and Y. Gao, *Adv. Electron. Mater.*, 2020, **6**, 1901064.
229 Y.-Z. Zhang, K. H. Lee, D. H. Anjum, R. Sougrat, Q. Jiang, H. Kim and H. N. Alshareef, *Sci. Adv.*, 2018, **4**, eaat0098.
230 H. An, T. Habib, S. Shah, H. Gao, A. Patel, I. Echols, X. Zhao, M. Radovic, M. J. Green and J. L. Lutkenhaus, *ACS Appl. Nano Mater.*, 2019, **2**, 948–955.
231 H. Liao, X. Guo, P. Wan and G. Yu, *Adv. Funct. Mater.*, 2019, **29**, 1904507.
232 X. Wu, H. Liao, D. Ma, M. Chao, Y. Wang, X. Jia, P. Wan and L. Zhang, *J. Mater. Chem. C*, 2020, **8**, 1788–1795.
233 V. Kedambaimoole, N. Kumar, V. Shirhatti, S. Nuthalapati, P. Sen, M. M. Nayak, K. Rajanna and S. Kumar, *ACS Sens.*, 2020, **5**, 2086–2095.
234 M. Wu, M. He, Q. Hu, Q. Wu, G. Sun, L. Xie, Z. Zhang, Z. Zhu and A. Zhou, *ACS Sens.*, 2019, **4**, 2763–2770.
235 L. Zhao, K. Wang, W. Wei, L. Wang and W. Han, *InfoMat*, 2019, **1**, 407–416.
236 M. Xin, J. Li, Z. Ma, L. Pan and Y. Shi, *Front. Chem.*, 2020, **8**, 297.

237 W. Huang, L. Hu, Y. Tang, Z. Xie and H. Zhang, *Adv. Funct. Mater.*, 2020, **30**, 2005223.
238 L. Zhou, X. Zhang, L. Ma, J. Gao and Y. Jiang, *Biochem. Eng. J.*, 2017, **128**, 243–249.
239 S. Seyedin, S. Uzun, A. Levitt, B. Anasori, G. Dion, Y. Gogotsi and J. M. Razal, *Adv. Funct. Mater.*, 2020, **30**, 1910504.
240 B. Li, K. Ma, S. Lu, X. Liu, Z. Ma, L. Zhang, X. Wang and S. Wang, *Appl. Phys. A: Mater. Sci. Process.*, 2020, **126**, 1–11.
241 R. Rakhi, P. Nayak, C. Xia and H. N. Alshareef, *Sci. Rep.*, 2016, **6**, 36422.
242 F. Wang, C. Yang, M. Duan, Y. Tang and J. Zhu, *Biosens. Bioelectron.*, 2015, **74**, 1022–1028.
243 G. Liu, J. Zou, Q. Tang, X. Yang, Y. Zhang, Q. Zhang, W. Huang, P. Chen, J. Shao and X. Dong, *ACS Appl. Mater. Interfaces*, 2017, **9**, 40077–40086.
244 S. Lai, Y. Jin, L. Shi, R. Zhou, Y. Zhou and D. An, *Nanoscale*, 2020, **12**, 591–601.
245 M. Jalali, Z. Gao, Y. Yu, R. S. Moakhar, Y. Ding, M. Zhuang, N. Zhou, T. König, A. Fery and S. Mahshid, *2D Mater.*, 2021, **8**, 035049.
246 L. Wang, J. Zhang, B. Qu, Q. Wu, R. Zhou, D. Li, B. Zhang, M. Ren and X. C. Zeng, *Carbon*, 2017, **122**, 176–184.
247 S. Lu, L. Sui, Y. Liu, X. Yong, G. Xiao, K. Yuan, Z. Liu, B. Liu, B. Zou and B. Yang, *Adv. Sci.*, 2019, **6**, 1801470.
248 Y. Qin, Z. Wang, N. Liu, Y. Sun, D. Han, Y. Liu, L. Niu and Z. Kang, *Nanoscale*, 2018, **10**, 14000–14004.
249 H. Huang, R. Jiang, Y. Feng, H. Ouyang, N. Zhou, X. Zhang and Y. Wei, *Nanoscale*, 2020, **12**, 1325–1338.
250 Z. Xiao, Z. Li, P. Li, X. Meng and R. Wang, *ACS Nano*, 2019, **13**, 3608–3617.
251 H. Cheng, L. X. Ding, G. F. Chen, L. Zhang, J. Xue and H. Wang, *Adv. Mater.*, 2018, **30**, 1803694.
252 T. Zhang, X. Jiang, G. Li, Q. Yao and J. Y. Lee, *ChemNanoMat*, 2018, **4**, 56–60.
253 S. Liu, J. Tian, L. Wang, Y. Zhang, X. Qin, Y. Luo, A. M. Asiri, A. O. Al-Youbi and X. Sun, *Adv. Mater.*, 2012, **24**, 2037.
254 H. Hu, Y. Liu, Z. Xie, Z. Xiao, G. Niu and J. Tang, *Adv. Opt. Mater.*, 2021, **9**, 2101423.
255 Q. Xue, H. Zhang, M. Zhu, Z. Pei, H. Li, Z. Wang, Y. Huang, Y. Huang, Q. Deng and J. Zhou, *Adv. Mater.*, 2017, 29.
256 G. Yang, J. Zhao, S. Yi, X. Wan and J. Tang, *Sens. Actuators, B*, 2020, **309**, 127735.
257 Q. Guan, J. Ma, W. Yang, R. Zhang, X. Zhang, X. Dong, Y. Fan, L. Cai, Y. Cao and Y. Zhang, *Nanoscale*, 2019, **11**, 14123–14133.
258 L. Luo, S. Ma, L. Li, X. Liu, J. Zhang, X. Li, D. Liu and T. You, *Food Chem.*, 2019, **292**, 98–105.
259 M. H. Elsayed, J. Jayakumar, M. Abdellah, T. H. Mansoure, K. Zheng, A. M. Elewa, C.-L. Chang, L.-Y. Ting, W.-C. Lin and H.-H. Yu, *Appl. Catal., B*, 2021, **283**, 119659.
260 K. Wang, R. Jiang, T. Peng, X. Chen, W. Dai and X. Fu, *Appl. Catal., B*, 2019, **256**, 117780.
261 Q. Lu, J. Wang, B. Li, C. Weng, X. Li, W. Yang, X. Yan, J. Hong, W. Zhu and X. Zhou, *Anal. Chem.*, 2020, **92**, 7770–7777.
262 Z. Wang, J. Xuan, Z. Zhao, Q. Li and F. Geng, *ACS Nano*, 2017, **11**, 11559–11565.
263 L. Zhou, F. Wu, J. Yu, Q. Deng, F. Zhang and G. Wang, *Carbon*, 2017, **118**, 50–57.
264 H. Villarraga-Gómez, E. L. Herazo and S. T. Smith, *Precis. Eng.*, 2019, **60**, 544–569.
265 P. F. FitzGerald, R. E. Colborn, P. M. Edic, J. W. Lambert, A. S. Torres, P. J. Bonitatibus Jr and B. M. Yeh, *Radiology*, 2016, **278**, 723–733.
266 C. Caro, M. Dalmases, A. Figuerola, M. L. García-Martín and M. P. Leal, *Nanoscale*, 2017, **9**, 7242–7251.
267 J. Xie, Z. Zhou, S. Ma, X. Luo, J. Liu, S. Wang, Y. Chen, J. Yan and F. Luo, *Nanoscale Res. Lett.*, 2021, **16**, 1–10.
268 M. H. Oh, N. Lee, H. Kim, S. P. Park, Y. Piao, J. Lee, S. W. Jun, W. K. Moon, S. H. Choi and T. Hyeon, *J. Am. Chem. Soc.*, 2011, **133**, 5508–5515.
269 H. Lin, Y. Wang, S. Gao, Y. Chen and J. Shi, *Adv. Mater.*, 2018, **30**, 1703284.
270 Z. Liu, H. Lin, M. Zhao, C. Dai, S. Zhang, W. Peng and Y. Chen, *Theranostics*, 2018, **8**, 1648.
271 K. Sasaguri and N. Takahashi, *Eur. J. Radiol.*, 2018, **99**, 40–54.
272 D. Ni, W. Bu, E. B. Ehlerding, W. Cai and J. Shi, *Chem. Soc. Rev.*, 2017, **46**, 7438–7468.
273 T. J. Clough, L. Jiang, K.-L. Wong and N. J. Long, *Nat. Commun.*, 2019, **10**, 1420.
274 R. J. McDonald, J. S. McDonald, D. F. Kallmes, M. E. Jentoft, D. L. Murray, K. R. Thielen, E. E. Williamson and L. J. Eckel, *Radiology*, 2015, **275**, 772–782.
275 C. Dai, H. Lin, G. Xu, Z. Liu, R. Wu and Y. Chen, *Chem. Mater.*, 2017, **29**, 8637–8652.
276 Z. Wang, T. Jia, Q. Sun, Y. Kuang, B. Liu, M. Xu, H. Zhu, F. He, S. Gai and P. Yang, *Biomaterials*, 2020, **228**, 119569.
277 Y. Chen, D. Ye, M. Wu, H. Chen, L. Zhang, J. Shi and L. Wang, *Adv. Mater.*, 2014, **26**, 7019–7026.
278 L. Zong, H. Wu, H. Lin and Y. Chen, *Nano Res.*, 2018, **11**, 4149–4168.
279 W. Rui, C. Tao and X. Liu, *Ultrason. Sonochem.*, 2020, **66**, 105095.
280 J. Huang and K. Pu, *Angew. Chem., Int. Ed.*, 2020, **59**, 11717–11731.
281 H. Lin, S. Gao, C. Dai, Y. Chen and J. Shi, *J. Am. Chem. Soc.*, 2017, **139**, 16235–16247.
282 X. Yuan, Y. Zhu, S. Li, Y. Wu, Z. Wang, R. Gao, S. Luo, J. Shen, J. Wu and L. Ge, *J. Nanobiotechnol.*, 2022, **20**, 154.
283 Z. Liu, L. Xie, J. Yan, P. Liu, H. Wen and H. Liu, *Aust. J. Chem.*, 2021, **74**, 847–855.
284 L. Jin, Y. Ma, R. Wang, S. Zhao, Z. Ren, S. Ma, Y. Shi, B. Hu and Y. Guo, *Mater. Today Adv.*, 2022, **14**, 100224.
285 X. Han, J. Huang, H. Lin, Z. Wang, P. Li and Y. Chen, *Adv. Healthcare Mater.*, 2018, **7**, 1701394.
286 D. Chen, Z. Jin, B. Zhao, Y. Wang and Q. He, *Adv. Mater.*, 2021, **33**, 2008089.
287 M. Rodrigues, N. Kosaric, C. A. Bonham and G. C. Gurtner, *Physiol. Rev.*, 2019, **99**, 665–706.

288 H. S. Kim, X. Sun, J.-H. Lee, H.-W. Kim, X. Fu and K. W. Leong, *Adv. Drug Delivery Rev.*, 2019, **146**, 209–239.
289 S. a Guo and L. A. DiPietro, *J. Dent. Res.*, 2010, **89**, 219–229.
290 M. Zafari, M. Mansouri, S. Omidghaemi, A. Yazdani, S. Pourmotabed, A. Hasanpour Dehkordi, H. Nosrati, M. Validi and E. Sharifi, *J. Biomed. Mater. Res., Part B*, 2020, **108**, 3084–3098.
291 F. R. Diniz, R. C. A. Maia, L. R. M. de Andrade, L. N. Andrade, M. Vinicius Chaud, C. F. da Silva, C. B. Corrêa, R. L. C. de Albuquerque Junior, L. Pereira da Costa and S. R. Shin, *Nanomaterials*, 2020, **10**, 390.
292 M. Bagheri, M. Validi, A. Gholipour, P. Makvandi and E. Sharifi, *Bioeng. Transl. Med.*, 2022, **7**, e10254.
293 F.-S. Lin, J.-J. Lee, A. K.-X. Lee, C.-C. Ho, Y.-T. Liu and M.-Y. Shie, *Polymers*, 2020, **13**, 70.
294 L. Mao, S. Hu, Y. Gao, L. Wang, W. Zhao, L. Fu, H. Cheng, L. Xia, S. Xie, W. Ye, Z. Shi and G. Yang, *Adv. Healthcare Mater.*, 2020, **9**, 2000872.
295 S. Begum, A. Pramanik, D. Davis, S. Patibandla, K. Gates, Y. Gao and P. C. Ray, *ACS Omega*, 2020, **5**, 3116–3130.
296 H. Zhao, C. Zhang, Y. Wang, W. Chen and P. J. Alvarez, *Environ. Sci. Technol.*, 2018, **52**, 12783–12791.
297 Q. Xin, H. Shah, A. Nawaz, W. Xie, M. Z. Akram, A. Batool, L. Tian, S. U. Jan, R. Boddula, B. Guo, Q. Liu and J. R. Gong, *Adv. Mater.*, 2019, **31**, e1804838.
298 X. Xie, C. Mao, X. Liu, L. Tan, Z. Cui, X. Yang, S. Zhu, Z. Li, X. Yuan and Y. Zheng, *ACS Cent. Sci.*, 2018, **4**, 724–738.
299 A. Anand, B. Unnikrishnan, S.-C. Wei, C. P. Chou, L.-Z. Zhang and C.-C. Huang, *Nanoscale Horiz.*, 2019, **4**, 117–137.
300 K. Rasool, M. Helal, A. Ali, C. E. Ren, Y. Gogotsi and K. A. Mahmoud, *ACS Nano*, 2016, **10**, 3674–3684.
301 A. Arabi Shamsabadi, M. Sharifian Gh, B. Anasori and M. Soroush, *ACS Sustainable Chem. Eng.*, 2018, **6**, 16586–16596.
302 E. A. Mayerberger, R. M. Street, R. M. McDaniel, M. W. Barsoum and C. L. Schauer, *RSC Adv.*, 2018, **8**, 35386–35394.
303 L. Wang, L. Du, M. Wang, X. Wang, S. Tian, Y. Chen, X. Wang, J. Zhang, J. Nie and G. Ma, *Carbohydr. Polym.*, 2022, **285**, 119209.
304 Y. Yang, X. Zhou, Y. K. Chan, Z. Wang, L. Li, J. Li, K. Liang and Y. Deng, *Small*, 2022, **18**, e2105988.
305 S. Li, B. Gu, X. Li, S. Tang, L. Zheng, E. Ruiz-Hitzky, Z. Sun, C. Xu and X. Wang, *Adv. Healthcare Mater.*, 2022, **11**, 2102367.
306 R. P. Pandey, K. Rasool, V. E. Madhavan, B. Aïssa, Y. Gogotsi and K. A. Mahmoud, *J. Mater. Chem. A*, 2018, **6**, 3522–3533.
307 X. Zhang, B. Tan, Y. Wu, M. Zhang and J. Liao, *Polymers*, 2021, **13**, 2100.
308 A. Mazinani, H. Rastin, M. J. Nine, J. Lee, A. Tikhomirova, T. T. Tung, R. Ghomashchi, S. Kidd, S. Vreugde and D. Losic, *J. Mater. Chem. B*, 2021, **9**, 6412–6424.
309 Y. Fu, J. Zhang, H. Lin and A. Mo, *Mater. Sci. Eng.: C*, 2021, **118**, 111367.
310 J. Yin, Q. Han, J. Zhang, Y. Liu, X. Gan, K. Xie, L. Xie and Y. Deng, *ACS Appl. Mater. Interfaces*, 2020, **12**, 45891–45903.
311 J. Lu, C. Cheng, Y.-S. He, C. Lyu, Y. Wang, J. Yu, L. Qiu, D. Zou and D. Li, *Adv. Mater.*, 2016, **28**, 4025–4031.
312 T. R. Nayak, H. Andersen, V. S. Makam, C. Khaw, S. Bae, X. Xu, P.-L. R. Ee, J.-H. Ahn, B. H. Hong, G. Pastorin and B. Özyilmaz, *ACS Nano*, 2011, **5**, 4670–4678.
313 K. Chen, Y. Chen, Q. Deng, S.-H. Jeong, T.-S. Jang, S. Du, H.-E. Kim, Q. Huang and C.-M. Han, *Mater. Lett.*, 2018, **229**, 114–117.
314 J. Zhang, Y. Fu and A. Mo, *Int. J. Nanomed.*, 2019, 10091–10103.
315 K.-Y. Sun, Y. Wu, J. Xu, W. Xiong, W. Xu, J. Li, Z. Sun, Z. Lv, X. Wu and Q. Jiang, *Bioact. Mater.*, 2022, **8**, 435–448.
316 Y. Li, Y. Hu, H. Wei, W. Cao, Y. Qi, S. Zhou, P. Zhang, H. Li, G.-L. Li and R. Chai, *J. Nanobiotechnol.*, 2022, **20**, 398.
317 K. H. Lee, Y.-Z. Zhang, Q. Jiang, H. Kim, A. A. Alkenawi and H. N. Alshareef, *ACS Nano*, 2020, **14**, 3199–3207.
318 F. Mokhtari, K. A. S. Usman, J. Zhang, R. Komljenovic, Ž. Simon, B. Dharmasiri, A. Rezk, P. C. Sherrell, L. C. Henderson, R. J. Varley and J. M. Razal, *ACS Appl. Mater. Interfaces*, 2025, **17**, 3214–3228.
319 F. Mokhtari, S. Danti, B. Azimi, F. Hellies, E. Zanoletti, G. Albertin, L. Astolfi, R. J. Varley and J. M. Razal, *Energy Environ. Mater.*, 2025, **8**, e12807.
320 D. Chaudhuri, S. Kundu and N. Chattoraj, Harvesting energy with zinc oxide bio-compatible piezoelectric material for powering cochlear implants, *2017 Innovations in Power and Advanced Computing Technologies (i-PACT)*, Vellore, India, 2017, pp. 1–5, DOI: **10.1109/IPACT.2017.8245043**.
321 A. Bigham, A. Zarepour, M. Safarkhani, Y. Huh, A. Khosravi, N. Rabiee, S. Iravani and A. Zarrabi, *Nano Mater. Sci.*, 2024, DOI: **10.1016/j.nanoms.2024.02.006**.
322 S. Iravani, *Ceram. Int.*, 2022, **48**, 24144–24156.
323 J. Ji, L. Zhao, Y. Shen, S. Liu and Y. Zhang, *FlatChem*, 2019, **17**, 100128.
324 A. Wojciechowska, M. Chandel and A. M. Jastrzębska, *MXene Nanocomposites*, CRC Press, 2023, pp. 37–66.
325 H. He, L. Guan and H. Le Ferrand, *J. Mater. Chem. A*, 2022, **10**, 19129–19168.
326 H. Wang, J. Zhang, Y. Wu, H. Huang and Q. Jiang, *J. Phys. Chem. Solids*, 2018, **115**, 172–179.
327 Z. Zhao, B. Shi, T. Wang, R. Wang, Q. Chang, J. Yun, L. Zhang and H. Wu, *Carbon*, 2023, 118450.
328 H. Liu, Z. Wang, J. Wang, Y. Yang, S. Wu, C. You, N. Tian and Y. Li, *Nanoscale*, 2022, **14**, 9218–9247.
329 Y. Zhou, L. Yin, S. Xiang, S. Yu, H. M. Johnson, S. Wang, J. Yin, J. Zhao, Y. Luo and P. K. Chu, *Adv. Sci.*, 2024, **11**, 2304874.
330 S. Han, M. Zou, X. Pu, Y. Lu, Y. Tian, H. Li, Y. Liu, F. Wu, N. Huang, M. Shen, E. Song and D. Wang, *VIEW*, 2023, **4**, 20230005.
331 L. Qin, J. Jiang, L. Hou, F. Zhang and J. Rosen, *J. Mater. Chem. A*, 2022, **10**, 12544–12550.
332 H. Lin, Y. Chen and J. Shi, *Adv. Sci.*, 2018, **5**, 1800518.

333 Q. Li, X. Wu, S. Mu, C. He, X. Ren, X. Luo, M. Adeli, X. Han, L. Ma and C. Cheng, *Adv. Sci.*, 2023, **10**, 2207759.
334 Y. Fan, H. Ran, Z. Wang, C. Ning, J. Zhai and P. Yu, *Adv. Funct. Mater.*, 2024, 2308310.
335 B. Zhang, D. Lu and H. Duan, *Biomater. Sci.*, 2023, **11**, 356–379.
336 M. Soleymaniha, M. A. Shahbazi, A. R. Rafieerad, A. Maleki and A. Amiri, *Adv. Healthcare Mater.*, 2019, **8**, 1801137.
337 L. Chen, X. Dai, W. Feng and Y. Chen, *Acc. Mater. Res.*, 2022, **3**, 785–798.
338 J. Ma, L. Zhang and B. Lei, *ACS Nano*, 2023, **17**, 19526–19549.
339 H. Li, R. Fan, B. Zou, J. Yan, Q. Shi and G. Guo, *J. Nanobiotechnol.*, 2023, **21**, 73.
340 Y. Liu, Q. Han, W. Yang, X. Gan, Y. Yang, K. Xie, L. Xie and Y. Deng, *Mater. Sci. Eng.: C*, 2020, **116**, 111212.
341 M. Wang, Y. Wang and Q. Fu, *Mater. Today Bio*, 2024, **26**, 101027.
342 Y. Zhu, L. Feng, R. Zhao, B. Liu and P. Yang, *ACS Appl. Nano Mater.*, 2024, **7**, 2546–2574.
343 S. Iravani and R. S. Varma, *Mater. Adv.*, 2021, **2**, 2906–2917.
344 H. Park, J.-U. Kim, S. Kim, N. S. Hwang and H. D. Kim, *Mater. Today Bio*, 2023, **23**, 100881.
345 Z. Huang, X. Cui, S. Li, J. Wei, P. Li, Y. Wang and C.-S. Lee, *Nanophotonics*, 2020, **9**, 2233–2249.